Parameter estimation and assessment of continuum models of drying on the basis of pore network simulations

Dissertation

zur Erlangung des akademischen Grades

Doktoringenieur
(Dr.-Ing.)

von **M.Sc. Alireza Attari Moghaddam**

geb. am 22.09.1986 in Tabas, Iran

genehmigt durch die Fakultät für Verfahrens- und Systemtechnik
der Otto-von-Guericke-Universität Magdeburg

Promotionskommission: Prof. Dr.-Ing. Eckehard Specht (Vorsitz)

Prof. Dr.-Ing. habil. Evangelos Tsotsas (Gutachter)

Prof. Dr. Marc Prat (Gutachter)

Prof. Dr.-Ing. habil. Dominique Thévenin (Gutachter)

eingereicht am: 06.03.2017

Promotionskolloquium am: 15.06.2017

Declaration

I hereby declare that I prepared the dissertation with the title:

"Parameter estimation and assessment of continuum models of drying on the basis of pore network simulations"

without inadmissible assistance and without the use of any aids other than those indicated. Facts or ideas taken from other sources, either directly or indirectly, have been marked as such. In particular, I did not use the services of a commercial graduation consultation. Further I have not made payments to third parties either directly or indirectly for any work connected with the contents of the submitted dissertation.

The work has not so far been submitted either in Germany or abroad in same or similar form as a dissertation and has also not yet been published as a whole.

Magdeburg, March 06, 2017

M.Sc. Alireza Attari Moghaddam

Acknowledgments

Abstract

Drying of porous media is an active field of research which has applications in the production of foodstuffs, ceramics, biotechnological products and in the wood industry, to name only a few. In the course of the last 60 years, different types of mathematical models have been developed to predict the behavior and characteristics of drying processes. They address the drying process on different length scales and are divided generally into two classes: discrete and continuum models. While the former consider the transport phenomena at the pore scale, the latter solve the conservation equations in a larger volume (macro scale). Therefore, the discrete models are able to provide a comprehensive insight into the phenomena happening at the pore scale during the drying process. This sets the concept of this thesis, which is to use the detailed information provided by a discrete drying model (pore network model) in order to predict the macroscopic behavior of drying porous media.

One of the most common continuum models of drying is the one-equation continuum model which considers saturation as the only variable. In order to make use of such a model, macroscopic parameters, i.e. the moisture transport coefficient as well as the local relationship between vapor pressure and saturation inside the porous medium and at its surface, must be known as functions of saturation a priori. In the last decades, different experimental and empirical methods have been developed to extract the moisture transport coefficient of drying porous media. However, in this thesis, with the help of pore network drying simulations, a completely new numerical method is developed to obtain this coefficient.

In this work, drying of a rigid capillary porous medium is considered, i.e. of a porous medium in which the pore size is typically in the micrometer range. When modeling the drying process in such a medium by the one-equation continuum model, conventionally it is assumed that the vapor is in local equilibrium with the liquid both inside the porous medium and at the evaporative surface. However, the validity of this assumption has not been proven yet. This will be investigated here with the help of pore network drying simulations. Because of the importance of the evaporative surface, special focus will be set on the change of the degree of local equilibrium at the surface with the variation of operational conditions of the drying process, geometrical characteristics of the network and liquid transport mechanisms.

Owing to the low computational time of drying simulations by the one-equation continuum model, the main application of this and similar models is in the simulation of drying of large (industrial) sample sizes. However, in this work the aforementioned macroscopic parameters will be obtained for a network of size $25 \times 25 \times 51$ nodes, which is one or two orders of magnitude smaller than the industrial porous samples (in terms of number of pores along each direction of space). The direct prediction of the macroscopic parameters of such porous media by methods based on pore network drying simulations is almost impossible, since the computational time would be too high. However, in this work an attempt will be made to predict the macroscopic parameters of industrial sample sizes by the analysis of macroscopic parameters of smaller samples.

In the framework of the continuum approach to porous media, the liquid velocity inside the drying porous medium is obtained by the mass conservation law. This, for example, leads to a linear change of velocity with depth in the capillary regime. However, pore network drying simulations show a step-wise instantaneous velocity profile at each time step during drying, which is due to the invasion of a single meniscus. In order to reconcile the pore network model and continuum velocity profiles, a new spatio-temporal averaging method is deployed. In this way, the macroscopic velocity profiles are generated by the averaging of slice-averaged single invasion velocity profiles over time. The pore network and continuum model velocity profiles in the presence of stabilizing mechanisms, i.e. buoyancy and viscous forces, are also investigated.

The continuum model considers liquid as a continuous phase across the network at every time. However, the pore network drying simulations suggest that as the drying process goes on, the liquid in the main cluster is split into different liquid clusters and isolated menisci. Here, through the analysis of water flow rates, the contribution of each liquid cluster as well as isolated menisci to the total transport of water inside the porous medium will be investigated. By means of this analysis, the edge effect will also be characterized.

Kurzzusammenfassung

Die Trocknung poröser Medien ist Gegenstand aktueller Forschung und findet Anwendung in vielen Industriezweigen. Dazu zählen beispielsweise die Produktion von Lebensmitteln, Keramik, sowie Produkten der Biotechnologie und der Holzindustrie. In den letzten 60 Jahren wurden verschiedene mathematische Modelle entwickelt, um das Verhalten und Charakteristika von Trocknungsprozessen zu beschreiben. Diese Modelle behandeln die Trocknungsprozesse auf verschiedenen Skalen und werden im Allgemeinen in zwei Klassen unterteilt: diskrete Modelle und Kontinuumsmodelle. Während diskrete Modelle die Transportphänomene auf der Porenskala berücksichtigen, lösen Kontinuumsmodelle Erhaltungsgleichungen in einem größeren Volumen (Makroskala). Aus diesem Grund ist es mit diskreten Modellen möglich, umfassenden Einblick in die Phänomene, die während des Trocknungsprozesses auf der Porenskala ablaufen, zu erhalten. Demnach ist es Inhalt dieser Arbeit, das makroskopische Verhalten von trocknenden porösen Medien mit Hilfe von detaillierten Informationen aus dem diskreten Trocknungsmodell vorhersagen zu können.

Eines der am meisten genutzten Kontinuumsmodelle für Trocknungsprozesse besteht aus einer Gleichung und verwendet die Sättigung als einzige Variable. Um dieses Modell verwenden zu können, müssen makroskopische Parameter, wie z.B. der Feuchtetransportkoeffizient und die lokale Beziehung zwischen Dampfdruck und Sättigung im porösen Medium und an dessen Oberfläche, von vornherein als Funktionen der Sättigung bekannt sein. In den letzten Jahrzehnten sind verschiedene experimentelle und empirische Methoden zur Bestimmung des Feuchtetransportkoeffizienten in trocknenden porösen Medien entwickelt worden. In dieser Arbeit hingegen wird eine vollständig numerische Methode basierend auf Porennetzwerksimulationen entwickelt, um den Feuchtetransportkoeffizienten bestimmen zu können.

In der vorliegenden Arbeit wird die Trocknung eines starren kapillarporösen Mediums, dessen Porengrößen typischerweise im Mikrometerbereich liegen, behandelt. Die Modellierung eines Trocknungsprozesses in einem solchen Medium mit Hilfe des eine-Gleichung-Modells setzt üblicherweise voraus, dass der Wasserdampf lokal mit der Flüssigkeit, sowohl im Inneren des porösen Mediums, als auch an dessen Oberfläche, im Gleichgewicht steht. Die Gültigkeit dieser Annahme ist jedoch bisher nicht bewiesen worden und soll daher in dieser Arbeit mit Hilfe von Porennetzwerksimulationen untersucht werden. Aufgrund der

Wichtigkeit der Verdampfungsoberfläche des Netzwerks wird dabei der Schwerpunkt auf die Veränderung des lokalen Gleichgewichts an der Oberfläche gelegt, wobei Prozessparameter der Trocknung, geometrische Eigenschaften des Porennetzwerks sowie Mechanismen des Flüssigkeitstransports variiert werden.

Da das Kontinuumsmodell basierend auf einer Gleichung Trocknungsprozesse mit kurzer Berechnungszeit simulieren kann, wird es hauptsächlich zur Simulation der Trocknung von Proben im Industriemaßstab verwendet. In dieser Arbeit werden die erwähnten makroskopischen Parameter jedoch an einem Netzwerk der Größe 25x25x51 Knoten, welches viel kleiner als poröse Netzwerke im Industriemaßstab ist (bezogen auf die Anzahl der Poren in jede Raumrichtung), bestimmt. Die direkte Vorhersage von makroskopischen Parametern an diesen porösen Medien ist aufgrund der hohen Berechnungszeit nicht möglich. Deshalb wird in der vorliegenden Arbeit der Versuch unternommen, makroskopische Parameter von porösen Netzwerken im Industriemaßstab durch die Analyse makroskopischer Parameter von kleineren Netzwerken vorherzusagen.

Im Rahmen der Kontinuumsmodelle wird die Geschwindigkeit der Flüssigkeit innerhalb des porösen Mediums durch die Massenerhaltungsgleichung bestimmt. Dies führt zu einer linearen Veränderung der Geschwindigkeit abhängig von der Tiefe im Kapillarregime. Porennetzwerksimulationen zeigen jedoch, dass aufgrund des Eindringens der Gasphase in einen Meniskus ein stufenweises instantanes Geschwindigkeitsprofil während der Trocknung auftritt. Um die verschiedenen Geschwindigkeitsprofile der Modelle in Einklang zu bringen, wird eine neue raum-zeitliche Mittelwertbildungsmethode angewandt. Damit können makroskopische Geschwindigkeitsprofile durch Mittelwertbildung von über Schritte gemittelten Einzeleindringungsgeschwindigkeitsprofilen erzeugt werden. Der Einfluss von stabilisierenden Mechanismen, z.B. Auftrieb und viskose Kräfte, auf die Geschwindigkeitsprofile der Porennetzwerke und Kontinuumsmodelle wird ebenfalls untersucht.

Im Kontinuumsmodell wird die Flüssigkeit zu jedem Zeitpunkt als kontinuierliche Phase innerhalb des Netzwerks betrachtet. Porennetzwerksimulationen weisen jedoch darauf hin, dass die Flssigkeit während der Trocknung in Cluster und isolierte Menisken gespaltet wird. In dieser Arbeit wird durch Analyse der Wassermassenströme der Beitrag jedes Flüssigkeitsclusters und jedes isolierten Meniskus am gesamten Flüssigkeitstransport innerhalb des porösen Mediums untersucht. Anhand dieser Analyse wird zudem der Randeffekt charakterisiert.

Contents

Contents

Nomenclature

Roman symbols

A	cross sectional area	m^2
A_w	normalized wet surface area	-
a	lattice spacing	m
D	moisture transport coefficient	$\mathrm{m^2\,s^{-1}}$
D	network depth	m
D	space dimension	-
D_{abs}	absolute diffusivity	$\mathrm{m^2\,s^{-1}}$
D_f	fractal dimension	-
D_{rv}	relative diffusivity	-
g	acceleration of gravity	$\mathrm{m\,s^{-2}}$
g	hydraulic conductance	m^3
H	network height	m
h	height	m
J	mass flow rate	$\mathrm{kg\,s^{-1}}$
j	mass flux	$\mathrm{kg\,s^{-1}\,m^{-2}}$
k_{abs}	absolute permeability	m^2
$k_{r\ell}$	relative permeability	-
L	length	m
$\tilde{M}$	molar mass	$\mathrm{kg\,kmol^{-1}}$
m	mass	kg

n, N	numbers	-
p, P	pressure	Pa
Q	slice-averaged volumetric flow rate	$\mathrm{m^3\,s^{-1}}$
q	volumetric flow rate between two pores	$\mathrm{m^3\,s^{-1}}$
$\tilde{R}$	universal gas constant	$\mathrm{J\,kmol^{-1}\,K^{-1}}$
r	radius	m
S	saturation	-
T	temperature	K
t	time	s
U	slice-averaged liquid velocity	$\mathrm{m\,s^{-1}}$
u	liquid velocity in throat	$\mathrm{m\,s^{-1}}$
W	network width	m
x	space coordinate	m
y	space coordinate	m
z	vertical space coordinate	m

Greek symbols

γ	surface tension	$\mathrm{N\,m^{-1}}$
δ	boundary layer thickness	m
ε	porosity	-
θ	equilibrium contact angle	grad
μ	viscosity	$\mathrm{Pa\,s}$
$\dot{\vartheta}$	evaporation rate	$\mathrm{kg\,s^{-1}}$
ξ	normalized network depth	m
ρ	density	$\mathrm{kg\,m^{-3}}$
σ	standard deviation	various
Φ	throat potential	Pa

φ	NLE function	-

Superscripts and subscripts

a	air
atm	atmospheric
c	capillary
cth	capillary threshold
D	Darcy(superficial)
dry	dry
g	gas
ic	isolated cluster
irr	irreducible
it	isolated throat
k	horizontal slice number
ℓ	liquid
loc	local
mc	main cluster
min	minimum
net	network
sm	stable meniscus
$surf, s$	surface
t	throat
tht	top horizontal throat
tp	two-phase region
tvt	top vertical throat
um	unstable meniscus
v	vapor

w, wet wet

wp wet patch

∞ ambient

0   initial

0   average, reference

$*$ saturation

Abbreviations

Bo Bond number

BT breakthrough point

Ca capillary number

CM continuum model

CRP constant rate period

CV control volume

FRP falling rate period

IP invasion percolation

LE local equilibrium

MCD main cluster detachment

NLE non-local equilibrium

PN pore network

REV representative elementary volume

RFP receding front period

Chapter 1

Introduction

1.1 Overview

A porous medium consists of a solid matrix with interconnected void space (Fig. 1.1). The void space is comprised of a network of pore bodies (pores) and pore throats (throats), in which fluid transport occurs. Usually, the pores are randomly distributed in the porous medium and have different size and shape, resulting in an irregular structure of the material (Nield and Bejan [2006]). One or more fluids can flow through the void space simultaneously, leading to single- or multi-phase flow, respectively. Multi-phase flow in porous media is observed in many industrial applications, among them are enhanced oil recovery, filtration and drying. In all of the applications, the complex pore structure of the medium plays an important role for the displacement and distribution of fluid(s).

Solid matrix ▦ Pore space ▢
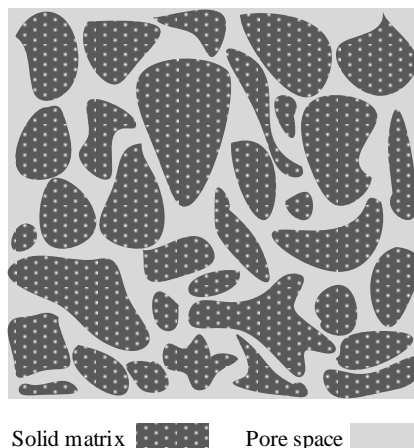
Figure 1.1: Solid matrix and pore space in a porous medium.

Drying, as a two-phase flow process with phase transition in porous media has been the subject of scientific publications for at least about a century, e.g. Lewis [1921], Ceaglske and Hougen [1937], and is still a field of active research, e.g. Defraeye [2014]. In this

process, the gas (non-wetting) phase displaces the liquid (wetting) phase. There are different types of drying processes, among them are convective drying, freeze drying and vacuum drying. Convective drying has many industrial applications and is considered in this thesis. In this process, the moisture is removed by the hot fresh air outside the medium. The displacement of the wetting phase during the drying process involves heat and mass transfer, thermodynamic phase change, and the interaction of various forces such as viscous, gravity, and capillary forces (Sahimi [2011]). These mechanisms and phenomena have been addressed in different fields such as soil physics (Brutsaert [1982]), drying of manufactured products (Mujumdar [2015]) or remediation of soils contaminated by light hydrocarbons (Ho and Udell [1992]), to name only a few.

Despite the fast progress in understanding of flow and transport in porous media in the last 25 years (Sahimi [2011]), many of its aspects are not yet well understood due to the complexity of the drying process, even for the simple situation corresponding to the typical laboratory experiment where water evaporates from a relatively thin sample at room temperature, e.g. Duan et al. [2012], Vincent et al. [2014]. This along with the continuous emergence of new applications, such as evaporation in fuel cells (Médici and Allen [2013]) or in loop heat pipes (Le et al. [2016]), has made the drying of porous media a very active field of research.

Several numerical approaches have been used so far to model the transport phenomena during the drying process in porous media. This is classically done within the framework of the continuum approach to porous media. In this approach the system is considered as a fictitious continuum and macroscopic equations valid at the level of a block of porous medium, i.e. the Representative Elementary Volume (REV), describe the transport phenomena. The main advantage of such models is to circumvent dealing with inhomogeneities at the pore-scale in porous media. By doing so, the computational time is decreased since the mathematical models are solved over a larger volume.

As the first type of continuum models (CM), and ideally, a macroscopic description is rigorously derived from the transport equations at the pore level by means of the volume averaging technique (Whitaker [1977]) or homogenization method (Sanchez-Palencia [1980]). The equations for conservation of momentum, energy, and mass along with their corresponding boundary conditions at the fluid-solid interface at the micro-level are well understood and can be simply written (see Chapter 2). However, numerical techniques are often not feasible for solving such boundary-value problems, owing to the irregular structure of the pores, particularly when dealing with a large number of pores as in industrial samples (Sahimi [2011]). Thus, if one could assume a REV, over which all the irregularities of pore space are smoothed and conservation laws are written, dealing with micro-structure complexities can be bypassed.

The concept of REV in the first type of continuum models is implemented by defining

effective parameters, which represent the average behavior of the REV. Here the REV is a part of the porous medium, in which the effective parameters do not change with increasing size. The REV must be small enough compared to the volume of the system, but large enough compared to the size of the pores, i.e. the so-called length scale separation rule should be met (Arce et al. [2005]).

Beside situations for which the fictitious continuum model can be rigorously extracted from the pore-level transport formulations (the first type of CMs), the macroscopic description of transport phenomena in the second type of continuum models is simply assumed to be valid, e.g. Luikov [1975], Philip and de Vries [1957]. In this case, the macroscopic equations are established using a priori an equivalence between the heterogeneous porous medium and a fictitious continuum (Bories [1991]) and the model is developed directly at the macroscopic level.

Although the resulting equations in the second type of continuum models resemble the ones in the first type (see Chapter 3 for CM equations), as no mathematical proof for the extraction of them has been given, their validity is in doubt (Prat [1998]). For example, are they genuinely local or only suitable for describing the macroscopic behavior of the system? Also, there are some cases for which the continuum approach cannot be expected to be valid because the length scale separation is not met, but no criterion is given to limit the application of the second type of continuum models (Prat [1998]). In this thesis, the first type of continuum models will be studied and for the sake of simplicity we will call them simply continuum models.

The geometrical homogenization (transition from pore scale to REV scale) in a CM requires the up-scaling of some phenomena and transport equations as well. For example, in drying of porous media, while the diffusion law or Darcy law can be used to calculate the flux of water vapor and liquid water at the pore scale, respectively, modified forms of these equations should be applied on the continuum scale. In fact, the effective parameters are responsible for such modification: The Darcy law will change to generalized Darcy law by introducing the effective permeability and in the diffusion equation the effective diffusivity will replace the binary diffusion coefficient (see Chapter 3 for explanation of continuum-scale transport equations). The microscopic capillary pressure, the Young-Laplace equation, will also be modified to the macroscopic capillary curve.

In addition to these upscalings that are required in continuum models of drying, there are some macro scale concepts and definitions that are used in drying porous media on a length scale larger than the pore scale. One of these concepts is saturation. At the pore scale, saturation is the volumetric fraction of water in one pore or throat, however, this value in a larger volume consisting of many pores and throats, is the fraction of volume of water in the total void space. Porosity is also a macro scale quantity, equal to the volume fraction of void space in the sample. Another example is the evaporation rate of

the sample. While each meniscus, a partially or fully filled pore or throat which is exposed to the gas phase, can produce a certain amount of water vapor, a summation of all water vapor flow rates coming out of all menisci in a porous medium gives the total evaporation rate of the sample. These large scale parameters, however, have nothing to do with the local conditions of drying and they are only used to give a macroscopic overview of the drying process.

The complexity of the transport of fluids in porous media is mainly due to the irregularities of the pore space, which are called inhomogeneities or heterogeneities. For example, Daian [2014] mentions that identification of microscopic pore structure parameters like topology and size of the pores or determination of how the pores are connected are extremely difficult because of such irregularities. In the context of drying process in porous media, dealing with micro scale heterogeneities and the study of transport phenomena in gas and liquid phase at the pore scale is the subject of discrete models of drying.

The discrete models solve the mass, energy and momentum equations at each pore and throat, therefore they require detailed information about the morphology and structure of the pore space inside the porous medium. The shape and size of the pores and throats, the way they are connected, the structure of their surface, and the number of throats connected to a pore, i.e. the coordination number, are only a few geometrical parameters of the porous medium that should be known when working with discrete models. Thus, these models are particularly useful when the effect of the pore space is strong (Sahimi [2011]). One of the main reasons that such models have gained attention, especially in the last 40 years, is that they give a comprehensive insight into the micro scale phenomena and can capture discrete effects such as percolation or local thermodynamical non-equilibrium (Perré [2010]). However, the main disadvantage of discrete models is that they need a high computational effort, owing to solving the transport phenomena at each pore and throat. As a result, a precise prediction of the behavior of large drying porous media with such models with the current facilities is impossible. Bundle of capillaries and pore network (PN) models are two types of discrete models for drying.

The bundle of capillaries model is strictly one-dimensional and therefore the liquid always forms a continuous phase (Metzger et al. [2008]). This feature is consistent with the classical continuum model, which acts as an advantage when extracting the macroscopic parameters of drying. However, a disadvantage of the bundle of capillaries model is that among all pore scale information, only the pore size distribution effect can be investigated (Vu [2006], Vu et al. [2006]). Other structural properties characterizing a real pore space cannot be investigated and more complete models, e.g. PN model, should be used.

In pore network models, the structure of the porous medium is microscopically modeled by representing it as a network of pores interconnected by throats. This enables to understand how pore-scale phenomena influence the drying process at the larger scale.

There are two main applications for PN models (Prat [2002]): a) the extraction of the effective parameters for continuum models, e.g. Attari Moghaddam et al. [2017b], Nowicki et al. [1992], Vorhauer et al. [2010], and b) analysis of the drying process at the pore scale. The pore network models in the latter case have been developed to address different aspects of the drying process like: fractal liquid pattern and drying curves, e.g. Laurindo and Prat [1996], Metzger et al. [2007a], Prat [1993]; three-dimensional simulations, e.g. Le Bray and Prat [1999], Yiotis et al. [2006]; liquid films, e.g. Prat [2007], Vorhauer et al. [2015], Yiotis et al. [2003]; surface phenomena, e.g. Attari Moghaddam et al. [2017c]. The pore network model used in this thesis is explained in Chapter 2.

According to what was explained, both continuum and discrete models have some advantages and disadvantages. The main advantage of CM models is that their computational time is very low compared to discrete models and, therefore, one is able to simulate industrial-scale drying porous samples. However, a disadvantage of such models is that they are not well-suited for situations in which the structure of the pore space plays a major role. In such cases, discrete models should be used instead. Also the length scale separation should be met in CM models, which is a limitation in application of CM models, while discrete models can be used for any sample size or geometry.

The outcome of the drying process in an industrial or field scale porous sample involves several scales. As Perré [2010] mentions, a perfect model for the transport of heat and mass in porous media is the one that includes the effect of all scales at the same time. However, achieving such a model requires a thorough understanding of the upscaling processes and that is why so many publications have been and still are devoted to this field.

1.2 Problem and motivation

It is assumed that during drying of porous media the local equilibrium (LE) assumption at the pore scale is met. This means that at a meniscus in a pore the vapor is in equilibrium with the liquid and therefore the vapor pressure is always saturation vapor pressure. However, upscaling this assumption, i.e. applying it over a large number of pores and throats is the subject of discussion. For example in hygroscopic porous media, it is proven that even in the presence of water in a REV, the average partial vapor pressure could deviate from the saturation vapor pressure if the saturation is smaller than a certain value. Therefore, a desorption isotherm is used in this case to account for the non-equilibrium effect (Peishi and Pei [1989]).

In a capillary porous medium, i.e. a porous medium in which the pore size is typically in the micrometer range (up to, say, sizes in the order of 100 microns), the water which is adsorbed in the solid matrix is almost negligible and therefore such a medium can

be considered non-hygroscopic (Geoffroy and Prat [2014]). In such porous media, it is assumed that local equilibrium pertains at the macro scale. This assumption practically means that if there is liquid in a REV, the transport of water vapor in the gas phase is zero, simply because there is no vapor pressure gradient. However, there has never been a pore scale study on this assumption, by which the validity of LE in capillary porous media could be investigated.

The local equilibrium assumption is used in the continuum model of drying at the surface and inside the capillary porous medium. At the surface this assumption theoretically predicts a constant drying rate period in the presence of water as long as the surface is fully or sufficiently wet. However, the pore network drying simulations on capillary porous media (see Chapter 3) show that even in the presence of water at the surface a perfect constant rate period is not observed, instead a slight continuous decrease of evaporation rate during this period is seen. This, in fact, contradicts the traditional LE assumption in capillary porous media. Moreover, our simulations show that inside the porous medium and in the two-phase region, where vapor and liquid are present at the same time, the vapor flux is non-zero. This means that in this region, the vapor pressure is not always saturation vapor pressure, which leads to a non-zero vapor pressure gradient and consequently a vapor flux.

As it is seen, some results obtained from simulations hint at the ineffectiveness of local equilibrium assumption in capillary porous media. Therefore, it is worth to investigate this assumption in such media to better assess its validity.

Le Bray and Prat [1999] observed a sharp drop in saturation profiles near the evaporative surface in their pore network drying simulation results. The sharp drop was also reported by Gupta et al. [2014] in experimental profiles of drying process obtained by NMR. This drop, which seems to be an intrinsic feature of the drying of porous media and later in this thesis is called the edge effect, cannot be described by macroscopic approaches available in literature. Actually, an important reason for the existence of such an effect in drying porous media could be attributed to the pore space configuration at the evaporative surface. While inside the network every pore or throat could be connected to its neighbors in higher and lower positions, this possibility does not exist for the pore spaces at the top of the network, owing to the fact that at the top of this area there is no pore space. Therefore, this region in the porous medium behaves differently during drying and needs a special attention.

One class of continuum models consider only saturation as a variable and are called one-equation continuum model, since only one equation for the conservation of gas and liquid phases is solved. Although dealing with only one variable makes these models very attractive, a difficulty in using them is that they include some macroscopic parameters that need to be determined before. These parameters are NLE (non-local equilibrium) func-

tions at the surface and inside the porous medium and the moisture transport coefficient. Up to now, the moisture transport coefficient has been mainly obtained by experiments (see Janz [1997] for a description of many experimental methods) or some simplifying assumptions, e.g. Schoeber [1976] who used a regular regime curve to extract the moisture transport coefficient. The problem with the experiments is that they are, most of the times, expensive and could take quite a long time to finish. In addition, when it comes to the determination of macroscopic parameters of industrial sample sizes, such methods cannot be used. From the other side, no upscaling method or mathematical model has been developed that would be able to give the values of this parameter. One of the main reasons for the lack of such a method is that it should be able to account for the transport of water in both phases at the same time, as well as dealing with the inhomogeneities of the pore structure. As it was mentioned before, dealing with the latter is already a difficult task, and to include the physical process in the upscaling process will make it even harder.

With the continuous increase in the understanding of transport phenomena at the pore scale and the power of computers, it is possible to obtain detailed information about the drying process at pore scale by discrete models. This will help to better understand and analyze the drying process in capillary porous media in different scales to see whether an upscaling method for the extraction of macroscopic parameters can be developed.

An important period during drying of porous media is the period, during which the surface is fully or partially wet. This is due to the fact that during this period evaporation rate is high and therefore the liquid in the porous medium can be dried out of the sample in the shortest possible time. Therefore, it is highly desirable, especially from the industrial point of view, to extend this period, so that to save energy and lower the cost of the process.

At each time during the drying process, the macroscopic approach is only able to give the saturation profile and the evaporation rate. However, it does not reveal, for example, why for some materials the drying period, during which the surface is wet, is longer or why for two different materials with the same surface saturation, the evaporation rate could be different. Fortunately, these questions can be answered by the detailed information that can be obtained from discrete models. Finding an answer to such questions regarding the evaporative surface will finally help us to change the drying parameters or even manufacture the materials in a way that could lead to the extension of this period.

As it was mentioned before, the local equilibrium assumption at the surface, which is used in the one-equation continuum model of drying in capillary porous media, expresses that as long as there is liquid at the surface, the vapor pressure of the surface is saturation vapor pressure, leading to creation of a perfect constant rate period. Therefore, this assumption directly affects the evaporation rate in the period in which the surface is partially or fully

wet. Thus, the analysis of the surface which was mentioned in the previous paragraph would give also some insight into this assumption, to see whether or not it is valid.

Similar to the analysis of the evaporative surface, the study of the distribution of liquid water inside the porous medium could also help to better understand the drying process. Pore network simulations reveal that the liquid inside the porous medium does not remain in one cluster during the drying process (Yiotis et al. [2010]). Instead, it splits into multiple clusters, each of which loses its connection to the others. This is due to the irregularities that exist in the pore space of the porous medium, which leads to the random emptying of pores and throats during the drying process. In order to better analyze the drying process, characterization of the liquid phase fragmentation into several clusters is important since each of the liquid clusters contributes differently to the water transport inside the porous sample. However, this is not a simple task. A sign of difficulties in the precise identification of this phenomenon is that no continuum model of drying has been developed so far to include it.

In the one-equation continuum model of drying, the liquid inside the porous medium is assumed to form a continuous phase at all times. This practically contradicts the findings of the pore network simulations and means that the liquid stays in one cluster during the whole drying process.

The splitting of the liquid phase into different clusters also affects its transport inside the porous medium. At each step of the drying process, the gas phase randomly invades into the menisci (almost always) one by one. This leads to a spontaneous impulse to the liquid phase, leading to creation of a step-change velocity profile inside the porous medium. This velocity profile is obviously created in the liquid cluster in which the invaded pore space is located. Therefore, the other liquid clusters are stagnant in this step. This phenomenon is important to be analyzed, especially in case of transport of species in porous media. However, the assumption made in the macroscopic approach, by which the liquid always forms a continuous phase, leads to a different type and magnitude of the liquid velocity field. In fact, from the macroscopic point of view, the liquid is always and everywhere moving. This clearly differs from what is predicted by pore scale models, and in case of transport of species leads to a different distribution of them inside the porous medium. Why these two approaches produce such different velocity profiles and whether they contradict each other should be investigated.

The discussion given in this section shows that during drying of porous media there are some phenomena and effects at the pore scale, which are considered differently in the macro scale framework, or in case of the edge effect or isolated liquid clusters are not considered at all. We believe that these effects and phenomena must be characterized if a comprehensive understanding of the drying process is to be achieved and thus a reliable continuum model is to be developed.

1.3 The new work

In this thesis, we will address the problems that were stated in the previous section by investigation of pore scale phenomena during drying of porous media. This will be done by the help of the detailed information obtained from PN drying simulations and with the methods explained below. The details of the PN model are given in Chapter 2.

As it was mentioned in the previous section, in the one-equation continuum model of drying of capillary porous media, it has been assumed that the local capillary equilibrium assumption is valid at the surface and inside the network. In this work, with the help of the pore network drying simulations the validity of this assumption will be investigated. In order to do so, a slice which contains one row of pores is considered in the PN and then its average vapor pressure and saturation are recorded at different times during the drying process. By this procedure, the local capillary equilibrium assumption inside capillary porous media will be investigated. The same process will be used at the evaporative surface, to see whether a different behavior is observed. The relationship between saturation of the slice and its normalized vapor pressure is called NLE function.

The NLE function at the surface is used in the evaporation rate formula of the one-equation continuum model. Therefore, it has a direct effect on the evaporation rate and should be studied in different cases. The changes of this function with operating conditions of the drying process, geometrical specifications of the pore space and different mechanisms of the liquid transport inside the porous medium will be investigated. In this series of studies, the focus will be on the phase distribution of the surface, i.e. the contribution of wet and dry patches and the change of vapor pressure of the gas pores at the surface. With the help of these two informations, a general relationship for the behavior of the NLE function will be established.

Inside the porous medium, the extracted NLE function will act as a link between saturation and vapor pressure to derive the one-equation continuum model. Therefore, its role is vital in the final formulation of this model, which is expressed only based on saturation.

The edge effect will also be investigated in this work. PN drying simulations can give us the detailed phase distribution at each time step of the drying process. Therefore, isolated clusters and menisci as well as the main cluster are known in each time step. With the analysis of the mass flow partition between all liquid clusters and the gas phase, as well as the analysis of the throats and pores at the top of the network, it will be shown why the saturation profiles experience a sharp drop in the region near the top of the network. Then it will be shown that the edge effect could lead to a sharp decrease in evaporation rate at the beginning of the process.

The identification of the moisture transport coefficient in the one-equation continuum model from pore scale simulations is also one of the subjects that will be discussed in this

work. As the NLE functions, the moisture transport coefficient must also be expressed as a function of saturation. In order to do so, a slice-sampling method is developed first. Each slice is composed of two successive rows of pores. Then the moisture transport coefficient is divided into two parts, one of which is responsible for the transport of water in the liquid phase and the other is responsible for the transport of water vapor in the gas phase. Since the pore network provides the liquid and vapor pressure fields in each time step, one is able to calculate the total liquid and vapor fluxes that pass through each slice by using Hagen-Poiseuille equation and the diffusion law, respectively. Finally, by using the mass conservation law for liquid and water vapor, the moisture transport coefficient in each phase will be obtained. The summation of these two quantities will give the moisture transport coefficient function versus saturation.

Two other methods will also be used to estimate the moisture transport coefficient. The first one is based on the local capillary equilibrium assumption, that is in a REV the phase distribution is only obtained by capillarity. Assuming this, capillary-controlled invasion percolation simulations will be performed on a REV to produce three effective parameters, namely, capillary pressure, relative permeability and relative diffusivity. These three functions along with the NLE function inside the porous medium which was obtained from PN drying simulations are used to produce the moisture transport coefficient. As a second method, the inverse method, in which the one-equation continuum model is integrated over space, will be used. The only information that is needed when using this method is saturation profiles. Therefore, the inverse method can be considered as a macroscopic method for determination of the moisture transport coefficient, although the slice-averaged saturation profiles are obtained from the PN drying simulations.

The expected behavior of moisture transport coefficient and its dependency on network saturation will also be discussed in this thesis. In addition, the moisture transport coefficients obtained from all the methods will be compared and their differences will be analyzed in detail. It should be noted that only with the help of an informative model like a pore network such comparisons can be made.

The velocity of the liquid phase inside the porous medium during drying will be analyzed by considering different mechanisms of the transport of liquid. In order to do so, two approaches in different scales will be studied: the macroscopic velocity field which is obtained by the mass conservation law, and the pore scale velocity obtained from pore network simulations. It will be shown that the latter is a step function of depth, with the position of the moving meniscus to be the position of the step change. However, the macroscopic velocity field is different, e.g. in the capillary regime it changes linearly with depth.

In order to investigate the different velocity profiles predicted by the two methods, a new spatio-temporal averaging method is deployed. As it was mentioned before, the

common method in upscaling of the processes in porous media is to take the average of parameters over space. However, here a new method of upscaling will be presented, that is step velocity profiles are averaged over a certain period of time to give the macroscopic velocity profiles. It will be shown that the probability density function of the moving menisci has a direct relationship with the macroscopic shape of the velocity profile. The impact of the edge effect on the velocity profiles will also be investigated.

The role of the isolated liquid clusters and isolated menisci in the velocity field will also be investigated. With the help of the pore network drying simulations, it will be shown that the liquid is mainly transported in the main cluster, while isolated clusters and menisci are at rest and stagnant.

1.4   Outline of contents

The descriptive outline of the next chapters is as follows:

Chapter 2 describes the pore network model that is used throughout the thesis. The mechanisms for the transport of liquid, i.e. capillary, gravity and viscous forces, as well as the diffusion that leads to the transport of water vapor during drying are discussed at the pore scale. It is shown in this chapter, how they are implemented in the PN model. Also the network and boundary layer geometry will be explained.

Chapter 3 starts with the derivation of the one-equation continuum model and the introduction of the three macroscopic parameters. Then the methods for the extraction of these parameters, which are based on the pore network drying simulations, are discussed one by one. Later in this chapter the results regarding the PN drying simulations as well as the macroscopic parameters are presented. This is followed by the comparison of saturation profiles and evaporation rate of the continuum model with PN drying simulation results. In addition, the effect of network size on the macroscopic parameters is investigated. It is also shown that the gravity-capillary regime under certain conditions can resemble the macroscopic parameters of the viscous-capillary regime.

Chapter 4 focuses on the analysis of the evaporative surface and of how its phase distribution affects the evaporation rate of the continuum model. In this chapter it is tried to find a relationship between the vapor pressure and wet area of the surface with the NLE function at the surface. This will further be investigated by the change of liquid transport mechanism, throat length and boundary layer thickness. Also the contribution of the wet and dry patches to the total evaporation rate in each of these cases will be thoroughly discussed.

Chapter 5 investigates the continuum and PN liquid velocity profiles during drying of porous media. The contribution of the main and isolated clusters as well as isolated

menisci and vapor diffusion to the transport of water towards the evaporative surface is studied. The continuum velocity field is obtained by a new type of averaging method, that is the instantaneous slice-averaged velocity profiles obtained from PNM are averaged over time. A condition for reconciling the PN and continuum velocity profiles is also given. Moreover, the velocity profiles of the stabilizing regimes are also investigated. It is shown that near the sample bottom the liquid could be completely stagnant since gas can hardly invade deeper positions of the network in stabilized regimes. It is also realized that the main reason for the occurrence of the edge effect is emptying of isolated menisci at the surface.

Chapter 6 summarizes the thesis and provides an overview of all chapters. This is followed by the outlook of this work and some suggestions related to this thesis for future research.

Chapter 2

Pore network drying model

This chapter is a modified version of a part of Attari Moghaddam et al. [2017a].

Pore network modeling is a mesoscale approach which is based on the representation of the pore space as a network of pores connected by narrow channels or throats, see Fig. 2.1. The throats correspond to the constrictions of the pore space. The pore network used in this thesis is a three-dimensional regular cubic lattice of pores and throats based on the work presented in Metzger et al. [2007b]. The numbers of nodes in x, y and z directions are N_x, N_y and N_z, respectively. The distance between the centers of two adjacent pores on the mesh a is uniform and called the lattice spacing. Throats are cylindrical tubes, whereas pores are volume-less computational nodes located at the intersection of the throats. The throat radii r_t are sampled from a normal distribution with a given mean and standard deviation. Evaporation occurs at the top of the network and the bottom is sealed. Periodic boundary conditions are imposed on the lateral faces. A boundary layer is located at the top of the network and is responsible for the gas-side diffusion of water evaporated from the network.

2.1 The drying algorithm in absence of viscous effect

In the absence of viscosity and considering gravity and capillarity as the main mechanisms for the transport of water inside the porous medium, the pore network algorithm is as follows:

1. Every liquid cluster and isolated liquid throat present in the network is identified. A liquid cluster is a set of liquid pores interconnected by liquid throats. The identification of different liquid clusters and isolated throats is done by using four different matrices, namely tnt, tnp, pnp, pnt (see Metzger et al. [2007b] for more details). These matrices provide the index numbers of all neighbors of pores and throats inside the network and in the boundary layer. By knowing the saturation values of throats and pores everywhere in the network one is able to identify different liquid clusters as well as isolated throats
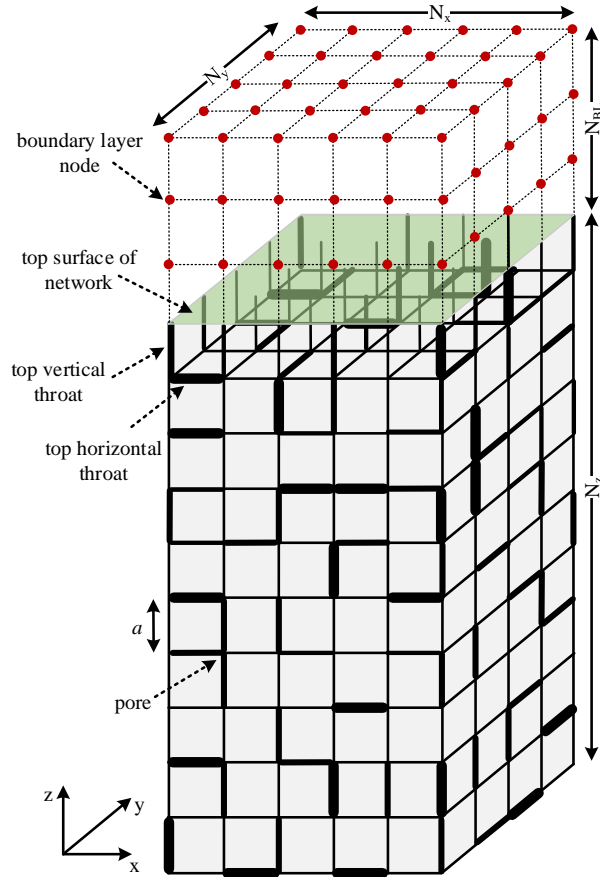
Figure 2.1: Sketch of a 3D cubic pore network with the gas-diffusion boundary layer on top.

in the network.

2. The interfacial throat (which contains a meniscus) with the highest throat potential, Φ, is identified for each cluster. This throat has the highest potential to be invaded by the gas phase. The throat potential is calculated as

$$\Phi = p_g - p_{cth} + (\rho_\ell - \rho_a)gh, \tag{2.1}$$

where p_g is the total gas pressure, ρ_ℓ and ρ_a are the density of the liquid and the air, g is acceleration of gravity and h is the height. p_{cth} is the capillary threshold and is calculated by Young-Laplace equation

$$p_{cth} = \frac{2\gamma}{r_t}cos\theta, \tag{2.2}$$

where γ is the surface tension and θ is the equilibrium contact angle (which is assumed constant in space and sufficiently smaller than 90°).

3. The evaporation rate at the boundary of each cluster and isolated liquid throat is computed. The gas phase is a binary mixture consisting of vapor and of an inert component. The evaporation rates are determined from the computation of the vapor partial pressures

in the gas-filled region of the network, assuming that the vapor flow is driven by diffusion in the gaseous pore space and can be obtained by diffusion law as

$$J_v = \frac{\pi r_t^2 \tilde{M}_v D_{va}}{\tilde{R} T L_t}(p_{v,i} - p_{v,j}), \tag{2.3}$$

where L_t, $\tilde{M}_v$, $\tilde{R}$, T, D_{va} and p_v denote length of the throat, molar mass of vapor, universal gas constant, temperature, air-vapor binary diffusion coefficient and vapor pressure, respectively. i and j are pore indices.

The numerical method for computing the vapor diffusion problem on a cubic network is similar to a classical finite difference or finite volume method used to solve the diffusion equation on a regular grid, see Metzger et al. [2007b] for more details. As also explained in Metzger et al. [2007b] and sketched in Fig. 2.1, additional computational nodes are located in a boundary layer adjacent to the evaporative surface of the pore network, where only gas diffusion is considered. This external layer represents the external mass transport boundary layer and is used to impose the difference in vapor partial pressure that drives the drying process. Saturation vapor pressure at pores neighboring to a fully or partially saturated throat as well as ambient vapor pressure at the top of the boundary layer are considered as boundary conditions for solving the vapor pressure field. As sketched in Fig. 2.1, the number of nodes in the mass transport boundary layer in the z direction is N_{BL}.

4. For each cluster, the mass loss according to the evaporation rate determined in step 3 is assigned to the interfacial throat identified in step 2. In the absence of viscosity, at each time step the throat with the highest potential is emptied. The rate of emptying of this throat is equal to the evaporation rate of the cluster in which it is located.

5. The throat eventually fully invaded is the first one to be completely drained among the interfacial throats selected in step 2 and the isolated liquid throats. Since at each time step the total number of evaporating liquid clusters plus the evaporating isolated throats could be bigger than one, there may be more than one "moving" menisci. A step is completed when the first moving meniscus is completely drained. Then the corresponding time step is calculated.

6. The phase distribution within the network is updated. The saturation of the invaded throat is set to zero and the Hoshen-Kopelman algorithm is used to relabel the liquid clusters and isolated throats. Then the pore network algorithm is restarted from step 1.

2.2 The drying algorithm in presence of viscous effect

In presence of viscosity, the algorithm is slightly different. Viscous forces would not let the water from the meniscus with the highest throat potential be easily and without any resistance pumped to the evaporating menisci of its cluster. Therefore it could happen that other menisci with lower throat potential are also emptied. In order to identify which menisci at each time step are moving, the liquid pressure field inside each liquid cluster must be solved. Therefore step 4 in the pore network algorithm for gravity-capillary regime should be changed as following:

4a. All the menisci with the highest potential in each liquid cluster as well as the partially-filled menisci are considered to be moving. The rest are assumed to be non-moving or stationary.

4b. With the known boundary conditions for stationary and moving menisci, the liquid pressure field is obtained. Here the Hagen-Poiseuille equation is used to calculate the liquid flow between two neighboring pores i and j as

$$J_\ell = \frac{\pi r_t^4 \rho_\ell}{8 \mu_\ell L_t}(p_{\ell,i} - p_{\ell,j}), \qquad (2.4)$$

where J_ℓ, μ_ℓ and p_ℓ are the liquid flow rate, viscosity and pressure, respectively.

4c. For all stationary menisci the discrepancy between inflow and outflow is calculated as: discrepancy = liquid inflow - liquid outflow.

4d. The stationary throats with negative discrepancy are identified. If the discrepancy of a meniscus is negative, its liquid outflow is bigger than the inflow, therefore it cannot stay stationary. In fact, it will be moving (emptying).

4e. The "status" of the stationary meniscus with the largest amount of negative discrepancy is changed to moving. Then a loop is built by redoing the steps 4b to 4e, until there is no more negative discrepancy.

When the moving and stationary menisci have been identified, the PN algorithm for the capillary-gravity regime can be continued with step 5. In fact, the only difference between the non-viscous and the viscous algorithm is in step 4.

Chapter 3

Macroscopic parameters in drying porous media

This chapter is partly taken from Attari Moghaddam et al. [2017b].

3.1 Introduction

Drying of porous media is a very active research area not only because a drying step is frequently encountered in many engineering processes but also because predicting accurately the drying process is still a challenge. The most frequently used approach for modeling drying in porous media is the classical continuum approach in which the porous medium is seen as a fictitious continuum (Sahimi [2011]). The history of continuum models of drying dates back to 1950s. In 1957, Philip and de Vries [1957] proposed a diffusion-based equation for the transport of moisture under temperature gradients. Later on, Luikov [1975] derived macroscopic heat and mass transfer governing equations by volumetric summation of transport equations of each species based on the macroscopic flux relationships. A comprehensive modeling was developed by Whitaker [1977] within the framework of the volume averaging method, essentially confirming the formulation of the model proposed by Philip and de Vries. For the simple drying situation considered in this chapter, namely the slow drying of a non-deformable capillary medium, the formulation of the continuum model still used nowadays is not different from the one presented in Whitaker's work. The corresponding set of equations will be presented later in this chapter. As any other continuum models, the drying continuum models involve a series of effective properties, such as permeability and effective diffusion coefficient, which must be specified as input parameters. Although widely used, such models are not truly predictive. In particular the coupling with the external transfer is generally performed through the introduction of an external mass transfer coefficient, which is in fact used as a fitting parameter. Another puzzling aspect lies in the introduction of a so-called desorption isotherm to link the saturation and the vapor partial pressure. As it was mentioned in Chapter 1, invok-

ing adsorption-desorption phenomena makes sense for hygroscopic materials but can be questioned for capillary porous media where the smallest pores are greater than about 1 μm. In other terms, we believe that the classical drying continuum model is not as solid as often considered and needs further investigation.

The fact that the continuum model is far from perfect has motivated the development of alternative approaches such as the pore network drying models, e.g. Prat [2002, 2011], Metzger et al. [2007b] and references mentioned therein. In this approach, the drying process is modeled directly at the scale of the network. Therefore pore network models can be considered as a mesoscale approach allowing the computation of the phase distribution evolution during drying directly within the pore space.

Although pore network drying models are being developed for more than twenty years now, they have not been used so far as a tool for assessing the continuum model. One a priori obvious reason is that the size of networks (in number of pores along each direction of space) is typically relatively small owing to computational limitations. As a result, it is difficult to impose a significant length scale separation (the size of a REV is actually not significantly smaller than the whole pore network), which is in principle a requirement for the continuum model to be accurate.

In spite of this issue, we believe that a comparison between pore network simulations and continuum model simulations is instructive and can bring valuable insights as regards the continuum modeling of drying. This is the main objective of this chapter.

The idea for assessing the continuum model is simple. We consider a numerical model porous medium: a cubic pore network and perform pore network simulations of drying which play the role of experiments. In other terms, we explore the ability of the continuum model to predict the results of the PN simulations of drying. Among other things, adsorption-desorption phenomena are not considered in the pore network model. Therefore, it is obviously not consistent to invoke adsorption phenomena in relation with the continuum model as far as our model porous medium is concerned.

As sketched in Fig. 3.1, the drying situation we consider corresponds to a typical laboratory experiment where the vapor forming as a result of evaporation escapes from the top surface of sample. From the continuum standpoint, this is an 1D situation whereas the situation is of course 3D as far as the PN simulations are concerned. Drying is slow, which means that the cooling effect due to evaporation can be neglected. In other terms, the temperature is considered as uniform and constant all along the drying process. Next, the one-equation continuum model is derived and macroscopic parameters are introduced.
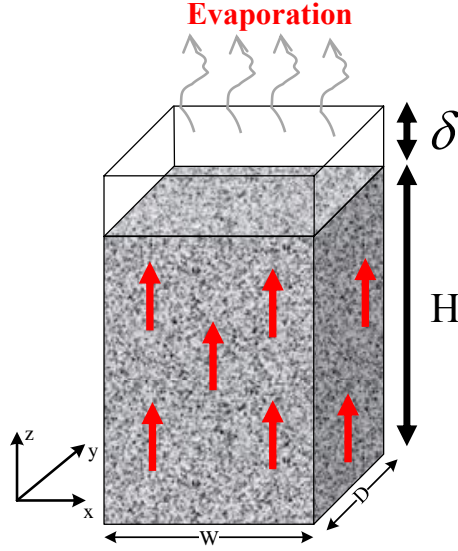
Figure 3.1: Schematic of the drying situation considered in this chapter.

3.2 Description of the one-equation continuum model

In the continuum drying model the moisture transport is considered to be dominant in direction perpendicular to the evaporative surface. Thus, the mass conservation of liquid and vapor reads, respectively

$$\frac{\partial}{\partial t}[\rho_\ell \varepsilon S] + \frac{\partial j_\ell}{\partial z} = -\dot\vartheta, \tag{3.1}$$

$$\frac{\partial}{\partial t}[\rho_v \varepsilon (1-S)] + \frac{\partial j_v}{\partial z} = \dot\vartheta, \tag{3.2}$$

where z is the upward direction and perpendicular to the evaporative surface (Fig. 3.1), $\dot\vartheta$ is evaporation rate and j_ℓ is the flux in the liquid phase which is obtained by using the generalized Darcy's law (neglecting gravity)

$$j_\ell = -\rho_\ell \frac{k_{abs}k_{r\ell}}{\mu_\ell}\frac{\partial p_\ell}{\partial z}, \tag{3.3}$$

where k_{abs} and $k_{r\ell}$ are the absolute and relative permeability of liquid phase in porous media, respectively. j_v is the water vapor flux and for isothermal drying is expressed by (Nowicki et al. [1992])

$$j_v = -\frac{\tilde{M}_v}{\tilde{R}T}\frac{p_{atm}}{p_{atm}-p_v}D_{abs}D_{rv}\frac{\partial p_v}{\partial z}, \tag{3.4}$$

where D_{abs} and D_{rv} are the absolute and relative diffusivity of vapor in porous media, respectively. In Eq. 3.4 it is assumed that the water vapor and air binary gas mixture behaves as an ideal gas.

Combining Eqs. 3.1 and 3.2 and assuming that the drying process is quasi-steady (i.e.

the vapor mass balance does not have accumulation of vapor), the 1D CM for drying in porous media reads

$$\rho_\ell \varepsilon \frac{\partial S}{\partial t} = -\frac{\partial}{\partial z}[j_\ell + j_v].$$

(3.5)

Invoking the local capillary equilibrium assumption, a relationship between liquid and capillary pressure will be obtained

$$p_c = p_{atm} - p_\ell.$$

(3.6)

Combining Eqs. 3.3, 3.4, 3.5 and 3.6, the continuum model can be written as

$$\rho_\ell \varepsilon \frac{\partial S}{\partial t} = \frac{\partial}{\partial z}\left[\rho_\ell \frac{k_{abs}k_{r\ell}}{\mu_\ell}(-\frac{\partial p_c}{\partial S}\frac{\partial S}{\partial z}) + \frac{\tilde{M}_v}{\tilde{R}T}\frac{p_{atm}}{p_{atm} - p_v}D_{abs}D_{rv}\frac{\partial p_v}{\partial z}\right].$$

(3.7)

The first term on the right hand side of Eq. 3.7 describes the liquid transport in the regions of porous medium where there is a non-zero gradient of saturation in the liquid phase, whereas the second term represents the diffusive vapor transport in the regions where the gradient of vapor concentration is non-zero.

The variables in Eq. 3.7 are S and p_v. In order to deal with only one variable and therefore solve the CM easier, one possibility is to obtain a one-equation CM by introducing a relationship between S and p_v as

$$\varphi(S) = \frac{p_v}{p_v^*},$$

(3.8)

where p_v^* is the saturation vapor pressure and $\varphi(S)$ is classically considered as the desorption isotherm of the medium. The desorption isotherm is a property of the porous medium and an input data for the CM. However, as we shall see, our interpretation of φ will be completely different. Therefore the one-equation CM can be formulated as

$$\varepsilon \frac{\partial S}{\partial t} = \frac{\partial}{\partial z}\left[\left(\frac{k_{abs}k_{r\ell}}{\mu_\ell}(-\frac{\partial p_c}{\partial S}) + \frac{p_v^*}{\rho_\ell}\frac{\tilde{M}_v}{\tilde{R}T}\frac{p_{atm}}{p_{atm} - \varphi p_v^*}D_{abs}D_{rv}\frac{\partial \varphi}{\partial S}\right)\frac{\partial S}{\partial z}\right].$$

(3.9)

At the evaporative surface, a boundary layer type relationship is generally considered to express the evaporation rate,

$$\dot{\vartheta} = \frac{\tilde{M}_v A}{\tilde{R}T}D_{va}\left(\frac{p_{v,surf} - p_{v,\infty}}{\delta}\right),$$

(3.10)

in which $p_{v,\infty}$, δ and A are vapor pressure in ambient, boundary layer thickness and

surface area of the sample, respectively. $p_{v,surf}$ is the mean vapor pressure of the surface.

A simple assumption is then to assume that Eq. 3.8 is still valid at the surface. Replacing Eq. 3.8 into Eq. 3.10 enables one to express Eq. 3.10 as a function of the saturation at the surface,

$$\dot{\vartheta} = \frac{\tilde{M}_v A p_v^*}{\tilde{R}T} D_{va} \left(\frac{\varphi - \varphi_\infty}{\delta} \right). \tag{3.11}$$

Next is the moisture transport coefficient of the CM which corresponds to the inner bracket of Eq. 3.9, namely

$$D(S) = \frac{k_{abs} k_{r\ell}}{\mu_\ell} \left(-\frac{\partial p_c}{\partial S} \right) + \frac{p_v^* \tilde{M}_v}{\rho_\ell \tilde{R}T} \frac{p_{atm}}{p_{atm} - \varphi p_v^*} D_{abs} D_{rv} \frac{\partial \varphi}{\partial S}. \tag{3.12}$$

The CM model can thus be written as

$$\varepsilon \frac{\partial S}{\partial t} = \frac{\partial}{\partial z} [D(S) \frac{\partial S}{\partial z}]. \tag{3.13}$$

Equation 3.13 is a one-equation CM, since saturation is the only variable that is considered. The first term on the right hand side of Eq. 3.12 is responsible for moisture transport in the liquid phase and is denoted by D_ℓ, whereas the second term, D_v, expresses the moisture transport in the gas phase. Therefore D can be expressed as

$$D(S) = D_\ell(S) + D_v(S). \tag{3.14}$$

Replacing Eq. 3.14 in Eq. 3.13 and comparing it with Eq. 3.5, D_ℓ and D_v can be expressed as

$$j_\ell = -\rho_\ell D_\ell \frac{\partial S}{\partial z} \rightarrow D_\ell = \frac{-1}{\rho_\ell} \frac{j_\ell}{\partial S/\partial z}, \tag{3.15}$$

$$j_v = -\rho_\ell D_v \frac{\partial S}{\partial z} \rightarrow D_v = \frac{-1}{\rho_\ell} \frac{j_v}{\partial S/\partial z}. \tag{3.16}$$

Equations 3.15 and 3.16 show that in the one-equation CM the driving force for transport in both the liquid and the gas phases is considered to be the saturation gradient.

From the above, only two parameters should be specified to solve the CM: the moisture transport coefficient D(S) and the parameter $\varphi(S)$ characterizing the dependency of vapor pressure with saturation. Methods for determining D(S) are presented in the next section, whereas the relationship between the vapor partial pressure and the saturation is discussed

in Section 3.4.3.

3.3 Determination of the moisture transport coefficient

There are several different approaches for building the relationship between D and saturation in the drying process of porous media. An old method, the so-called regular regimes, was developed by Schoeber [1976]. This approach is based on the assumption that all drying curves at a given temperature merge into one curve (regular regime curve) regardless of initial moisture content (Srikiatden and Roberts [2007]). Transient saturation profiles in drying processes can also be used to obtain the moisture transport coefficient by inverse methods. Despite of some uncertainties in the experimental techniques for producing transient saturation profiles (Roels et al. [2004]), inverse methods are widely used. A complete explanation of this method has been given in Pel et al. [1996] and will be recalled in Section 3.3.2. One of the deficiencies of this method is that reliable results for the moisture transport coefficient are obtained only if the majority of the liquid water is in the main liquid cluster. Also D cannot be determined with sufficient accuracy at low and high saturation values. In order to obtain D values at low saturation, Pel et al. [1996] developed a receding drying front method. Pel's solution for high saturation values was to perform an absorption experiment on a semi-infinite slab, and then obtain the moisture transport coefficient by using the Boltzmann transformation method (Gómez et al. [2007], Marchand and Kumaran [1994], Pel et al. [1996]). A restriction of this approach is that the hysteresis effect is neglected and the medium should be long enough to be assumed semi-infinite.

Next, three methods are introduced to determine the CM parameters from the postprocessing of results obtained from pore network drying and capillary-controlled invasion percolation (IP) simulations. The pore network model used here is the one introduced in Chapter 2 and is used throughout this thesis.

3.3.1 Extraction of moisture transport coefficient from pore network drying simulations

As a direct method for determination of the moisture transport coefficient in drying processes, pore network drying simulations are used.

The moisture transport coefficient is calculated based on the moisture transport fluxes in the liquid and the gas phase (Eqs. 3.15 and 3.16). To obtain the moisture transport fluxes and the saturation gradient that appear in these two equations, a slice-sampling method

is used on pore network results. Figure 3.2 shows a 2D schematic representation of a slice with two rows of computational nodes which is cut from the pore network. The slice size is chosen to be smaller than the network size, so that the macroscopic parameters extracted from it represent a local quantity. The liquid and gas are shown in blue and gray, respectively. In order to obtain the moisture transport coefficient in the liquid phase, only pores 7 and 2 are considered, as liquid can be transported within the slice only through these pores. Knowing nodal liquid pressures, the liquid flow rate between pores 7 and 2 can be calculated by using the Hagen-Poiseuille equation (Eq. 2.4). Then the liquid flux (j_ℓ) through the slice is obtained by the summation of J_ℓ values over all vertically neighboring liquid pores and dividing by the cross sectional area of the sample (A).
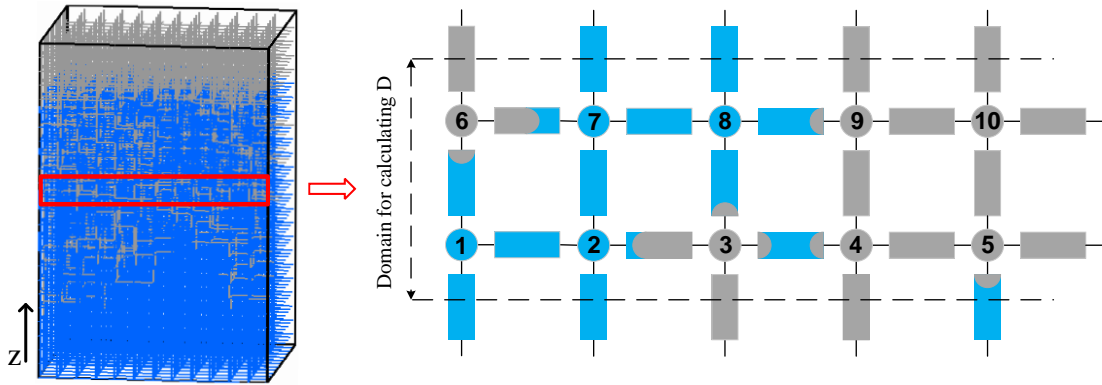
Figure 3.2: Schematic representation in 2D of a part of the slice with two rows of pores which has been used to derive the moisture transport coefficient from pore network simulations of drying.

A similar method is used to calculate the moisture transport coefficient in the gas phase. As can be seen in Fig. 3.2 different values of vapor pressure at pores 5 and 10 lead to vapor transport in the gas phase. By using the gas diffusion equation (Eq. 2.3) for all vertically neighboring gas pores, the vapor flow rate through the slice is calculated and is fed into Eq. 3.16 to obtain the moisture transport coefficient of gas phase.

3.3.2 Extraction of moisture transport coefficient from inverse method

The inverse method uses the slice-averaged saturation profiles to obtain the moisture transport coefficient. By integrating Eq. 3.13 from the bottom of the sample ($z = 0$) to the desired location z' and assuming that the spatial derivative of the saturation at the bottom is zero,

$$D(z') = \varepsilon \frac{\int_0^{z'} \frac{\partial S}{\partial t} dz}{\frac{\partial S}{\partial z}\big|_{z'}}, \tag{3.17}$$

the moisture transport coefficient at position z' is obtained. By knowing the values of saturation in each position, the final relationship between D and S is built.

3.3.3 Extraction of moisture transport coefficient from capillary-controlled invasion percolation simulations

By employing Eq. 3.12, a different method for the extraction of the moisture transport coefficient can be developed. In order to obtain D from this equation, some parameters need to be specified first; single-phase flow parameters (k_{abs} and D_{abs}), two-phase flow parameters (p_c, $k_{r\ell}$ and D_{rv}) and the closure relationship between the vapor pressure and the saturation (φ). The latter can be extracted from PN drying simulations as discussed below. The two-phase flow parameters for a drying process are obtained by the help of capillary equilibrium assumption, that is, the fluid distribution is mainly controlled by capillary, rather than viscous or buoyancy forces in a representative elementary volume (Pini and Benson [2013]). It follows that at a given local saturation the fluid configurations are the same, and so the relative permeability and diffusivity for a given system are unique functions of saturation (Wilkinson [1986]). The size of the REV is chosen in a way that it is big enough to cover all the range of throat radii and no change in the relationship between two-phase flow parameters and saturation is seen, if its size increases.

The IP model describes the quasi-steady displacement of a wetting fluid (liquid) by a non-wetting one (gas) in a REV, where the capillary equilibrium assumption is considered (Wilkinson and Willemsen [1983]). A gas reservoir is located at the top of the REV, whereas the liquid inside the porous medium is connected to a liquid reservoir at the bottom. The spatial periodic boundary condition is applied on the other sides of the REV. The gas phase from its reservoir invades into the REV, which leads the liquid phase to be discharged from the REV to its reservoir. In the standard IP, the boundary condition for the invasion of the gas phase into the REV is the flow rate. This means that, after the invasion of a certain amount of the gas phase into the REV, which is enough for emptying one meniscus, the capillary equilibrium is established. However, in order to obtain the two-phase transport parameters, the flow is considered to be capillary controlled (Lowry and Miller [1995], Rajaram et al. [1997], Svirsky et al. [2007]). Hence, in the capillary-controlled IP, multiple menisci can be invaded at the same time to reach the new capillary equilibrium state in the REV.

The algorithm for building the relationship between capillary pressure and saturation from the capillary-controlled invasion percolation simulations is as follows:

1. For simplicity and without affecting the final capillary pressure-saturation relationship, the liquid pressure in the REV and liquid reservoir are set to zero. Therefore, according to Eq. 3.6, the capillary pressure is equal to the gas pressure.

2. The smallest capillary threshold between all menisci is calculated (for explanation of capillary threshold see description of Eq. 2.1). Here a perfect wetting between liquid and solid is considered which means wetting coefficient is unity (see Cieplak and Robbins [1990] for more details regarding the IP algorithm depending on the contact angle). Therefore according to Eq. 2.2, the smallest capillary threshold according to the Young-Laplace equation belongs to the largest meniscus.

3. The gas pressure, which is equal to the capillary pressure, is increased to the smallest capillary threshold calculated in step 2 to invade the menisci with the smallest capillary threshold.

4. The newly created menisci are identified and their capillary thresholds are calculated. If the capillary pressure is bigger than the capillary threshold of any of them, they are also invaded.

5. The saturation of the REV is calculated and assigned to the capillary pressure. This is one data point in capillary pressure-saturation curve.

6. The algorithm is repeated from step 2.

Invasion of gas into the liquid phase splits the continuous connected liquid phase into several clusters of different sizes, some of which are no longer connected to the liquid reservoir at the bottom of the REV (trapped cluster). The process continues until there is no more connected cluster. The saturation of the REV at this point is called irreducible saturation (S_{irr}).

In order to extract relative permeability, at first absolute permeability is obtained and then the generalized Darcy's law (Eq. 3.3) is used. To obtain k_{abs}, saturation of the REV is set to one and then a liquid pressure gradient is applied on it. Therefore the liquid pressure field inside the REV is calculated, which is then used for obtaining the liquid flux in the REV. Then by using Eq. 3.3 and assuming $k_{r\ell} = 1$, absolute permeability is calculated. For estimation of relative permeability, at each time step of the capillary-controlled IP process and until there is still connection between liquid at the top and bottom of the REV, a similar procedure as for k_{abs} is used to calculate the liquid flux. Then Eq. 3.3 is employed.

Next the absolute and relative diffusivities are determined. The initial saturation of the REV is set to zero and a vapor pressure gradient is applied on it; the vapor pressure field inside the REV is calculated, which then gives the vapor flux inside the REV. By setting $D_{rv} = 1$, the absolute diffusivity is calculated from Eq. 3.4. In order to estimate D_{rv}, the capillary-controlled IP process is used. When gas reaches the bottom of the REV, vapor flux is calculated by the method applied for D_{abs} (considering the liquid as a barrier to vapor diffusion) and then Eq. 3.4 is used.

All the parameters discussed above are used in Eq. 3.12 in order to calculate D. Since the two-phase flow parameters are obtained as functions of saturation, D is dependent on the saturation. This method gives D for a certain range of saturation, because capillary-controlled IP continues only until irreducible saturation.

3.4 Simulation results

In this section, pore network simulation results for the extraction of the macroscopic parameters are presented. As it was mentioned, two types of pore network simulations are performed: capillary-controlled IP and PN drying simulations to extract these parameters. The drying rate curve and saturation profiles obtained from CM are then compared to the ones obtained from PN drying simulations.

3.4.1 Pore network drying simulations

Pore network drying simulations are done for 15 realizations on a network with cross section of 25 by 25 nodes and height of 51 nodes. In this way the height of the network is $50L_t$, which is the double size of its width and depth (due to the periodic boundary condition, width and depth of the network are $25L_t$). The drying conditions are chosen in a way that the liquid viscous effect plays a noticeable role. The characteristics of this series of simulations are shown in Table 3.1. Figure 3.3 shows the average normalized evaporation rate for all realizations versus network saturation (S_{net}). The constant rate period (CRP) is not seen because of relatively strong viscous effect. The average change of saturation versus time among all realizations is shown in Fig. 3.4.

Table 3.1: Characteristics of PN drying simulations.

Parameter	Value
Network discretization	$25 \times 25 \times 51$ nodes
Boundary layer discretization	$25 \times 25 \times 10$ nodes
Number of realizations	15
Mean throat radius	250 μm
Standard deviation of throat radius	25 μm
Throat length	1 mm
Viscosity	28 Pa.s
Sample porosity	0.594
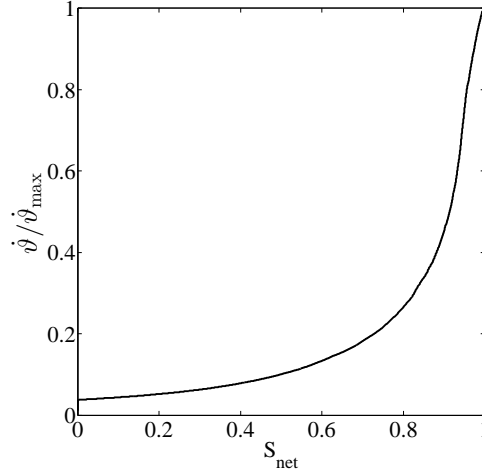
Figure 3.3: Normalized evaporation rate averaged among 15 realizations for a network of $25 \times 25 \times 51$ nodes.
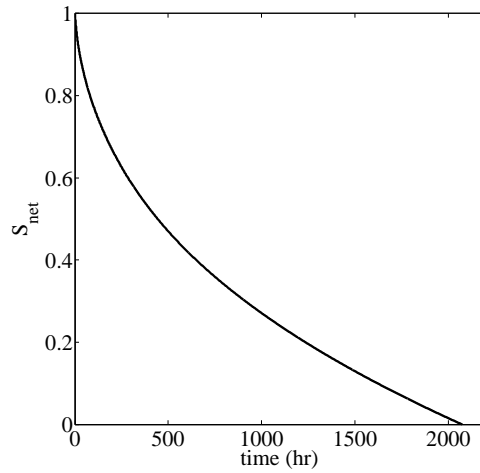
Figure 3.4: Change of saturation versus time averaged among 15 realizations for a network of $25 \times 25 \times 51$ nodes.

3.4.2 Capillary-controlled invasion percolation simulations

As it was mentioned in Section 3.3.3, capillary-controlled invasion percolation simulations are carried out on a REV. The size of REV is $25 \times 25 \times 25$ nodes, in which the values of two-phase flow parameters have negligible fluctuation. Besides, these parameters stay unchanged by increasing the REV size to more than $25 \times 25 \times 25$ nodes. From each original network 3 REVs are cut and therefore simulations are done on 45 REVs in total. The cross sections of REVs are the same as those of the original networks, therefore in order to have REVs with different throat radii distribution, they are cut from different heights of a network as follows: the first REV is cut from pore 1 (bottom) to pore 25, the second REV from pore 13 to 38 and the third REV from pore 26 to 51 (top) in z direction. The average values of absolute permeability and diffusivity are $1.6 \times 10^{-9} \pm (7 \times 10^{-13}) m^2$ and $5 \times 10^{-6} \pm (1 \times 10^{-9}) m^2/s$, respectively.

(a)

(b)

(c)
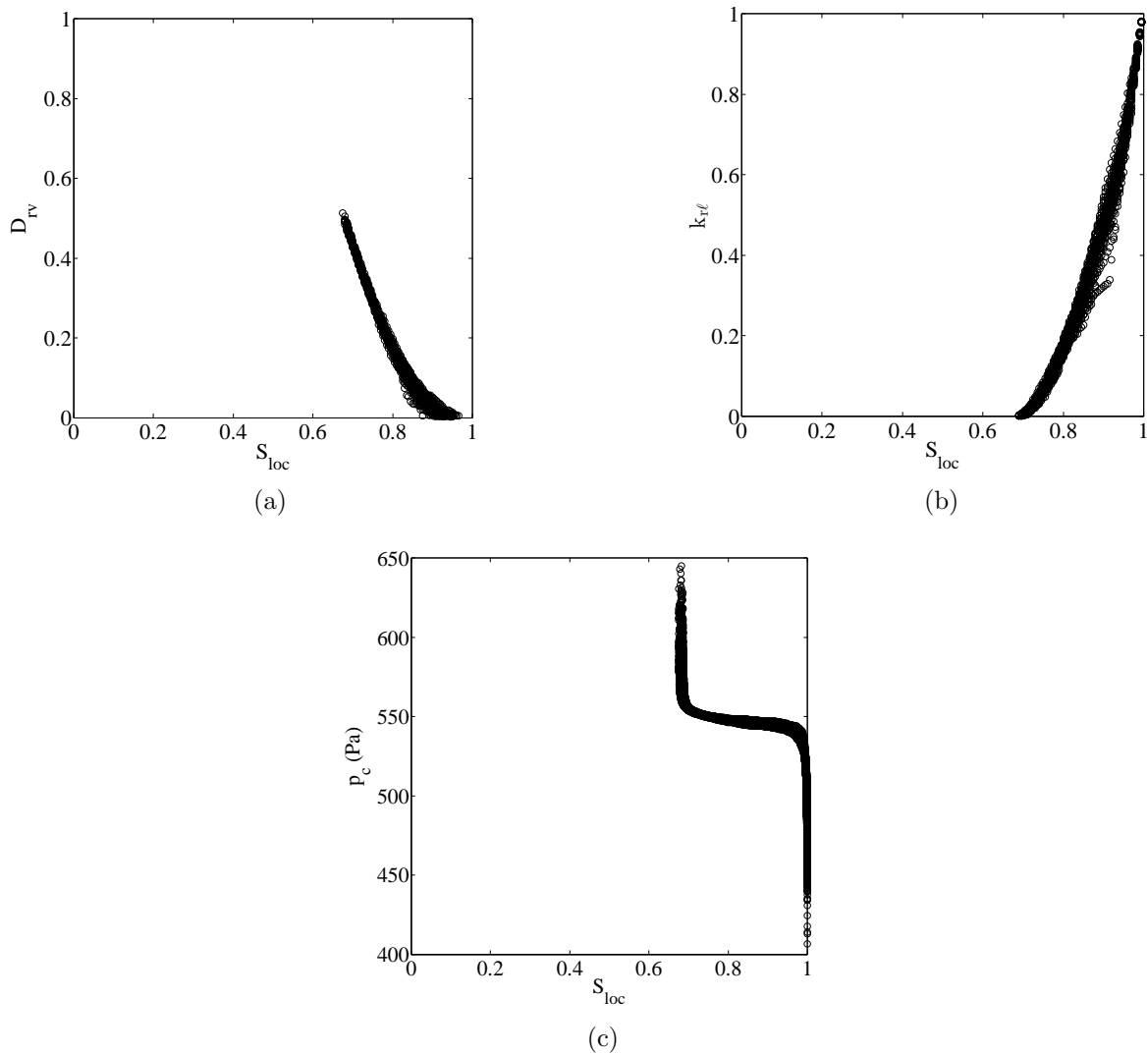
Figure 3.5: Relative permeability (a), relative diffusivity (b) and capillary pressure (c) for the REV of size $25 \times 25 \times 25$ nodes.

The data points obtained from all realizations for capillary pressure, relative permeability and diffusivity versus local saturation (S_{loc}) are shown in Fig. 3.5. The irreducible saturation in capillary-controlled IP simulations is $0.68 \pm (4 \times 10^{-4})$ and that is the reason there is no data for saturations smaller than that in these curves. The high irreducible saturation is due to the cubic structure of network and the fact that the pores are volumeless (the fluids are in the throats) in our pore network model. When the REV is fully saturated, capillary pressure is at its minimum and the conductivity of the liquid inside the REV is completely established, meaning relative permeability is one, whereas relative diffusivity is zero. Bigger throats are invaded as invasion of gas into the REV continues, leading to increasing capillary pressure. This is followed by a reduction in the conductivity of the liquid, which consequently leads to a continuous decrease in relative permeability and an increase in relative diffusivity, until no invasion is possible anymore.

In order to obtain the moisture transport coefficient from two-phase flow parameter re-

sults, a discrete approach is used as follows: First the saturation interval between 0 and 1 is divided into 200 sub-intervals. The centers of these sub-intervals are discrete S_{loc} values. Then, in each sub-interval, average values of $k_{r\ell}$, D_{rv} and dp_c/dS_{loc} over all realizations are calculated and fed into Eq. 3.12 to extract the values of D at discrete S_{loc} values. The moisture transport coefficient data obtained in this way, as well as two-phase flow parameter results are documented in an electronic appendix.

3.4.3   Vapor pressure-saturation relationship

Figure 3.6 shows an example of slice-averaged vapor partial pressure and saturation along the network obtained from the pore network drying simulations. The slice-averaged saturation is computed by summing up the liquid volume in an x-y plane of horizontal throats plus half of the volume of vertical throats connected to this plane and dividing it by the total pore space volume in the slice (except the very first slice which contains not half but the full volume of the vertical throats connected to the network surface, see Fig. 4.1). The vapor pressure of the slice is the average of vapor pressure of pores in the corresponding x-y plane. As can be seen from Fig. 3.6, the average vapor pressure is not equal to saturation vapor pressure in the presence of liquid over a noticeable range of saturation. Since adsorption-desorption are completely absent in our numerical model porous medium, it is absolutely clear that the fact that the vapor pressure is less than the saturation vapor pressure in the presence of liquid, i.e. at non-zero saturation, has a different physical origin. It is interpreted here as the signature of a non-local equilibrium effect. In the framework of the continuum approach to porous media, NLE means that the local thermodynamic equilibrium is satisfied at the menisci surface (where the vapor pressure is thus the saturation vapor pressure) but not at the scale of the REV where the average vapor pressure is different from the saturation vapor pressure in the presence of liquid within the REV. This is an important difference from the conventional presentation of the continuum model. Here, the function is therefore not interpreted as a desorption isotherm but as a NLE relationship.

Figure 3.7 shows φ data points averaged over small local saturation intervals at different network saturations. It can be seen that a unique function φ cannot be defined over the whole drying process. Thus φ does not stay unchanged during the drying process, and it can be seen that φ goes to unity as the network saturation approaches zero. This may be due to the breakage and more uniform lateral distribution of liquid at these saturations which may result in higher vapor pressures in gas pores in the two-phase region, the thickness of which increases as it travels further into the depth of the network. This can be explained by Fig. 3.8, in which the ratio of the contribution of isolated menisci to the total network saturation is shown. By decreasing S_{net} and reducing the evaporation rate, the liquid transport due to capillary forces is enhanced. Large liquid clusters are
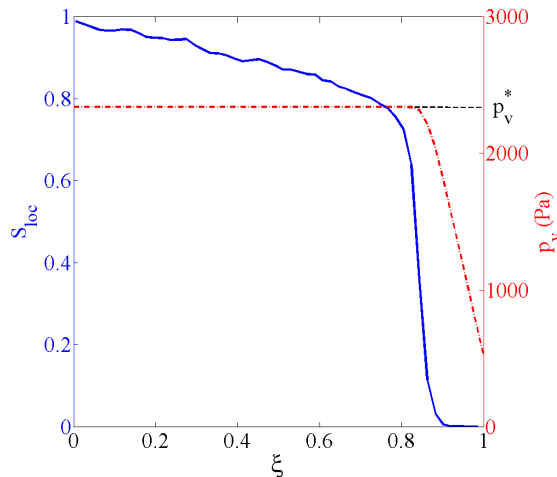
Figure 3.6: Profiles of slice-averaged vapor pressure and saturation from PN simulations at network saturation 0.75, averaged among all realizations.

invaded by gas and thus more isolated menisci are created. This results in a more uniform distribution of liquid inside the network compared to higher network saturations and, therefore, local mean vapor pressure may be closer to the saturation vapor pressure.
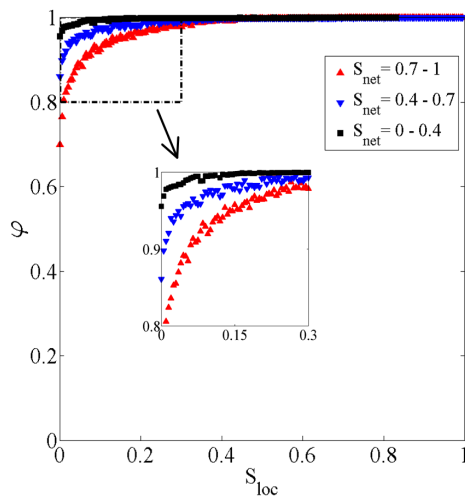
Figure 3.7: Mean value of φ for the network of $25 \times 25 \times 51$ nodes obtained from PN drying simulations at different network saturations averaged over small local saturation intervals.

The PN simulations indicate that a NLE effect is also present at the surface. The NLE function at the network surface (φ_{surf}) is shown in Fig. 3.9. Comparing these results with φ, it is clear that these two functions are different, although they follow a similar trend. The smaller values of φ_{surf} than φ at a given saturation are due to the fact that at the surface the vapor pressure is directly affected only by the liquid in the first layer of the network, while vapor pressures of the nodes inside the network are influenced by the liquid at their top and bottom layers. Therefore for a given saturation of a layer, vapor pressure of the surface is expected to be smaller compared to any other position inside the network.
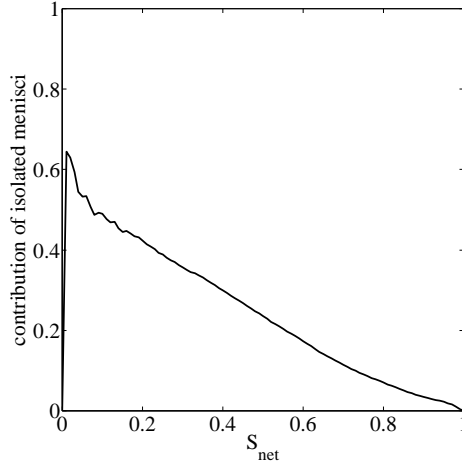
Figure 3.8: Contribution of isolated menisci versus total network saturation averaged among 15 realizations for a network of $25 \times 25 \times 51$ nodes.
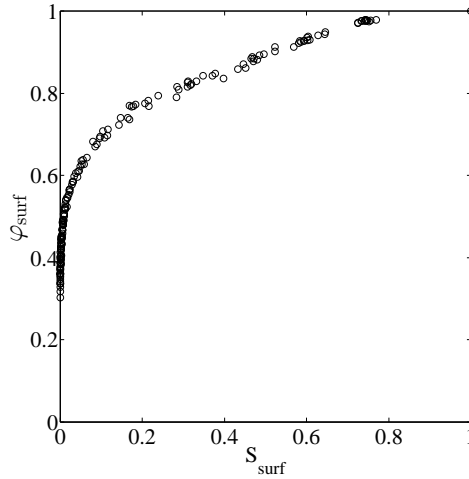
Figure 3.9: φ_{surf} for the network of $25 \times 25 \times 51$ nodes obtained from PN drying simulations.

This is also a noticeable departure from the conventional continuum modeling of drying, which is based explicitly on the local equilibrium assumption through the consideration of the desorption isotherm and the implicit assumption that the desorption isotherm is still valid at the surface.

3.4.4 Moisture transport coefficient

The moisture transport coefficients for the gas and the liquid phase as well as the total moisture transport coefficient obtained from PN drying simulations, averaged over small local saturation intervals, are shown in Fig. 3.10. The results show that all types of moisture transport coefficient depend on the network saturation at middle and lower local saturations ($S_{loc} < 0.68$). At high local saturation ($S_{loc} > 0.68$), the dependency of D on the network saturation is not clear though and data points are sparse, which is due to the fluctuations of liquid pressure. In this range of local saturation, the mean local vapor pressure everywhere in the network is close to p_v^* and no vapor pressure gradient

can be established, therefore the transport is only through the liquid phase. This can be confirmed by looking at the ratio of local liquid flux (J_ℓ) over total local flux (J), shown in Fig. 3.11. For $S_{loc} > 0.68$, $J_\ell/J = 1$, therefore vapor flux and moisture transport coefficient in the gas phase are zero. From this point on, by decreasing the local saturation, the vapor pressures of gas pores deviate from saturation vapor pressure and more paths for the vapor transport become available, which leads to a stronger contribution of the gas phase to the total flux and consequently, increasing D_v. The increase in D_v by reducing the local saturation can also be clarified by the NLE function φ data, shown in Fig. 3.7. As can be seen, the derivative of φ over S_{loc} becomes bigger by reducing the local saturation, which results in bigger D_v (Eq. 3.12).

(a)

(b)

(c)
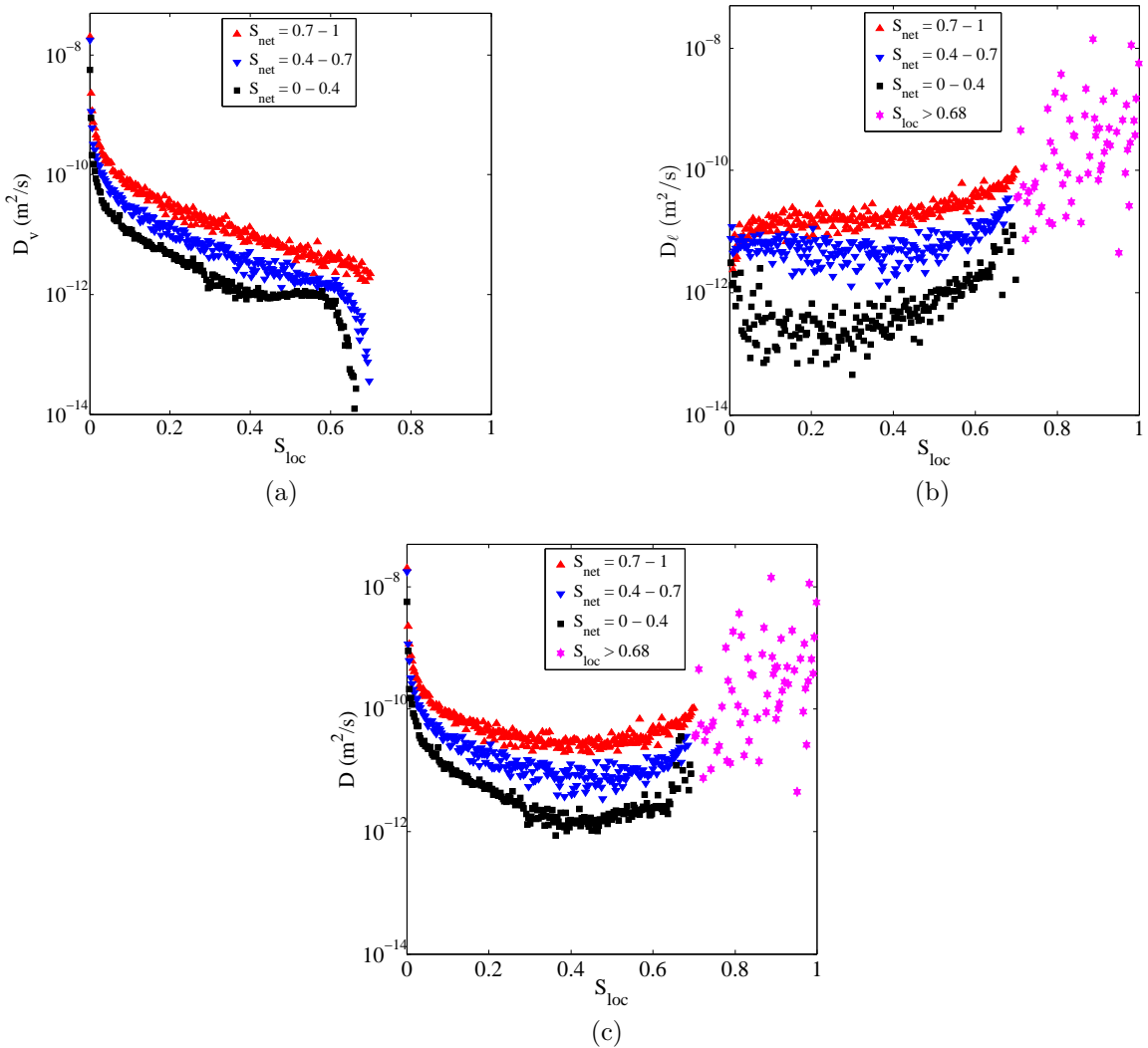
Figure 3.10: The moisture transport coefficients for the gas (a) and the liquid (b) phase as well as the total moisture transport coefficient (c) obtained from PN drying simulations, averaged over small local saturation intervals.

In Fig. 3.10a, it is clear that by decreasing the network saturation, D_v at a specified local saturation decreases as well. The change in the ratio of isolated menisci over network saturation, shown in Fig. 3.8, can explain this behavior. At lower S_{net} the relative
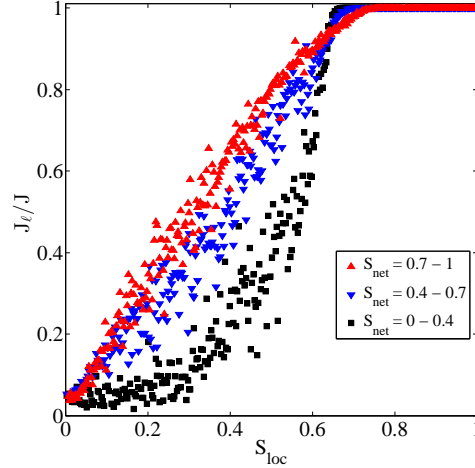
Figure 3.11: The ratio of liquid flux over the total flux inside the porous sample during drying.

amount of isolated menisci is bigger and liquid is more uniformly distributed. Therefore, when going from one layer to its neighboring layer the vapor pressure drop is expected to be smoother, which leads to a smaller vapor flux and D_v. The deeper position of the drying front at lower S_{net} is also a reason for reduction in the moisture transport coefficient of the gas phase.

At $S_{loc} = 1$, the hydraulic conductivity of the liquid is at its maximum, therefore moisture transport coefficient in the liquid phase has the highest value (Fig. 3.10b). By decreasing the local saturation, the continuity of the liquid phase is affected and thus D_ℓ is reduced. When the local saturation becomes smaller than 0.68, the liquid pressure profile is developed and the dependency of D_ℓ on network saturation is clearer. Similar to D_v, the dependency of D_ℓ on the network saturation can be explained by the presence of isolated menisci. At higher S_{net}, the majority of liquid is in the main cluster, making the transport of liquid easier. This results in a higher liquid flux and moisture transport coefficient. However, at low S_{net}, the contribution of the isolated menisci to the network saturation is bigger (Fig. 3.8), thus a smaller part of liquid can effectively contribute to the liquid transport and, consequently, D_ℓ will be lower. That also explains the dependency of the transition point between dominant phases for the transport with S_{net}. This point corresponds to the saturation at which $J_\ell/J = 0.5$ and represents the equivalence of the contributions of the gas and the liquid phase to the transport. With decreasing S_{net}, which leads to an increasing number of isolated menisci, the local saturation at which the transition happens becomes bigger (Fig. 3.11).

As can be seen in Fig. 3.10b, when local saturation $S_{loc} < 0.2$ a different behavior in D_ℓ at different network saturations is observed. With S_{loc} decreasing to values below 0.2, the moisture transport coefficient in the liquid phase increases at low network saturations, whereas the opposite behavior is observed at higher network saturations. Since the majority of liquid in the latter case is in the main cluster, decreasing the local saturation leads to lowering the effective paths for the transport of liquid. This consequently leads

to a reduction of the moisture transport coefficient in the liquid phase. But at lower network saturations, for $S_{loc} < 0.2$, it is more likely that by decreasing the local saturation the amount of isolated menisci is reduced, because they compose the larger part of the liquid. This means that the effective paths for the transport of liquid may stay almost unchanged. Knowing that the spatial gradient of saturation decreases by decreasing the local saturation below 0.2 (see Fig. 3.17) and assuming that J_ℓ stays constant in this range, then according to Eq. 3.15, D_ℓ should increase. It is only by using a pore scale model such as a pore network that this opposing behavior can be detected.

The lumped moisture transport coefficient, i.e. $D_\ell + D_v$, is shown in Fig. 3.10c. For all network saturations, a minimum in D is observed. The saturation at which this minimum occurs (S_{min}) is almost equal to the transition saturation at which $J_\ell/J = 0.5$ (Fig. 3.11). In the region in which saturation is higher than S_{min}, the liquid transport is more significant (D_ℓ is bigger), while at lower local saturations vapor transport plays a more important role (D_v is bigger). Interestingly, the trend depicted in Fig. 3.10c is in qualitative agreement with the experimental determination of D, D_v, D_ℓ for a sand sample reported in Crausse et al. [1981].

The lumped moisture transport coefficient has also been obtained by using the saturation profiles, applying the inverse method (Section 3.3.2). The results obtained using the average saturation profiles among all realizations (documented in an electronic appendix) are shown in Fig. 3.12. It is seen that the inverse method is able to predict the trend of the moisture transport coefficient. However, at lower network saturations there are some deviations in the values of D compared to the results obtained from PN drying simulations. Take for example the values for $S_{net} < 0.4$ obtained from these two methods which are shown in Fig. 3.13. In this range of network saturation, the inverse method produces bigger values compared to the results from PN drying simulations for $0.2 < S_{loc} < 0.6$. The reason for this discrepancy is that when calculating the slice-averaged saturation profiles, all amount of liquid water which is present in the network (liquid in the main cluster, isolated clusters and isolated menisci) is taken into account. Therefore, when calculating the moisture transport coefficient from the inverse method, different types of liquid are not distinguished. In fact, the liquid is considered to form a continuous phase everywhere that $S_{loc} > 0$. But as it has already been explained, during drying the contribution of liquid in isolated menisci and isolated clusters to the moisture transport is smaller compared to that of the main cluster. Therefore, the inverse method overestimates the liquid transport inside the porous media during drying by considering all the liquid in one cluster. This, however, is not the case for the results obtained from the PN drying simulations, because there liquid of different types is distinguished through the detailed phase distribution at the pore scale.

The discrepancy between the results obtained from the inverse method and the PN drying simulations at higher saturations is negligible, though. This is due to the fact that at
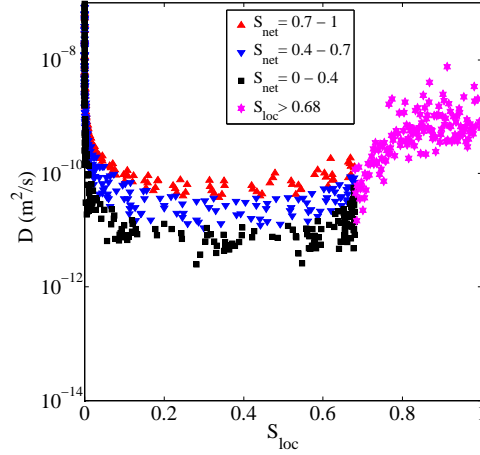
Figure 3.12: Moisture transport coefficient obtained from the inverse method.
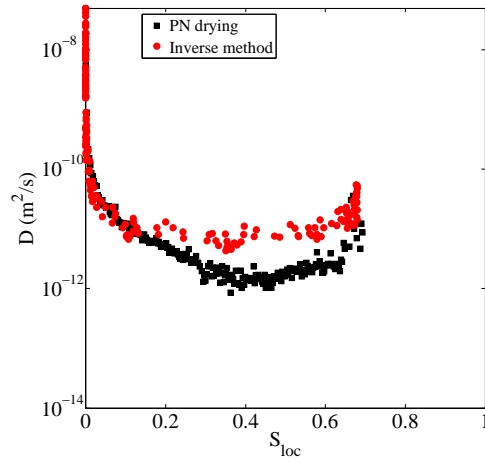
Figure 3.13: D obtained from PN drying simulations and the inverse method for total saturation smaller than 0.4.

higher saturations the liquid is mainly located in the main cluster, whereas the percentage of liquid in isolated clusters and menisci is small. Thus, it is important to note that the inverse method can be expected to generate reliable moisture transport coefficient results only if the amount of liquid in isolated clusters and menisci is small enough compared to the liquid in the main cluster.

As mentioned before, for the estimation of D, capillary-controlled invasion percolation simulations can also be used. In this method, the results of two-phase flow as well as one-phase flow parameters and the NLE function φ are used to estimate D. The moisture transport coefficient obtained from this method is shown in Fig. 3.14. Values of D are obtained until S_{irr}, since the capillary-controlled IP process stops at this saturation. As it was mentioned before, the vapor transport in the gas phase for $S_{loc} > 0.68$ is negligible and therefore the data points are actually showing the moisture transport coefficient in the liquid phase.

Comparing Figs. 3.14 and 3.10c, it is concluded that trends of D data points obtained from the two methods are in agreement, although their values for very high local sat-
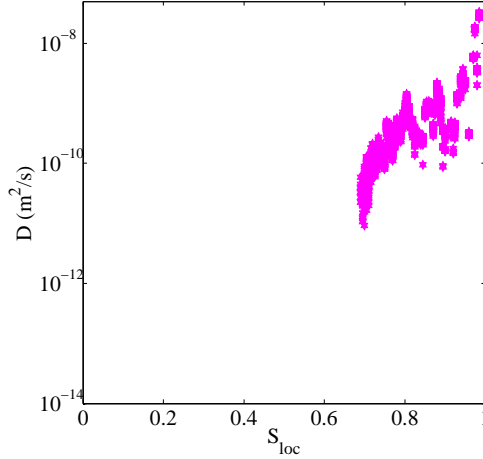
Figure 3.14: D obtained from capillary-controlled IP simulations.

urations deviate somewhat from each other. This behavior is due to the smaller liquid flux predicted by PN drying simulations at $S_{loc} > 0.9$. In this range of local saturations, because of the small number of menisci, the liquid pressure field calculated from PN drying simulations is not completely developed. Therefore the gradient of liquid pressure between two vertically neighboring liquid pores towards the evaporative surface could be positive. This reduces the total liquid flux through the slice. But in capillary-controlled IP simulations, the liquid pressure field will be uniform, since the liquid boundary conditions are not imposed by menisci. Thus a higher liquid flux and D_ℓ are produced from capillary-controlled IP simulations, which are not reflecting the real behavior seen during drying. Therefore the data obtained from PN drying simulations are used to solve the CM.

3.4.5 Comparison of continuum model with pore network simulation results

The moisture transport coefficient and the NLE surface function are directly used for solving the one-equation continuum model (Eqs. 3.13 and 3.11). When solving these equations, local saturations can reach very small values, for which no values of D and φ_{surf} obtained from PN drying simulations are available. This is due to the fact that slice-averaged saturation can be captured only until a certain positive value, therefore the values of these two parameters are unknown for very small local saturations.

A solution may be to increase the network size, so that aforementioned parameters can be calculated for lower slice saturations. This solution however increases the computational time and might not solve the problem completely, since the local saturations in CM could still become lower than the smallest saturation of the slice. Another solution would be to calculate the receding velocity of the drying front and use it to determine values of D at very low saturations as proposed by Pel et al. [1996].

In this work, in order to obtain values of D at very low local saturations, a new solution based on the evaporation rate of PN drying simulations is used. In order to do so, first curves are fitted to the available data points of moisture transport coefficient and NLE function at the surface. Due to the high non-linearity of D values and in order to produce fitted curves with high accuracy, the fitted curve to the D data points for each range of the network saturation consists of several curves, each of which covers a small range of local saturations, see Fig. 3.15. After fitting curves to the data points of moisture transport coefficient and NLE function at the surface, the discretized one-equation continuum drying model is solved. When the saturation of the surface becomes very small, for which D and φ_{surf} values are not available ($S_{surf} < 2 \times 10^{-4}$), the averaged evaporation rate of PN drying simulations is applied as the boundary condition. Then D for the corresponding surface saturation is obtained, providing the mass conservation at the surface is met. In this way, the moisture transport coefficient of any other node with $S_{loc} < 2 \times 10^{-4}$ can be obtained. Then a curve is fitted on all data points of D. By applying the same procedure for the evaporation rate and using the new fitted curve for D, this time the CM can be solved without any limitation until the network dries out completely. The CM was solved using an explicit finite difference scheme with variable time step and uniform grid (200 computational nodes in z direction).
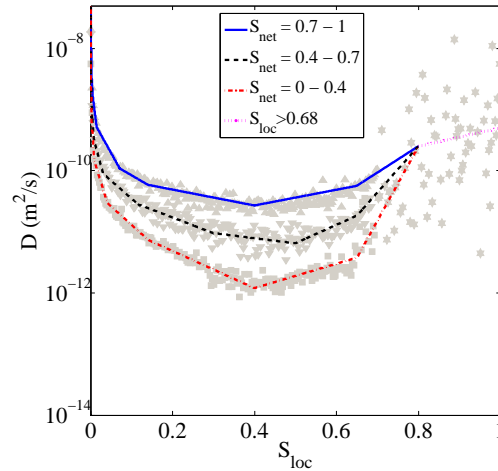
Figure 3.15: Fitted curves to the moisture transport coefficient data points used for solving the one-equation CM. The gray symbols show their corresponding data points (Fig. 3.10c).

The normalized averaged evaporation rates predicted by the CM (Eq. 3.11) and by the PN drying simulations are shown in Fig. 3.16. The CM predicts the evaporation rate until data points of φ_{surf} are available ($S_{net} \approx 0.85$) and afterwards the evaporation rates of PN drying simulations are used as boundary condition in the CM. As can be seen, the evaporation rate curves resemble each other very well. This of course only shows that the CM model can reproduce the data and is by no means a proof that the CM model can predict the evaporation rate. This important point is further discussed below. The saturation profiles obtained from the two methods are plotted against the normalized network depth (ξ) in Fig. 3.17. As can be seen, the CM is able to reproduce the saturation

profiles of PN drying simulations.
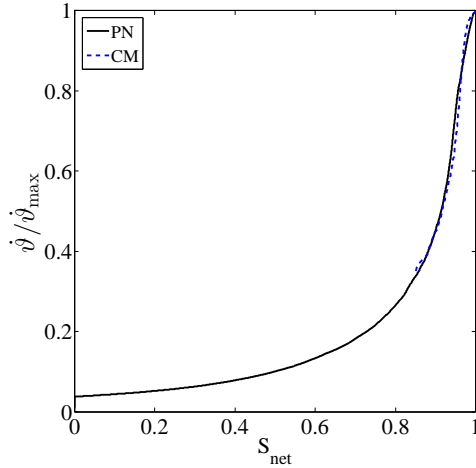
Figure 3.16: Evaporation rate predicted by Eq. 3.11 and PN drying simulations.
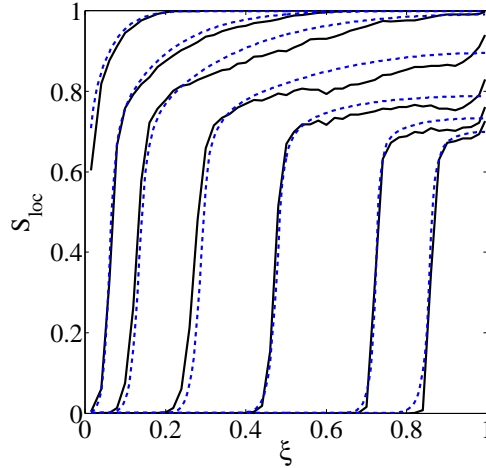
Figure 3.17: Saturation profiles obtained from CM (blue dashed lines) and PN (black solid lines) drying simulations. The saturation profiles of PN are averaged among 15 realizations. From top the profiles belong to network saturations of 0.98, 0.9, 0.8, 0.6, 0.4, 0.2 and 0.1, respectively.

Since the CM model is able to reproduce the PN simulation results, it is tempting to consider that the results presented before confirm the overall validity of the CM model. Accordingly, the main problem would be simply a correct determination of macroscopic parameters. With the permanent progress in imaging techniques (X-ray microtomography, FIB-SEM, etc.), e.g. Bultreys et al. [2016], Wang et al. [2012], and as regards the techniques for extracting pore networks from digital images of microstructures, e.g. Agaesse et al. [2016], it would be just a matter of time to determine accurately these parameters from high performance pore network computations. However, we believe that the conclusion one must draw from the results presented in this section is completely different as discussed here.

Compared to the current state of the art concerning the drying CM, the results presented in the previous section show several differences. The moisture transport coefficient

function D(S) is not unique (as illustrated in Fig. 3.10). We actually used three different functions depending on the average saturation of the medium. However, as already mentioned, the general shape of the function D(S) is in qualitative agreement with the experimental determination of this function (Crausse et al. [1981]). It is unclear whether the fact that we did not obtain a unique function of saturation is due to the small size of our network which implies a poor length scale separation between the REV size and the sample size. More interestingly and more importantly in our opinion, the pore network simulations indicate a significant non-equilibrium effect, i.e. the average vapor pressure is lower than the saturation pressure when the saturation is sufficiently low but non zero in the REV (a horizontal slice containing one row of pores in this case). This phenomenon is generic and expected not to be an artifact of the small size of network. Also, we had to consider a NLE function at the surface, different from the one inside the network, and the NLE function inside the two-phase region was not unique. Even if we assume that repeating the work over much bigger networks would lead to a unique internal NLE function, the consequence would be that the present version of the drying CM is intrinsically not adapted to model the drying process in our network. The existence of the NLE effect is a strong indication that a NLE two-equation model would be much more appropriate. Contrary to the classical CM where the equations describing the transport in liquid phase and in vapor phase are combined to obtain a single transport equation, liquid and vapor transport would be kept separate in the two-equation model and a source-sink term would take into account the NLE exchange between the phases, e.g. Casciatori et al. [2016]. A simplified version of the two-equation model assuming the liquid phase to be immobile is presented in Pujol et al. [2011]. The comprehensive version is yet to develop.

The fact that the surface NLE function φ_{surf} is different from the internal NLE functions φ is interpreted as a strong illustration of the problem posed by the adequate description of the transfer at the surface where the internal and the external transfer must be coupled. The modeling of the transfer at the surface is often seen as the major problem of the theory of drying and the present results can be regarded as an additional confirmation that more work on this topic is needed.

Now there is the question of the representativeness of our pore network model compared to real systems. Since the main new aspect is the NLE effect, the question arises whether the NLE effect might be only a consequence of the model. As discussed in Vorhauer et al. [2015], it is relatively well established that secondary capillary structures can form during the invasion of the pore space by the gas phase as a result of evaporation. Secondary capillary structures refer to capillary bridges, rings, liquid films forming in wedges, contact regions between particles, constrictions and other geometrical singularities of the pore space. The formation of the secondary capillary structures strongly depends on the local geometry of the pore space and wettability properties (the lower the contact angle, the more likely the formation of secondary capillary structures). The formation of secondary

capillary structures can be considered as taken into account in the pore network model used in the present paper since liquid can be temporarily trapped in single throats, but its effect might be more important in some real systems. The impact of secondary capillary effects on the NLE effect in real systems would therefore deserve to be studied in more detail.

3.5 Macroscopic parameters in large networks

One of the main advantages of the one-equation continuum model compared to the pore network modeling of drying is that for large (industrial) sample sizes (in terms of number of pores along each direction of space) the computational effort needed to obtain the kinetics and saturation profiles is very small. Therefore, it is highly popular to use the continuum model when dealing with large network sizes. However, as it has been discussed in Section 3.2, the determination of the macroscopic parameters is crucial when using the CM.

The network considered in the previous section was composed of $25 \times 25 \times 51$ nodes. However, the number of pores along each direction in industrial capillary porous samples, e.g. bricks, could be much larger than the number of pores for the sample considered here (Defraeye [2014]). Therefore, the question arises, how the methods explained in this work can be used to predict the macroscopic parameters of big samples.

With a personal computer with the configuration stated in Table 3.2, the computational time needed for pore network drying simulation of one single realization for the reference network of $25 \times 25 \times 51$ nodes in viscous-capillary regime is about 30 hours. The computational time increases to 7 days by increasing the network size by a factor of four (network of $50 \times 50 \times 51$ nodes) and is expected to increase exponentially with further increase in the size of the network. Such a jump in computational time by increasing the network size only by four times, suggests that PN drying simulation of samples one or two orders of magnitude bigger than the reference network could take even years with the current computational facilities (see explanations in Section 3.5.2 for the network of $100 \times 100 \times 101$). Not considering that simulations should be done on several, and not only one, realizations to damp the effect of randomness of the throat size distribution.

Table 3.2: Main characteristics of the PC used for running the simulations.

Component	Model
Processor	INTEL 1150 Core i7-4790K
RAM	2×DDR3 16GB 1600
Hard disk	250GB SSD + 1000GB HDD

Therefore, it is practically impossible to apply the numerical analysis which is based on the PN drying simulations to obtain the macroscopic parameters for a large sample. How-

ever it is possible to study the trend of change of macroscopic parameters with increasing network size, although within a limited range of network sizes, to see whether a "representative network size" can be identified. A network size can be considered as representative, when the macroscopic parameters do not change upon further network size increase (Fatt [1956]). Next, we will investigate this possibility in our simulations.

3.5.1   Effect of network size on macroscopic parameters

In order to investigate the effect of network size, first PN drying simulations on 10 realizations for a network of $50 \times 50 \times 51$ nodes were performed. The other geometrical and physical parameters are considered unchanged compared to the previous simulations. The evaporation rate and saturation profiles of this network and the reference network (with $25 \times 25 \times 51$ nodes) are shown in Figs. 3.18 and 3.19. The results show that the phase distribution and kinetics during drying of these two networks are very similar. The reason for this behavior is that the reference network has already a "big enough" cross section and its depth is the same as the depth of the network with $50 \times 50 \times 51$ nodes. Considering that macroscopic behavior in these two networks is similar, it is therefore expected that their macroscopic parameters are also close to each other.
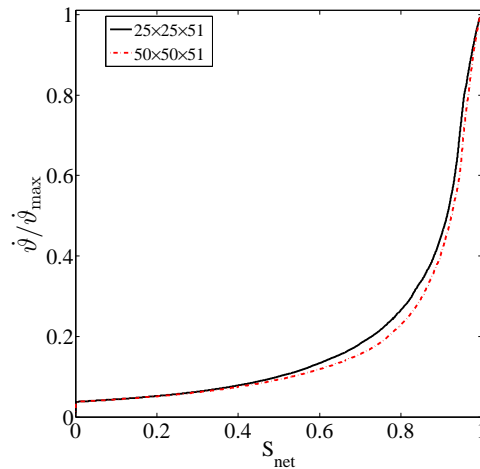
Figure 3.18: Averaged normalized evaporation rate for networks of $50 \times 50 \times 51$ and $25 \times 25 \times 51$ nodes.

The NLE function inside the bigger network is shown in Fig. 3.20. The results are in very good agreement with the NLE function of the reference network shown in Fig. 3.7. The NLE function at the surface for both networks is also depicted in Fig. 3.21. As it has already been illustrated, the evaporation rate curves of the two networks are similar (see Fig. 3.18). Therefore it is expected that their φ_{surf} values also resemble each other, as shown in Fig. 3.21.
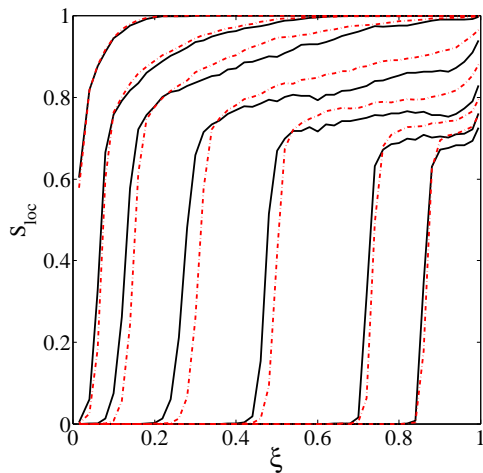
Figure 3.19: Saturation profiles obtained from PN drying simulations on network of $50 \times 50 \times 51$ nodes (red dashed lines) and $25 \times 25 \times 51$ nodes (black solid lines). The saturation profiles have been averaged among all realizations. From top the profiles belong to network saturations of 0.98, 0.9, 0.8, 0.6, 0.4, 0.2 and 0.1, respectively.
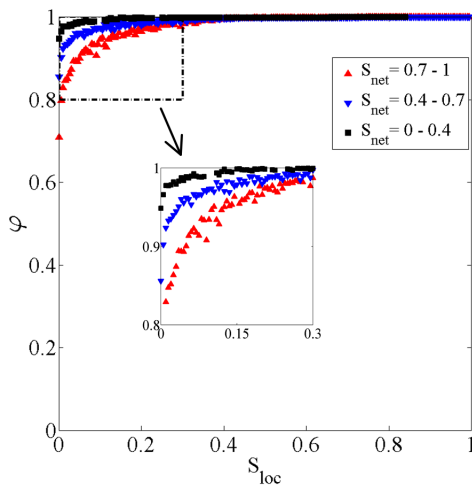
Figure 3.20: Mean value of φ for the networks of $50 \times 50 \times 51$ nodes obtained from PN drying simulations at different network saturations averaged over small local saturation intervals.
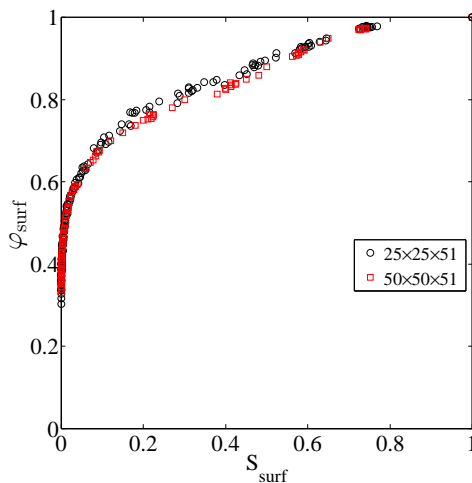
Figure 3.21: φ_{surf} obtained from PN drying simulations for two networks.

The moisture transport coefficients in the gas and the liquid phase, as well as the lumped moisture transport coefficient for the network with $50 \times 50 \times 51$ nodes are shown in Fig. 3.22. Since the NLE functions for the network of $50 \times 50 \times 51$ nodes are similar to the ones for the reference network (see Figs. 3.7 and 3.20), D_v values are also expected to be similar for both networks (according to Eq. 3.12, $D_v \propto d\varphi/dS_{loc}$). Also similarly to the reference network, D_v values for $S_{loc} > 0.68$ are zero, since the local average vapor pressure at these saturations is p_v^*. The moisture transport coefficient for the liquid phase and the lumped moisture transport coefficient for the network with $50 \times 50 \times 51$ nodes also resemble the values of the reference network, owing to the similar geometrical characteristics as well as drying rate curves and saturation profiles. It can thus be concluded that the macroscopic parameters of the reference network can be used for the continuum modeling of the drying process of the bigger network with $50 \times 50 \times 51$ nodes.
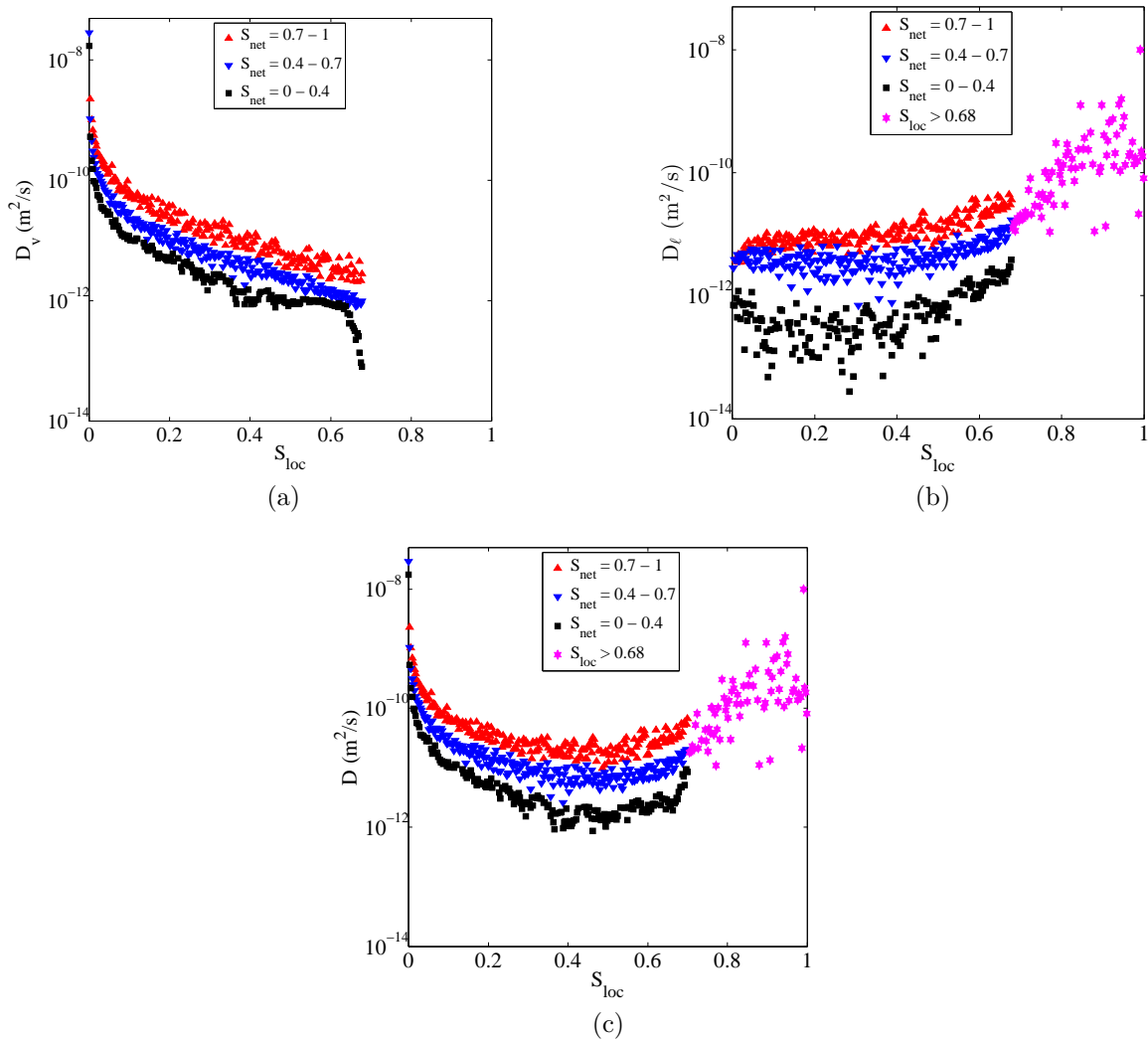
Figure 3.22: Moisture transport coefficients for the gas (a) and the liquid (b) phase as well as the total moisture transport coefficient (c) obtained from PN drying simulations on the network of $50 \times 50 \times 51$ nodes, averaged over small local saturation intervals.

Although the network with $50 \times 50 \times 51$ nodes is four times bigger than the reference

network, it is still much smaller than industrial porous samples (in terms of number of pores along each direction in space). From the other side, one could argue that the dependency of the moisture transport coefficient on network saturation might be due to the small size of the network, since it has never been reported before (Crausse et al. [1981], Pel et al. [2002]). Therefore it seems desirable to as much as possible increase the number of nodes, so as to see how macroscopic parameters might change. However, increasing the network size of PN drying simulations to bigger than $50 \times 50 \times 51$ nodes is computationally expensive. A major reason for the high computational time of viscous-capillary PN drying simulations is that the liquid pressure field is solved in each time step (see Chapter 2 for the PN algorithm). However, we may use a physical phenomenon as a trick to reduce the computational time, that is to introduce gravity instead of viscosity in PN drying simulation. In the next section it will be explained how this trick can help to simulate bigger sample sizes.

3.5.2 Using gravity instead of viscosity for extraction of macroscopic parameters

As it was mentioned before, by increasing the network size to fairly bigger sizes ($> 100 \times 100 \times 101$ nodes), the computational time of PN drying simulation increases drastically. When dealing with such network sizes, the main time-consuming parts of the PN drying algorithm in viscous-capillary regime are the solution of liquid and vapor pressure field as well as relabeling of the liquid clusters. To make the PN simulation of bigger networks possible, one trick could be to use gravity instead of viscosity as a stabilizing force. In this way, the liquid pressure field at each time step of the PN drying algorithm is not solved, since viscosity is neglected. Therefore the time-consuming parts of the PN drying algorithm are reduced to two parts: solution of the vapor pressure field and relabeling of the liquid clusters. However, when using the gravity instead of the viscosity as stabilizing force, two points should be considered:

1. The gravity-capillary simulations are not able to produce moisture transport coefficient in the liquid phase by the method explained in Section 3.3.1. This is due to the fact that here viscosity is negligible, therefore, the Hagen-Poiseuille equation (Eq. 2.4) cannot be used to produce the liquid flux through a slice (J_ℓ) and, consequently, D_ℓ cannot be extracted from Eq. 3.15.

2. If the gravity-capillary simulations are supposed to produce macroscopic parameters which resemble the ones in viscous-capillary regime, the characteristics of the two-phase region, i.e. its size and phase distribution produced by both regimes during the drying process should not deviate a lot from each other. This is due to the fact that all macroscopic parameters are calculated in the two-phase region, i.e. where

$0 < S_{loc} < 1$. Therefore, it is necessary that the characteristics of this region for the two regimes are close to each other.

In order to quantify the second point, it is necessary to study the change in the vertical extent of the two-phase region (L_{tp}) during the drying process in both viscous-capillary and gravity-capillary regime. The change of L_{tp} during the immiscible displacement in porous media is due to the competition between capillary, gravity and viscous forces in the liquid phase (Yortsos et al. [1997]). The dimensionless number Ca (capillary number) quantifies the relative magnitude of the viscosity over capillary force, whereas Bo (Bond number) relates gravity and capillary forces as (Metzger et al. [2007b])

$$Bo = \frac{\Delta \rho g L_t r_0^2}{2\sigma_0 \gamma}, \tag{3.18}$$

in which $\Delta \rho$ is density difference $\Delta \rho = \rho_\ell - \rho_g$, r_0 is the mean throat size, σ_0 is the standard deviation of throat size and g is acceleration gravity (m/s^2). The capillary number is calculated by (Metzger et al. [2007b])

$$Ca = \frac{4\mu_\ell \dot{\vartheta} L_t^3}{A\rho_\ell \pi r_0^2 \sigma_0 \gamma}. \tag{3.19}$$

The length of the two-phase region in three-dimensional drying of porous media can therefore be expressed as a function of these two dimensionless numbers as (Laurindo and Prat [1996], Prat et al. [2012])

$$L_{tp} \sim Bo^{-1}, L_{tp} \sim Ca^{-1}. \tag{3.20}$$

Bo stays constant during the drying process (it is not a function of evaporation rate, see Eq. 3.18), while Ca decreases with time since it is directly proportional to the drying rate. Therefore, it is expected that in the gravity-capillary case except for a short period at the beginning and the period after the breakthrough (BT) point (the time when gas reaches the bottom of the network), the length of the two-phase region stays constant. On the other hand, until the BT point a continuous increase in L_{tp} for the viscous-capillary case is expected. After the BT point and with drying of the network, the length of the two-phase zone decreases.

Knowing that L_{tp} shows two different kinds of behavior during drying in viscous-capillary and gravity-capillary regimes, it should not be expected that the macroscopic parameters of these two regimes are always in agreement. Instead, it is only under certain conditions that the macroscopic parameters of the gravity-capillary regime could resemble the ones from the viscous-capillary regime. One necessary condition is that the initial values of Ca

and Bo need to be in the same range. Then at early stages of the drying process, when capillarity is the main mechanism for the transport of liquid inside the porous medium, the phase distribution in both cases would be similar.

The other important criterion for resemblance between macroscopic parameters obtained from pore network drying simulations of gravity-capillary and viscous-capillary regimes is the ratio of the height over width (H/W) and depth (H/D) of the network. As it was mentioned, the two-phase region in viscous-capillary regime will continuously widen until the BT happens, while the L_{tp} in gravity-capillary regime stays constant. Therefore, the higher the network, the more discrepant the length of the two-phase region in these two regimes will become. Consequently, the macroscopic parameters would be less similar. However, it is not clear for a given width and depth of the network, how big the height of the network should be in order to get similar macroscopic parameters in both regimes.

In order to investigate which range of H/D and H/W values would lead to similar macroscopic results in the gravity and viscous cases, gravity-capillary PN drying simulations were performed on the same network sizes ($25\times25\times51$ and $50\times50\times51$ nodes), while other geometrical and operating conditions were similar to the viscous-capillary simulations. The initial capillary number of viscous-capillary simulations in this chapter calculated by Eq. 3.19 is Ca = 0.014. For the gravity-capillary simulations, the acceleration of gravity was considered to be 1.3 m^2/s, so that to have Bo in the same range as the initial Ca (based on Eq. 3.18, Bo is equal to 0.022). The complete simulation parameters can be found in Appendix A.

In Fig. 3.23, L_{tp} for both regimes is shown. As it was expected, the length of the two-phase region in viscous-capillary regime becomes bigger than in the gravity-capillary regime. However, because the height of the network is not too big compared to its width and depth (H/W and H/D both are 2 in this case), the L_{tp} stays in the same range for both regimes. Thus it is expected that macroscopic parameters extracted from both regimes will resemble each other. Three macroscopic parameters, the NLE functions at the surface and inside the network and the moisture transport coefficient in the gas phase, obtained from PN drying simulations of gravity-capillary regime on the network with $25 \times 25 \times 51$ nodes are shown in Fig. 3.24 and are in good agreement with results for viscous-capillary regime on the same network size.

It is therefore expected that for values of H/W and H/D smaller than 2, provided the Bo and initial Ca are both in the same range, the macroscopic parameters obtained from PN drying simulations of gravity-capillary regime will be similar to the ones obtained from viscous-capillary simulations. This is due to the fact that smaller values of H/W and H/D, considering constant width and depth of the network, would result in a smaller height. However for very low values of these two ratios (shallow networks), special attention should be paid, since the BT happens quite early in this case. Also for values of H/W
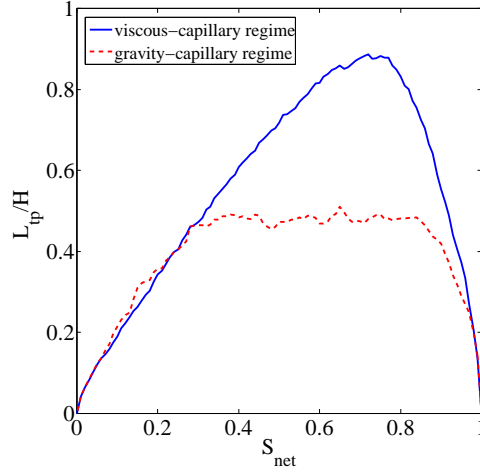
Figure 3.23: Normalized length of the two-phase zone obtained from PN drying simulations of gravity-capillary and viscous-capillary regime on the network of $25 \times 25 \times 51$ nodes, average among all realizations.

and H/D bigger than 2, it is not clear whether gravity-capillary simulations will produce the same macroscopic parameters as viscous-capillary simulations.

For the network of $50 \times 50 \times 51$ nodes, H/W and H/D are both one, therefore it is expected that the two-phase region for drying in both regimes, similarly to the network of $25 \times 25 \times 51$ nodes, will stay in the same range. Figure 3.25 shows that the discrepancy of L_{tp} values between the two regimes is not large and, therefore, suggests that macroscopic parameters for this network size should also be nearly the same. The macroscopic parameters extracted from PN drying simulations of gravity-capillary regime for the network of $50 \times 50 \times 51$ nodes are indeed in good agreement with the ones obtained from viscous-capillary regime, but here in order to avoid repetition will not be shown here. They will be documented in the electronic appendix of the thesis.

By the comparisons made above, it has been proven that it is possible to extract the macroscopic parameters of viscous-capillary drying from gravity-capillary PN drying simulations under certain conditions. This can be utilized to obtain the macroscopic parameters for bigger sample sizes, since the gravity case has lower computational cost.

To the best of our knowledge, so far the maximum network size, for which PN drying simulations in the absence of viscosity have been performed, is $80 \times 80 \times 80$ nodes by Yiotis et al. [2006] (Shibata and Hirohashi [2013], Yiotis et al. [2006]). Yiotis et al. have reported that the simulations for the capillary-dominated regime and in the absence of a diffusive layer for the mentioned network size took 18 hours on an Intel Xeon 3.6 GHz workstation. They have also mentioned that simulations on a network of $100 \times 100 \times 100$ nodes require significantly more time (several days).

A series of optimizations on the available in-house PN drying code allowed us to run the PN drying simulations for the capillary-gravity regime on the network of $100 \times 100 \times 101$ nodes, which is the biggest network ever, on which PN drying simulations have been performed. The main optimizations in the code were done on a) allocating data to sparse
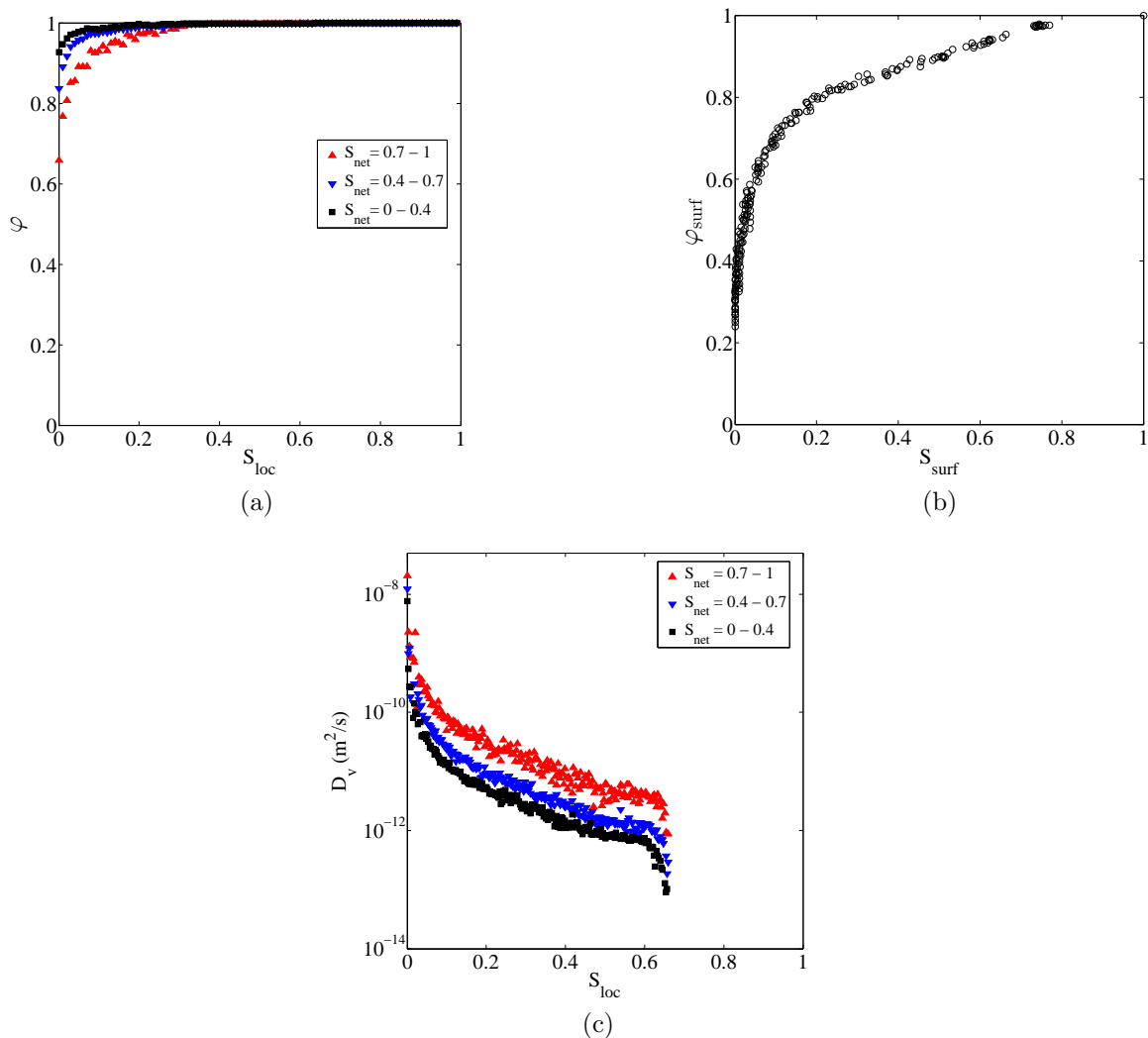
Figure 3.24: NLE function inside the network (a) and at the surface (b) and the moisture transport coefficient in the gas phase (c) obtained from PN drying simulations of capillary-gravity regime on the network of $25 \times 25 \times 51$ nodes, averaged over small local saturation intervals.

matrices and b) the non-linear solution of vapor pressure field. The final optimized PN drying code will be part of the electronic appendix of the thesis.

With the optimized code, the PN drying simulations for the capillary-gravity regime on the network of $100 \times 100 \times 101$ nodes took almost 100 days for a single run to finish, considering that this simulation was performed on a PC (not on a workstation as by Yiotis et al. [2006]). Although the computational time is very long, the results are of great value when it comes to comparing the macroscopic parameters and their change (if there is any) with network size.

The operating and geometric characteristics for the PN drying simulation on the network of $100 \times 100 \times 101$ nodes are similar to the ones considered for the simulations on the smaller network sizes discussed earlier in this chapter. The macroscopic parameters obtained from simulation of one realization on this network are shown in Figs. 3.26 and 3.27. The results show very good agreement with the ones obtained for the networks of $50 \times 50 \times 51$ and
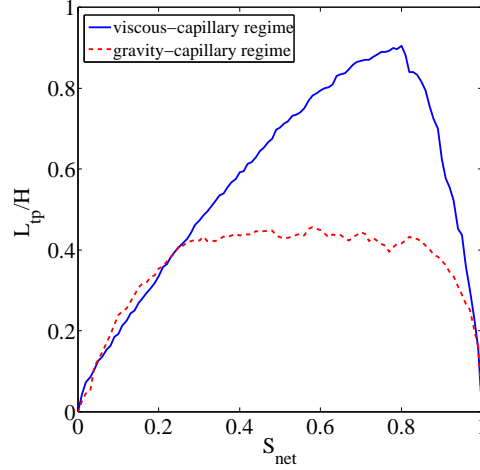
Figure 3.25: Normalized length of the two-phase zone obtained from PN drying simulations of gravity-capillary and viscous-capillary regime on the network of $50 \times 50 \times 51$ nodes, average among all realizations.

$25 \times 25 \times 51$ nodes.
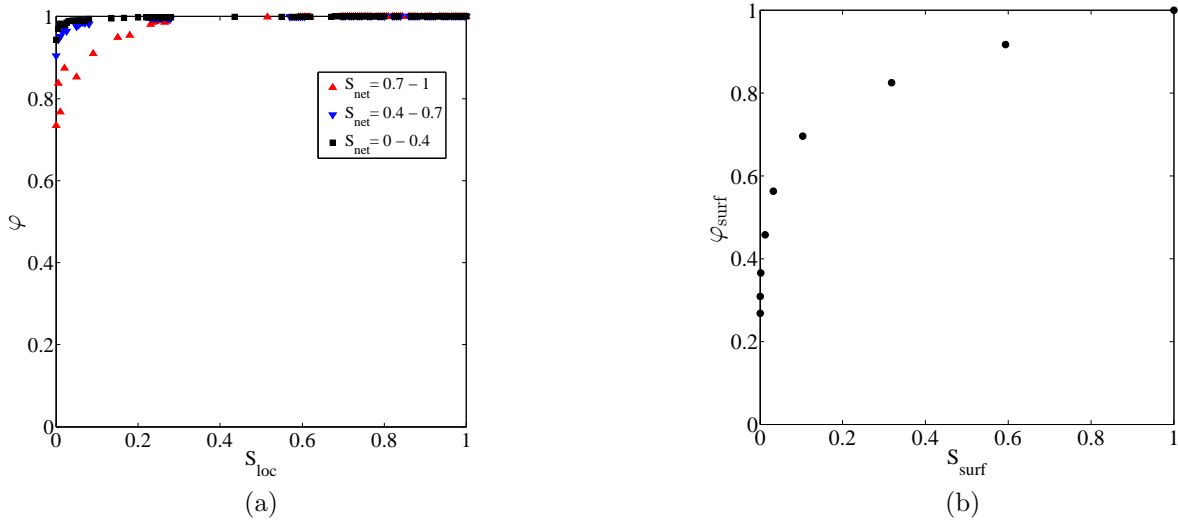
Figure 3.26: NLE function inside the network (a) and at the surface (b) for the network of $100 \times 100 \times 101$ nodes.

The moisture transport coefficient in the gas phase for the network of $100 \times 100 \times 101$ nodes, similar to smaller network sizes, is a function of network saturation and becomes zero for $S_{loc} > 0.68$ (the vapor pressure for these local saturations is p_v^*). The other point regarding the analysis of the results of the network of $100 \times 100 \times 101$ nodes, which is 32 times as big as the network of $25 \times 25 \times 51$ nodes, is that the NLE phenomenon for this big network size is observed with similar significance as for the smaller networks. This once more questions the validity of the traditional assumption of local equilibrium in the presence of water in the CM for the drying of capillary porous media.

Based on the previous comparisons made between the viscous-capillary and gravity-capillary simulations in this section, it is expected that the three macroscopic parameters for the network of $100 \times 100 \times 101$ nodes in viscous-capillary regime will be similar to the
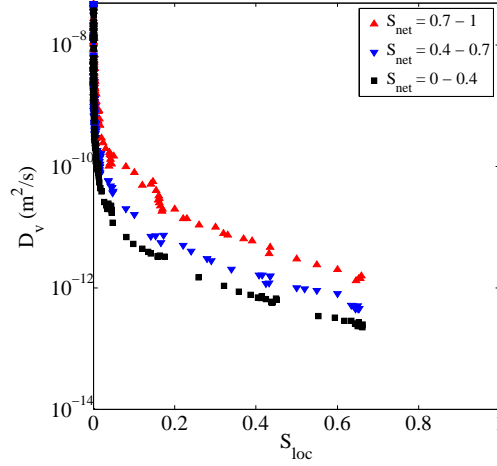
Figure 3.27: Moisture transport coefficient in the gas phase for the network of $100 \times 100 \times 101$ nodes.

ones obtained from the gravity-capillary simulations.

According to the results of all the networks considered in this chapter, the following remarks regarding macroscopic parameters in viscous-capillary drying of a capillary porous sample can be pointed out, provided that the ratios of H/W and H/D are not bigger than 2 and not too small:

1. For network sizes smaller than $100 \times 100 \times 101$ nodes, the non-local equilibrium phenomenon should always be considered. Also the fact that the internal and surface NLE functions are different should be taken into account for all network sizes.

2. For network sizes smaller than $100 \times 100 \times 101$ nodes, the moisture transport coefficient in the gas phase is always a function of network saturation. This has not been reported in any scientific publication before.

3. For any network size smaller than $100 \times 100 \times 101$ nodes, the macroscopic parameters D_v, φ and φ_{surf} can be obtained from gravity-capillary simulation of the reference network, provided that Bo is in the same range as the initial value of Ca. Therefore, the reference network of $25 \times 25 \times 51$ nodes is considered as the representative network for all network sizes smaller than $100 \times 100 \times 101$ nodes.

4. For network sizes smaller than $50 \times 50 \times 51$ nodes, D_ℓ obtained from the reference network can be used. Since the PN drying simulation on the network of $100 \times 100 \times 101$ nodes was performed only for the gravity-capillary regime, it is not clear how D_ℓ might change when increasing the network size to bigger than $50 \times 50 \times 51$ nodes. However, according to the fact that for PN drying simulations of viscous-capillary regime Ca is the same as in the smaller networks, it is expected that D_ℓ does not change with the network size.

5. The macroscopic parameters of network sizes bigger than $100 \times 100 \times 101$ nodes are likely to be similar to the ones obtained from the reference network, if the initial Ca

is the same. This is due to the fact that the phase distribution and the structure of the two-phase region (width, slice-average saturation and the ratio of isolated menisci) for bigger samples are expected not to deviate from the reference network.

The conclusions made here are valid for not too high or shallow samples. The investigation of the macroscopic parameters for very high or shallow networks as well as the ability of the one-equation continuum model to predict their saturation profiles and evaporation rate obtained from PN drying simulations is yet to be done.

3.6   Remarks

In this chapter, the results obtained from the one-equation continuum model and from pore network simulations for drying of a capillary porous medium are compared and assessed. The continuous model includes, implicitly or explicitly, three macroscopic parameters, the moisture transport coefficient and two non-local equilibrium relationships. A slice-sampling method was developed to extract these parameters from PN drying simulations. The non-local equilibrium phenomenon was observed at the medium's surface as well as inside the model capillary porous medium. This phenomenon is typically ignored in the classical continuum modeling of drying of capillary porous media. The results on the moisture transport coefficient showed three critical points of the D-S curve: two maxima at opposing local saturation limits, which show that the transport is best propelled in completely dry or wet regions, and a minimum that occured at S_{min}, which is a sign of maximum obstacle for the transport of the evaporating species. Isolated liquid menisci played a crucial role in the D-S curve. The moisture transport coefficient was also obtained from capillary-controlled invasion percolation simulations. In this method results were obtained until the irreducible saturation, since at local saturations lower than that the conductivity of the liquid phase was lost and therefore capillary-controlled IP could not be used. As the third method of extraction of D, an inverse method based on the spatial integration of the one-equation CM was developed. The results on the moisture transport coefficient obtained from the PN drying simulations and capillary-controlled IP were in agreement, except at very high saturations. This is due to decreased liquid flux in PN drying simulations as a result of fluctuations of liquid pressure field. The inverse method overestimated the values of D at low network saturations. This is due to the fact that isolated menisci are not distinguished in this method. The evaporation rate was well reproduced by the CM using the surface non-local equilibrium relationship φ_{surf} obtained from PN drying simulations until $S_{net} \approx 0.85$. This network saturation corresponds to the lowest surface saturation, at which φ_{surf} values are obtained by PN drying simulations. From this network saturation on, the evaporation rate of PN drying simulations was used directly as boundary condition in the CM. By the help of evaporation rate of PN drying

simulations, a method was developed to predict D as a function of saturation at very low local saturations. It was shown that the CM is able to reproduce the saturation profiles of PN drying simulations.

It was also proved that PN drying simulations of gravity-capillary regime are able to produce the macroscopic parameters (except D_ℓ) similarly to the viscous-capillary regime, on two conditions: a) the network should not be too high or too short, and b) Bo should be in the same range of initial Ca in viscous-capillary simulations. It has also been shown that with increasing the network size to $100 \times 100 \times 101$ nodes, D_v, φ and φ_{surf} do not change.

The main conclusion, however, is that interpreting the relationship between vapor partial pressure and saturation classically, introduced in the development of the one-equation model as a desorption isotherm, is wrong, at least for our model porous medium. This is the signature of a non-local equilibrium effect. As a result, developing a NLE two-equation model is the logical next step to improve the continuum modeling of drying.

Because of the importance of the NLE function at the surface on the evaporation rate of the one-equation CM, in the next chapter, this function will be studied in more detail.

Chapter 4

Surface phenomena during drying of porous media

4.1 Introduction

This section is partly taken from Attari Moghaddam et al. [2017c].

When the gas invades into the porous medium capillarity, gravity and viscosity define the drying kinetics (Prat [2002]). Obviously, the closer the liquid to the evaporative surface, the higher is the evaporation rate. In a capillary porous medium, as sketched in Fig. 3.1, viscosity and gravity act as a barrier to the liquid pumping towards the evaporative surface and this consequently leads to a decrease in evaporation rate.

As reported, for example, in Van Brakel [1980] or Coussot [2000], the drying kinetics of a capillary porous medium can be described in three main periods: namely a first period, the constant rate period (CRP), during which the evaporation rate is constant (or varies only weakly); a second period called the falling rate period (FRP), during which the evaporation rate drops significantly; and a third period called the receding front period (RFP), where evaporation takes place inside the porous medium and not anymore at its surface. In soil physics, e.g. Lehmann et al. [2008], Shokri and Or [2011], this description is simplified with the distinction of only two periods: stage 1 and stage 2, with stage 1 corresponding to the CRP and stage 2 to the combination of the FRP and the RFP.

This simplification emphasizes the fact that a crucial aspect of the drying process is the transition between the CRP and the FRP (or stage 1 / stage 2 transition). From an engineering prospect for instance, maintaining a long CRP can be a desirable objective to minimize the drying time. The understanding and the prediction of this transition can be considered as one of the remaining fundamental questions of drying of capillary porous media. The classical (qualitative) description of the transition, e.g. Van Brakel [1980] and Coussot [2000], Krischer [2013], essentially takes a porous medium standpoint. Schematically, the CRP/FRP transition occurs when the capillary forces are not suffi-

cient anymore to transport to the surface the liquid flow rate needed to compensate the evaporation rate corresponding to the CRP. In the viscous-capillary regime, this is owing to the increasing viscous resistance in the liquid due to the progressive decrease of liquid saturation, and in the gravity-capillary regime it is due to the sharp drop in capillary potential with decreasing distance from the bottom of the network. This is thus essentially a "liquid relative permeability approach" of the transition, e.g. Coussot [2000], since the liquid phase relative permeability decreases with decreasing saturation. However, one can also look at this transition from the external mass transfer standpoint. Obviously, the external mass transfer does not "know" what happens inside the porous medium. It only "sees" the surface. Thus, if the evaporation rate decreases, this is because the distribution of liquid water at the surface changes, or more precisely the water vapor partial pressure distribution at the entrance of the surface pores. The external mass transfer standpoint analysis was first developed by Suzuki and Maeda [1968] and then by Schlünder [1988], noting that Schlünder's model has been analyzed and used recently in a series of papers by e.g. Haghighi et al. [2013], Lehmann and Or [2013] and references therein. The porous medium surface implicitly considered by Schlünder is a spatially periodic surface. Each unit cell is a parallelepipedic volume in which the mass transfer is governed by diffusion. The bottom surface contains a cylindrical pore entrance where the vapor partial pressure is known (assuming the pore occupied by liquid, the saturation vapor pressure is assumed over the pore opening). A zero flux condition is imposed on the solid surface (surface complementary to the pore opening surface). Spatial boundary conditions are imposed on the lateral sides of the unit cell.

It is clear, however, that the surface of a drying porous medium is less simple than considered in Schlünder's model. In addition to liquid pores and solid surface, there are also empty pores (i.e. gas pores). The vapor partial pressure at the entrance of those pores is a priori less than the equilibrium vapor pressure prevailing at the entrance of liquid pores and not equivalent to a solid surface (where a zero flux condition applies). Also the liquid distribution changes during drying with the formation of dry and wet patches of evolving size. This suggests that Schlünder's model is probably not sufficient for modeling the impact of changes occurring at the porous surface on evaporation rate.

To get new insights into this problem, we use a pore network approach. The main advantage of the pore network approach in the context of this chapter is to permit to consider explicitly a discrete representation of the porous surface together with several additional important ingredients such as a spatial variation in the pore radius and the coupling with the phenomena occurring inside the porous medium. As described in review papers, e.g. Metzger et al. [2007b], Prat [2002, 2011], a pore network model of drying can be more or less sophisticated depending on the phenomena taken into account. Here, the idea is to consider the simplest situation corresponding to the slow drying at room temperature of a relatively thin sample, a situation frequently encountered in laboratory experiments.

Slow drying implies that the temperature variations induced by the evaporation process are negligible.

The pore network will provide us a detailed description of the phenomena happening at the surface and will also show how the continuum formulation of the evaporation rate used in the one-equation continuum model of drying can be affected by them. To this end, the pore network and continuum drying rates are introduced in the next section.

4.2 Evaporation rate in pore network and continuum models

The vapor pressure of pores at the evaporative surface has a direct impact on the drying rate of porous media. As far as the modeling of drying processes is concerned, the drying rate could be calculated in different ways. As it was explained in Chapter 2, during PN drying simulations, at each time step the vapor pressure field is solved for all gas pores inside the porous sample and the computational nodes in the diffusive layer. By knowing the vapor pressure field, the evaporation rate in PN drying model is calculated by summing up the vapor diffusion flow (Eq. 2.3) between the computational nodes at the top of the boundary layer. In fact, in the PN drying model, the vapor at each surface pore is transported to the atmosphere via a discretized boundary layer. However, in a continuum drying model a mean vapor pressure at the surface is considered first, and then by using the diffusion law between surface and top of the boundary layer the drying rate is obtained. The evaporation rate in this case, is

$$\dot{\vartheta} = \frac{\tilde{M}_v A}{\tilde{R}T} D_{va} \Big(\frac{p_{v,surf} - p_{v,\infty}}{\delta} \Big). \tag{4.1}$$

In Chapter 3, it was shown that the internal NLE function is different from the NLE function at the surface. The usage of a NLE function at the surface was shown to produce reliable drying kinetics results. Therefore the NLE function at the surface can be written as

$$\varphi_{surf} = \frac{p_{v,surf}}{p_v^*}, \tag{4.2}$$

in which φ_{surf} is a function of the surface saturation ($\varphi_{surf} = f(S_{surf})$). Replacing Eq. 4.2 into 4.1 the evaporation rate of the one-equation CM is

$$\dot{\vartheta} = \frac{\tilde{M}_v A p_v^*}{\tilde{R}T} D_{va} \Big(\frac{\varphi_{surf} - \varphi_{\infty}}{\delta} \Big). \tag{4.3}$$

Equation 4.3 states that the evaporation rate in the CM depends only on one parameter:

φ_{surf}. In Chapter 3 it was mentioned that the CM assumes there are homogenized volumes (averaging volumes) inside the porous sample, on which the continuum equations are solved. Here at the surface the same concept is applied, i.e. the evaporative surface is treated as homogeneous, whereas the fluctuations of vapor pressure at the surface are considered through an average quantity (NLE function at the surface).

In order to obtain the relationship between φ_{surf} and surface saturation, an averaging domain should be defined first. This is shown in Fig. 4.1, in which all throats in the first row and half of the second top vertical throats of the pore network contribute to surface saturation. Later in this chapter, it is shown that a high evaporation rate could occur because of two reasons: a highly wet surface or significant presence of water just below the surface. Therefore it is logical to consider a contribution of throats in both the first and the second top row of the pore network in the NLE function at the surface.

The mean vapor pressure of the surface pores is calculated and then divided by the saturation vapor pressure to give the NLE function at the surface. By knowing the relationship between φ_{surf} and surface saturation, Eq. 4.3 is used to predict the evaporation rate in the one-equation CM.
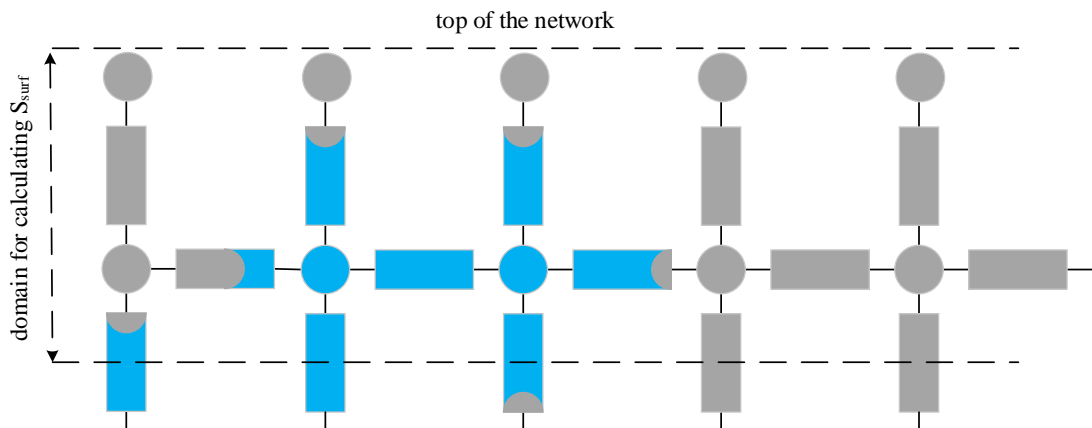
Figure 4.1: Schematic representation of a slice in 2D for calculation of surface saturation.

In this chapter, by using pore network simulations, the phenomena that happen at the surface of a porous medium during drying are investigated and their effect on the NLE function at the surface is analyzed. The role of wet and dry patches on the mean vapor pressure of the surface and consequently on the total evaporation rate for different regimes and geometrical and operating characteristics are also studied. The change in two-phase region length when the surface is partially wet is analyzed and its role in the NLE function is investigated. In order to do so, pore network drying simulations are performed on the network of $25 \times 25 \times 51$ nodes. The PN drying algorithm is described in Chapter 2.

4.3 Influence of stabilizing effect on the evaporation rate

In a drying porous medium and in the absence of viscosity and gravity, when the gas invades inside the bulk of the liquid, the water can be pumped towards the evaporative surface without any resistance. Therefore it is expected to have a longer CRP in capillary-dominated regime. However, in presence of viscosity or gravity, the water cannot be transported to the surface as easily as in the capillary-dominated regime. This is due to the stabilizing effect of viscosity and gravity and would lead to a shorter CRP compared to the capillary-dominated regime.

In order to investigate the effect of stabilization on the phase distribution of the surface of the drying porous medium, three different series of simulations are considered. Because of the lower computational cost for simulations in the absence of viscosity, only capillary-dominated and gravity-capillary regimes are considered. However, as it was shown in Chapter 3, the results for the gravity-capillary regime can be generalized for viscous-capillary drying.

Case 1 is a capillary-dominated drying process in which the phase distribution during drying is essentially controlled by the capillary forces. This regime is typically observed in samples sufficiently thin for the pressure drop in the liquid phase due to gravity or viscous effects to be negligible compared to the pressure variations due to the capillary effects (Prat [1993]). Cases 2 and 3 have Bo equal to 0.022 (g = 1.3 m/s^2) and 0.22 (g = 13 m/s^2), respectively. Therefore Case 3 has the biggest effect of gravity on the transport of water. The main characteristics of the simulations are shown in Table 3.1 (except for viscosity, since here the viscosity is neglected). For each series of PN drying simulations, 15 different realizations of throat size distribution are considered. The complete simulation parameters can be found in Appendix A.

The normalized evaporation rate curves of the three cases are shown in Fig. 4.2. In the capillary-dominated regime, a longer constant rate period is observed, which is due to the existence of water at the surface for a longer period compared to the other cases. With increasing Bo, the water detaches earlier from the evaporative surface, leading to smaller evaporation rate at the same network saturation.

The presence of water at the evaporative surface leads to bigger vapor pressure in the pores at the top of the network. This will consequently lead to an increased rate of evaporation. Therefore the area of the evaporative surface which is covered by liquid water plays an important role in the total drying rate of the porous sample. The normalized wet surface area is obtained as
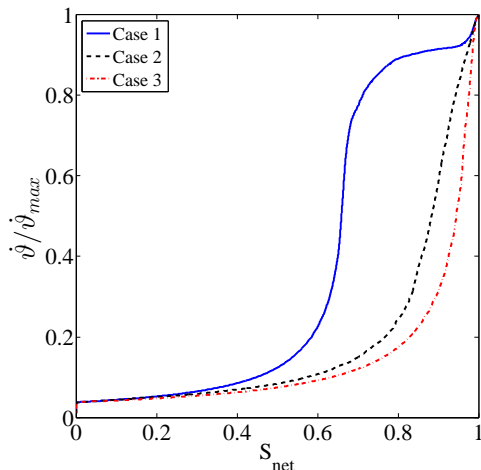
Figure 4.2: Normalized evaporation rate versus network saturation for three different series of PN simulations, each of which is averaged among 15 realizations.

$$A_w = \frac{\sum\limits_{i=1}^{n} \pi r_i^2}{\sum\limits_{i=1}^{N_x N_y} \pi r_i^2}, \tag{4.4}$$

where n is the number of vertical channels (throats) occupied by liquid at the top surface of network and $N_x N_y$ is the total number of vertical channels at the network top surface (see Fig. 2.1). Thus, A_w changes from one (fully wet surface, meaning that all surface throats are occupied by liquid) to zero (fully dry surface).

As it was mentioned before, for different regimes the water remains at the evaporative surface for a different period. In Fig. 4.3 the change of network saturation during a period in which the normalized wet surface area (A_w) changes from one to zero is shown. The surface in the capillary-dominated regime becomes completely dry at much lower network saturation (around 0.67) compared to the case with the highest Bo (around 0.95). This means that for the capillary-dominated regime water stays at the top of the network longer than in the other cases, which will consequently result in a longer CRP.

The extent of the period during which water remains at the surface of the porous sample depends on the competition of the capillary and gravity forces which affects the pumping of the liquid inside the network. This competition can be analyzed by changes of two-phase region length. Figure 4.4 shows the change in normalized length of the two-phase region versus normalized wet surface area. For better understanding of the effect of gravity on water pumping towards the surface, take for example two extreme cases: the capillary-dominated regime and the case with the highest Bo (Case 3). High gravity force in the latter makes it harder for the gas to invade deeper into the network, since the capillary potential is lower at those positions. This will lead to a slower increase in L_{tp}/H at relatively high A_w. Instead, for capillary-dominated regime, there is no resistance in

58
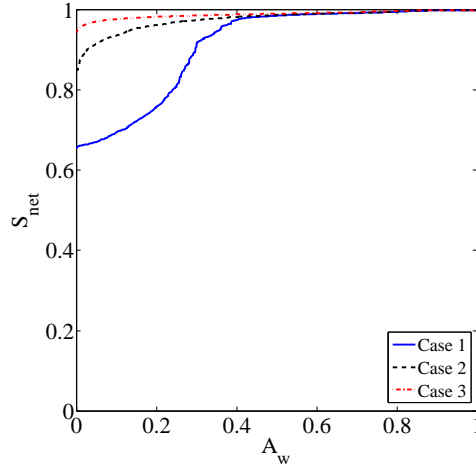
Figure 4.3: The change of network saturation until the surface becomes completely dry for three different cases, each of which is averaged among 15 realizations.

pumping the liquid inside the network and therefore gas can easily invade into deeper positions of the sample, leading to a steeper increase in L_{tp}/H and creation of more menisci for $A_w > 0.4$. In this case, as soon as there are enough menisci created inside the sample, knowing that at each time step the biggest meniscus is emptied, the possibility of surface menisci to be emptied becomes very small. This happens at A_w around 0.4 and that is why there is a sharp increase in the L_{tp}/H curve in this range of A_w. The evaporation at surface menisci will be compensated by the pumping of the water from the liquid inside the network, so the surface will stay partially wet for a longer period. In contrast, in the case with the highest Bo, the pumping of the water is resisted by the strong gravity force and therefore the surface cannot be prevented from drying out for a long period (Fig. 4.3). Thus a larger L_{tp}/H at $A_w > 0$ will lead to a longer presence of water at the surface and, consequently, to a bigger evaporation rate.
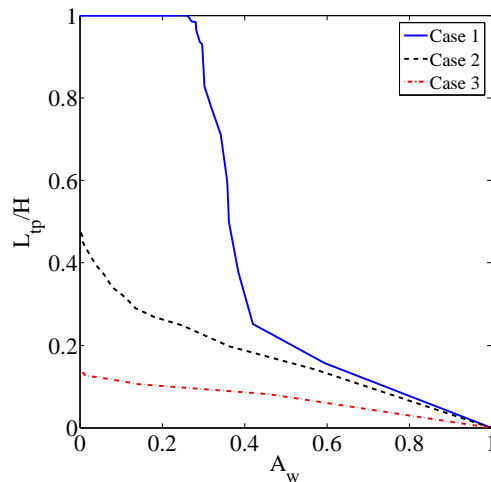
Figure 4.4: The change of the normalized two-phase region length versus normalized wet surface area for three different series of PN simulations, each of which is averaged among 15 realizations.

Pores at the surface which are neighboring to dried throats will not be in direct contact with water anymore and therefore their vapor pressure becomes smaller than saturation

vapor pressure. As the drying goes on, there will be a point at which, over a bigger area of the surface, pores will not be in equilibrium with the liquid, which will consequently affect the total evaporation rate of the sample. This effect at high A_w or for strongly stabilized regimes with small throat length will not be significant though, since the vapor pressure of the non-equilibrium pores will be close to the saturation vapor pressure (the effect of throat length on the vapor pressure will be explained later in this chapter). This is due to the massive presence of water near the top of the network.

Surface pores in these non-equilibrium areas could have different vapor pressures, depending on the liquid transport regime. As it was shown in Fig. 4.4, in the capillary-dominated regime the two-phase region can expand over the whole depth of the network, while the surface is still partially wet. This means that one would expect to have smaller vapor pressure in dry regions of the surface, since the water below the surface and inside the network is less. Therefore the change of vapor pressure of surface pores will be bigger compared to Cases 2 and 3.

Figure 4.5 shows the normalized standard deviation of vapor pressure at the surface ($\sigma_{p_{vs}}/p_v^*$) versus normalized wet surface area. As the drying goes on, because of creation of more non-equilibrium regions, the standard deviation of the vapor pressure increases constantly until it reaches a maximum. At this point, a small part of the surface is wet while the rest is dry and pores have different vapor pressures. After this point, the wet area dries out, which leads surface pores to have more uniform vapor pressure. It is also seen that the maximum of standard deviation for the case with the highest Bond number (Case 3) is slightly smaller. But in general, $\sigma_{p_{vs}}$ values for all cases are close to each other. This might be due to the small height of the network or a big boundary layer thickness. In fact, in all cases during the period in which the surface is partially wet, the presence of water inside the network is "felt" strongly in the gas pores neighboring to the empty throats at the surface. It is however expected that by changing the height of the network or boundary layer thickness, $\sigma_{p_{vs}}$ would differ more significantly among the three cases.

The analysis of the surface also helps to understand the behavior of φ_{surf} and consequently the evaporation rate of CM. In Fig. 4.6, the NLE function is plotted against surface saturation. According to Eq. 4.3, this figure also shows the normalized drying rates of the continuum model, because evaporation rate is directly proportional to φ_{surf}. It is then seen that, although the liquid transport regimes in Cases 1 to 3 are different, their φ_{surf} values are in general close to each other. In other words, the NLE function at the surface is not affected by the liquid transport mechanism in the range of gravity-capillary regime and thus the effect of the acceleration of gravity on the NLE function at the surface is not significant. The non-significant effect of the gravity on φ_{surf} can also be explained by the standard deviation of vapor pressure at the surface. As it was shown in Fig. 4.5, the fluctuations of vapor pressure at the surface pores are close in all three cases and therefore it is expected that their NLE functions do not deviate very much from each other.
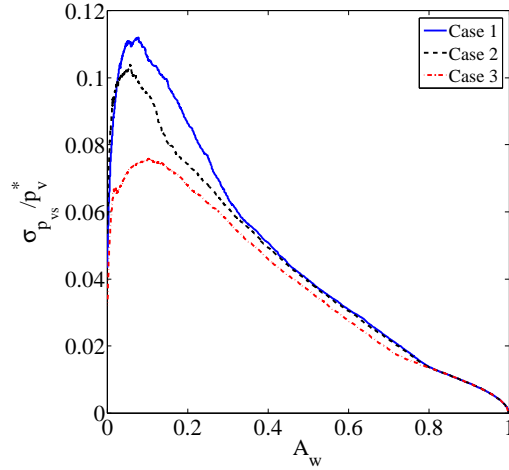
Figure 4.5: Normalized standard deviation of vapor pressure at the surface versus normalized wet surface area for three different series of PN simulations, each of which is averaged among 15 realizations.
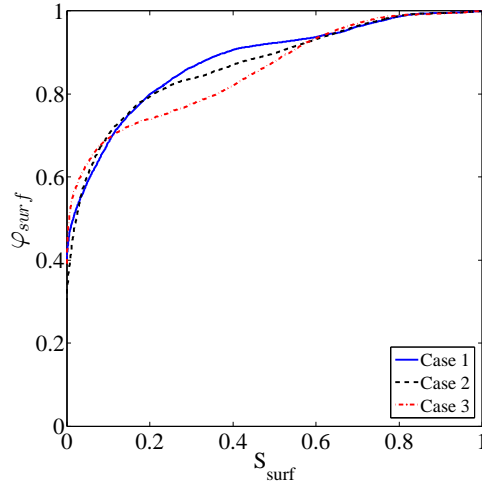
Figure 4.6: NLE function at the surface versus surface saturation for three different cases of PN simulations, each of which is averaged among 15 realizations.

Since throats are randomly distributed in the network, the creation of non-equilibrium areas leads to forming discrete wet areas on the surface. These wet patches have different size and are randomly distributed on the surface. In Figs. 4.7 and 4.8, the normalized standard deviation (σ_{wp}/A_t) and the mean value of the surface area of wet patches $(\overline{A}_{wp})$ are shown for different cases. At the beginning of the drying process there is only one wet patch. As soon as the second wet patch has been produced, σ_{wp} will become nonzero and the decrease in $\overline{A}_{wp}$ will deviate from the linear curve. The creation of the second patch happens at lower A_w for higher Bo, since gravity leads to a more stabilized receding of the drying front into the network. As the drying process goes on, wet patches with different sizes are created, which leads to a maximum in the σ_{wp} curve. This shows that more non-equilibrium areas at the surface are produced and therefore is a reason for reduction in evaporation rate. After this point, with drying of all wet patches, their surface area is decreased and therefore the standard deviation of surface area of wet patches will constantly decrease. At lower wet surface area, the wet patches will have more uniform

and smaller size.
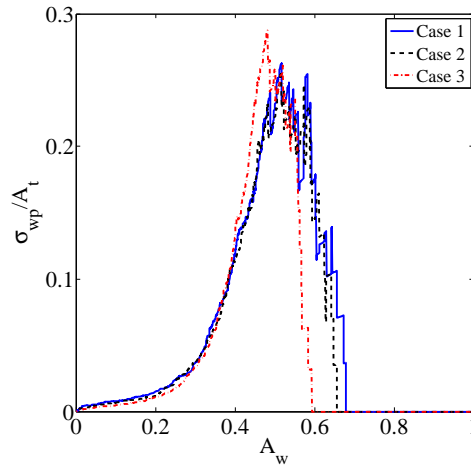
Figure 4.7: The normalized standard deviation of surface area of wet patches versus normalized wet surface area for three cases, each of which is averaged among 15 realizations.
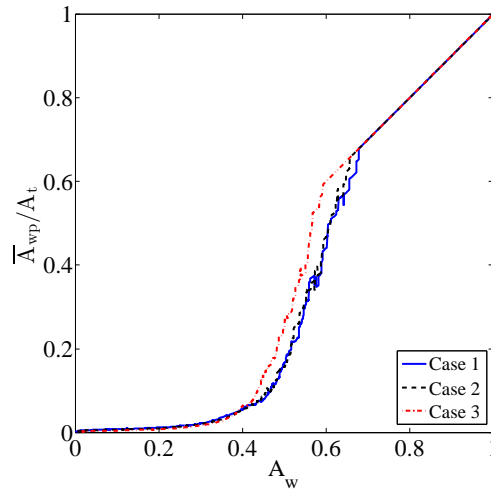
Figure 4.8: The normalized mean surface area of wet patches versus normalized wet surface area for three cases, each of which is averaged among 15 realizations.

Contrary to the simplified surface considered by Schlünder [1988], three phases, namely liquid, gas, and solid, can coexist at the surface of a drying porous medium and not simply two. It is therefore interesting to characterize the relative contributions of dry and wet surface areas to the total evaporation rate. The contribution of solid surface is obviously zero. The evaporation rate can thus be actually decomposed into two components

$$\dot{\vartheta} = \dot{\vartheta}_{wet} + \dot{\vartheta}_{dry}. \tag{4.5}$$

The contribution of wet and dry patches to the total drying rate is shown in Fig. 4.9. The transition between the dominant contributing areas to the total evaporation rate happens at a normalized wet surface area equal to 0.3. In the wet region the evaporation flux is bigger, since surface pores have saturation vapor pressure and therefore the dry region

needs a larger area to equalize the evaporation rate of the wet region. This is why the transition is expected to happen at A_w smaller than 0.5. It is also seen that in all the regimes considered in this study, the normalized evaporation rates of dry and wet regions are the same at different values of wet surface area. This shows that at each A_w the phase distribution close to the surface can be considered to be the same for all investigated regimes.
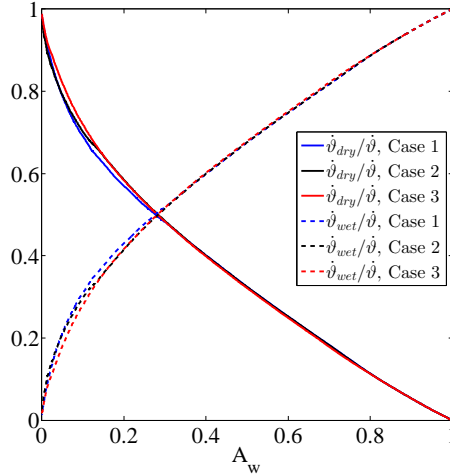
Figure 4.9: The ratio of contributions of dry and wet regions at the surface to the total evaporation rate versus normalized wet surface area for three different cases, each of which is averaged among 15 realizations.

4.4 Effect of throat length on the evaporation rate

In order to investigate the effect of network geometry on the surface phenomena, the throat lengths are changed. In all simulations capillarity is responsible for the transport of liquid. Case 1 is compared to two new cases, Case 4 and Case 5. The throat length in Case 4 is 2.5 times smaller than in Case 1, while in Case 5 the throat length is bigger by 2.5 times. For each set of simulations 15 realizations are considered, while the geometrical and operating characteristics remain unchanged. The complete simulation parameters can be found in Appendix A.

Since the variation of throat length will lead to a change in the cross sectional area of the evaporative surface, the initial evaporation rates of the three cases will be different. In Fig. 4.10 the evaporation rates of all three cases are normalized over their respective initial evaporation rate, to be able to study their relative behavior observed at the surface during drying of the network. In Case 5, longer throats lead to a bigger drop in evaporation rate at the beginning of the drying process, while for Case 4 with the shortest throat length a small drop is observed. This can be investigated by looking at the NLE function curves in Fig. 4.11, in which a large slope in φ_{surf} versus saturation of the surface curve suggests that the change of evaporation rate during the period in which $S_{surf} > 0$ should be big.
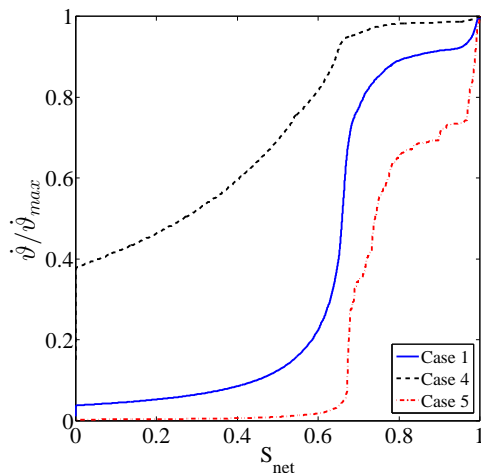
Figure 4.10: Normalized evaporation rate versus network saturation for three different throat lengths in PN simulations of capillary-dominated regime, each of which is averaged among 15 realizations and normalized over its initial value.
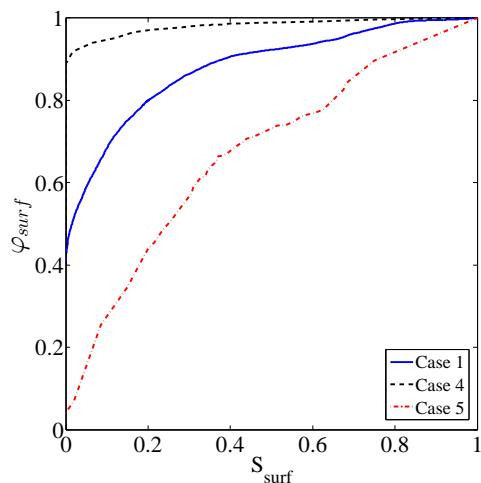
Figure 4.11: NLE function at the network surface versus surface saturation for three different throat lengths in PN simulations of capillary-dominated regime, each of which is averaged among 15 realizations.

In fact change of throat length leads to another change in the geometrical characteristics of the network and that is the change of the cross sectional area of the network. The cross sectional areas in Cases 1, 4 and 5 are 25 mm×25 mm, 10 mm×10 mm and 62.5 mm×62.5 mm, respectively. In order to understand the effect of these two changes on the evaporation rate and φ_{surf}, each change is compared with a base case.

First it is considered that only the throat length changes compared to the base case, whereas the cross section of the sample remains unchanged. At the beginning of the drying process, when surface menisci are saturated, surface pores are at saturation vapor pressure. Therefore the evaporation rate will be the same as in the base case. When a surface meniscus is emptied, the vapor pressure of the surface pore for that emptied throat will be reduced according to the throat length, because the pore is not anymore in direct contact with water. This will lead to a decrease in evaporation rate as well. With increasing throat length, the reduction in vapor pressure of the surface pore will be bigger,

because the vapor needs to take a longer path to get to the surface. This argument can be supported by looking at Eq. 2.3. According to this equation $\Delta p_v \propto L_t$, therefore by increasing the length of the throat, the pressure of the gas pore at the surface decreases. Consequently, the evaporation rate will experience a larger reduction. In this way the effect of increasing the throat length is a decrease in both, φ_{surf} and evaporation rate.

In order to investigate the second effect, change of cross section of the network due to varying throat length, it is assumed that inside the network the length of the throats remains constant, while the cross section of the sample changes. When vapor comes out of the network it is transported towards the top of the boundary layer while spreading over the surface. If the cross section of the sample increases, the vapor will be less accumulated just above the surface and will have more space to escape away from the surface pores compared to the base case (throat radii are kept constant). This will consequently lead to a lower vapor pressure at the surface and higher evaporation rate.

Considering the effects of change of throat length on the mean vapor pressure of surface, it is concluded that by increasing throat length, mean vapor pressure and consequently φ_{surf} is decreased. Regarding the evaporation rate, because each of the effects of change of throat length has an opposite impact on the evaporation rate, it is necessary to use the evaporation rate equation, Eq. 4.3, for interpretation. In this equation two variables are affected by the change of throat length, one is A, the cross sectional area of the evaporative surface and the other is $p_{v,surf}$, the mean vapor pressure of the surface. N_x and N_y pores are used in width and depth of the pore network, respectively, therefore A will be equal to $N_x N_y L_t^2$. Thus the effect of throat length is powered by two, which shows that throat length has a much bigger effect on the total evaporation rate compared to the reduction in $p_{v,surf}$. As a result, it is expected that by increasing the throat length, the evaporation rate will also increase.

This can be confirmed by looking at the evaporation rate curves, normalized by the initial evaporation rate of Case 1, in Fig. 4.12. In Case 1, in which the throat length is 2.5 times bigger than in Case 4, the initial evaporation rate is 2.5^2 times bigger than in Case 4 (because A and $\dot{\vartheta} \propto L_t^2$) and, similarly, Case 5 has an initial evaporation rate 2.5^2 times bigger than Case 1, since the throat lengths are also 2.5 times bigger. It is observed in this figure that when the network saturation decreases until the surface dries out (S_{net} around 0.65 for all cases), the ratio of evaporation rates between different cases stays almost constant and evaporation rate is always bigger for bigger L_t. This shows that when throat length increases, the effect of increase of cross section on the evaporation rate predominates the reduction of mean vapor pressure of the surface and keeps the evaporation rate bigger during the whole period in which $S_{surf} > 0$.

The mechanism for the transport of water in Cases 1, 4 and 5 is capillary force. Thus the sequence of emptying of menisci is the same for all of them and their phase distributions
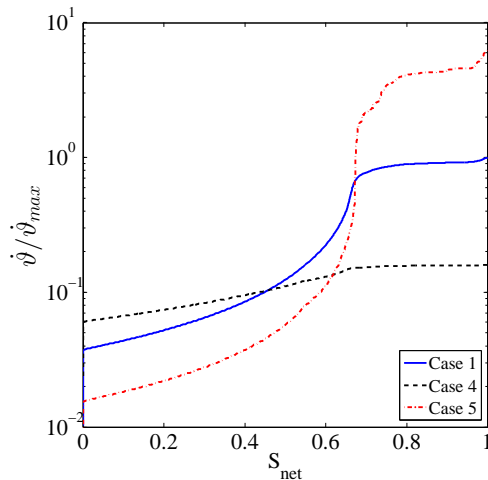
Figure 4.12: Normalized evaporation rate versus network saturation for three different throat lengths in PN simulations of capillary-dominated regime, each of which is averaged among 15 realizations and normalized over the initial evaporation rate of Case 1.

will be identical. Therefore it is expected that during the drying process they will have similar two-phase region length. Also the change of network saturation versus A_w for all cases is equivalent and the surface dries out at the same network saturation.

In Fig. 4.13 the change of normalized standard deviation of vapor pressure at the surface versus A_w is shown. As it was expected, Case 5 has much bigger $\sigma_{p_{vs}}$, since in this case the drop in the vapor pressure of a surface pore after emptying its neighboring throat is more significant. The moderate change of $\sigma_{p_{vs}}$ for Case 4 and its big deviation from the other two cases suggest that the vapor pressure of gas pores neighboring to empty throats at the surface is close to the saturation vapor pressure. With this explanation, an interesting conclusion regarding the relationship between standard deviation of vapor pressure of surface pores and NLE function at the surface (or evaporation rate) can be drawn: if $\sigma_{p_{vs}}$ is small, φ_{surf} will be bigger (as it was observed for Case 4 in Fig. 4.11). In contrary, if $\sigma_{p_{vs}}$ changes rapidly with A_w, this shows that the vapor pressure of gas pores neighboring to empty throats at the surface deviates more from saturation vapor pressure. That is the reason why the NLE function at the surface drops rapidly in this case.

In Case 5, the big drop in vapor pressure of surface pores after the menisci below them have been emptied leads to less contribution of the dry region to the total evaporation rate. Therefore it is expected that in this case the evaporation rate of the dry region becomes dominant only at very low A_w. This can be seen in Fig. 4.14. The normalized evaporation rate curves of wet and dry regions intersect at $A_w \approx 0.05$ for Case 5. But as throat length decreases, the drop in vapor pressure of pores in the dry region is smaller and therefore they contribute more to the total evaporation rate. The value of A_w at which $\dot{\vartheta}$ curves of dry and wet regions intersect will consequently move closer to 0.5. In an extreme case, when throat length would be close to zero, the contributions of wet and
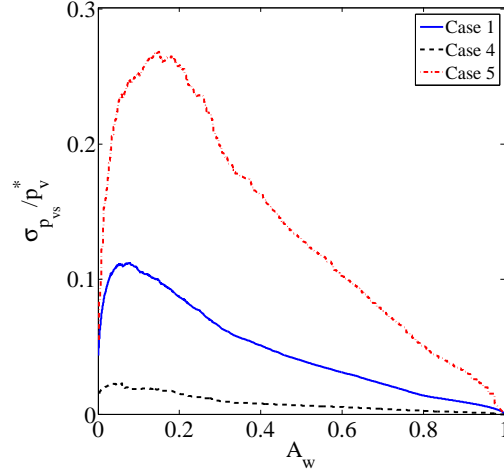
Figure 4.13: Normalized standard deviation of vapor pressure at the surface versus normalized wet surface area for three different throat lengths in PN simulations of capillary-dominated regime, each of which is averaged among 15 realizations.

dry regions to the total evaporation rate would be equal and the corresponding curves would intersect at exactly $A_w = 0.5$.
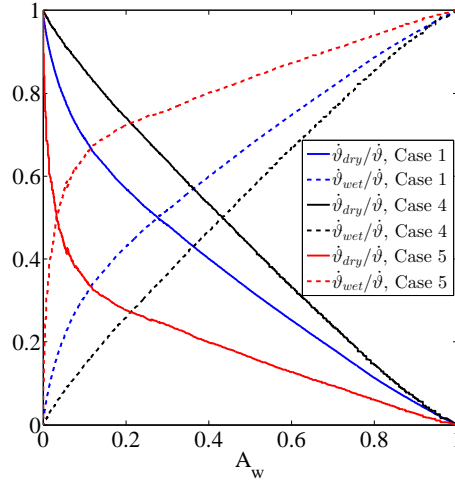
Figure 4.14: Relative contributions of dry and wet regions at the surface to the total evaporation rate versus normalized wet surface area for three different throat lengths in PN simulations of capillary-dominated regime, each of which is averaged among 15 realizations.

As it was shown in this section, the change in the geometrical characteristics of the network can significantly affect the NLE function at the surface and, consequently, the evaporation rate. This has been studied by changing the throat length and it was shown that change in throat length not only can affect the total evaporation rate of the drying process, but also affects the contribution of the dry and wet regions at the surface to total evaporation rate.

Now that it was shown that φ_{surf} is not a unique function and can change according to the geometrical characteristics of the sample, it is also interesting to study the effect of operating conditions on it. This will be done in the next section through the variation of boundary layer thickness.

67

4.5 Effect of boundary layer thickness on the evaporation rate

In order to study how the external conditions affect the surface phenomena during drying of porous media, the boundary layer thickness (δ) in capillary-dominated regime is increased. This change has not been directly applied in the simulations though, since increasing the boundary layer thickness would cost more computational time (due to increased number of computational nodes in the boundary layer). Instead the vapor diffusivity at the top row of vertical control volumes in the boundary layer is decreased, which, due to the increased resistance in vapor transport to ambient air, can be interpreted as if the boundary layer thickness had increased. In this part Case 1 from the previous section is compared with two new cases, Cases 6 and 7, in which the vapor diffusivity at the top of the boundary layer is 10 and 50 times smaller than in Case 1, respectively. The equivalent increase in the boundary layer thickness for Cases 6 and 7 can be calculated as follows: The resistance to the vapor diffusion in the boundary layer in Case 1 is $10L_t/D_{va}$ (boundary layer is composed of 10 nodes) and the resistance in Cases 6 and 7 will change to $9L_t/D_{va} + 10L_t/D_{va}$ and $9L_t/D_{va} + 50L_t/D_{va}$, respectively. In fact, only the last row of vertical control volumes in the boundary layer are affected in Cases 6 and 7 and the rest ($9L_t/D_{va}$) are unaffected. By comparing the resistances, the equivalent boundary layer thickness in Cases 6 and 7 is 1.9 and 5.9 times bigger than in Case 1, respectively. Except for the aforementioned difference between these cases, all other operating and geometrical characteristics are the same and they are done over 15 realizations. The complete simulation parameters can be found in Appendix A.

According to Eq. 4.3, $\dot{\vartheta} \propto \delta^{-1}$, therefore by increasing the boundary layer thickness, the evaporation rate decreases. This is shown in Fig. 4.15 for the cases considered in this section. The initial evaporation rate in Case 1 is 1.9 times bigger than the one in Case 6, and 5.9 times bigger than the one in Case 7.

When a surface meniscus is emptied, the change of vapor pressure of its neighboring surface pore will be dependent on the boundary layer thickness. With increasing δ, this change will be smaller owing to a higher distance of surface pores to the ambient. Therefore, when the boundary layer is thicker, the vapor pressure drop of a surface pore due to emptying of its neighboring meniscus will be smaller. This is shown via the φ_{surf} vs. S_{surf} curves in Fig. 4.16. It is observed in this figure that for Case 7, in which the boundary layer is the thickest, the change of φ_{surf} with surface saturation is smoother and at a specific S_{surf} its value is always bigger than for the other two cases.
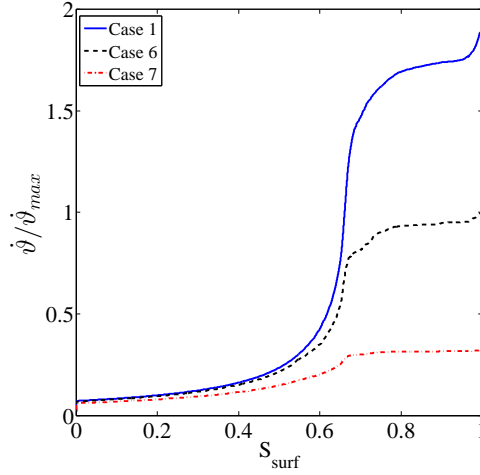
Figure 4.15: Normalized evaporation rate versus network saturation for three different boundary layer thicknesses in PN simulations of capillary-dominated regime, each of which is averaged among 15 realizations and normalized over the initial evaporation rate of Case 6.
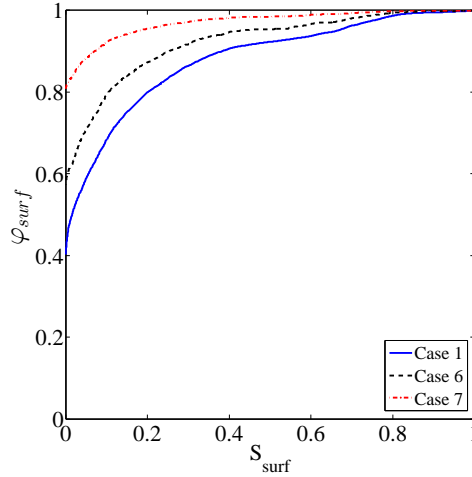
Figure 4.16: NLE function at the network surface versus surface saturation for studying the effect of δ, each of which is averaged among 15 realizations.

The different behavior seen in the NLE function at the surface with changing boundary layer thickness also affects the duration of the CRP as well as the change of evaporation rate during this period. In order to better analyze this effect on CRP, the evaporation rates of the three cases are normalized over their respective initial evaporation rates and are plotted versus network saturation, as shown in Fig. 4.17. In Case 1, after emptying a surface meniscus, its neighboring gas pore at the surface experiences a larger decrease in the vapor pressure. This is due to the fact that this gas pore is closer to the ambient, compared to Cases 6 and 7. The larger decrease in vapor pressure of gas pores neighboring to the emptied throats at the surface leads to a sharp decrease in the evaporation rate at the very beginning of the drying process, as seen for Case 1. Such a reduction in evaporation rate becomes less significant when increasing the boundary layer thickness. This is because of higher vapor pressure of gas pores neighboring to the emptied throats at the surface. This also results in an almost perfect CRP for Case 7 (for $S_{net} > 0.68$), in

contrast with the steady reduction of evaporation rate during the "CRP" for Case 1.
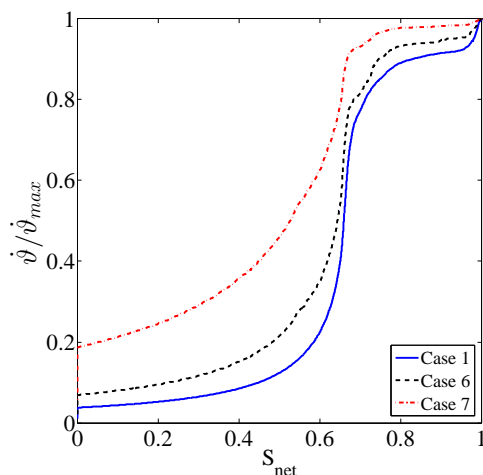
Figure 4.17: Normalized evaporation rates versus network saturation for three different boundary layer thicknesses in PN simulations of capillary-dominated regime, each of which is averaged among 15 realizations and normalized over its initial value.

With a similar argument the change of standard deviation of vapor pressure of gas pores at the surface can also be analyzed. As it was discussed in the previous paragraph, when boundary layer thickness is large, the vapor pressure of the gas pores in the dry region is closer to the saturation vapor pressure. Then, a smoother and more moderate evolution of $\sigma_{p_{vs}}$ with the change of A_w is expected. On the contrary, a small δ will lead to lower vapor pressure for the gas pores in the dry region at the surface. This means that $\sigma_{p_{vs}}$ should experience a sharper change with normalized wet surface area at the surface.

The normalized standard deviation of vapor pressure of surface pores versus A_w is shown in Fig. 4.18. Case 7 has the flattest curve, therefore, as it was discussed in the previous section, its evaporation rate curve experiences a smaller drop during the period in which the surface is partially wet (Fig. 4.17).
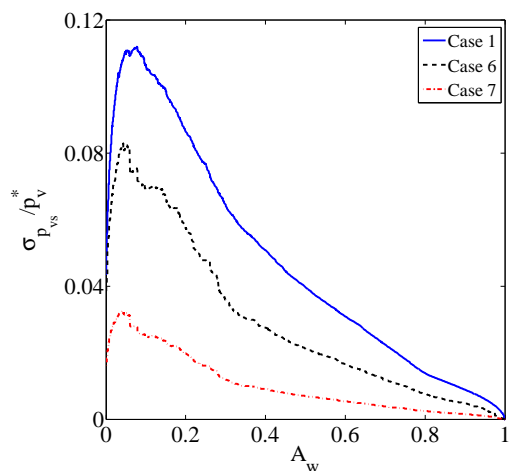
Figure 4.18: Normalized standard deviation of vapor pressure at the surface versus normalized wet surface area for three different boundary layer thicknesses in PN simulations of capillary-dominated regime, each of which is averaged among 15 realizations.

Similarly to the previous section, the mechanism for the transport of water for the cases under study in this section is capillary force. Therefore the network saturation at which the surface dries out and L_{tp}/H curves are the same.

The contributions of wet and dry regions to the total evaporation rate are the same for all three cases in this section. When the boundary layer becomes thicker, the diffusion length of the water vapor is increased for both the dry and the wet regions. Thus, the evaporation rates for both regions will decrease to the same proportion and consequently their relative contributions to the total evaporation rate will remain unchanged. Therefore the blue curves in Fig. 4.9 which belong to Case 1 are also valid for Cases 6 and 7.

4.6 Remarks

This section is partly taken from Attari Moghaddam et al. [2017c].

In this chapter the phenomena that occur at the surface during drying of porous media were studied by considering different liquid transport regimes, length of throats and boundary layer thicknesses. The effect of each of these parameters on the NLE function and the evaporation rate was specifically investigated. It was concluded that the change of liquid transport regime can barely affect the relationship between surface saturation and φ_{surf}, while boundary layer thickness and especially throat length can significantly affect it. A relationship between standard deviation of vapor pressure of surface pores and φ_{surf} was also obtained. A flatter change in $\sigma_{p_{vs}}$ would result in a smaller drop in evaporation rate and in values of φ_{surf} closer to one, which shows that the non-equilibrium phenomenon in this case is reduced. The contributions of wet and dry patches to the total evaporation rate for different cases were also investigated and it was shown that only a change in throat length can affect the transition point between these two contributions. The contribution of the dry region to the evaporation rate becomes bigger than the one from the wet region only at $A_w < 0.5$.

However the main results of this chapter are related to the concept of the NLE function and that φ_{surf} may not be a unique function for different geometrical characteristics of the network or operating conditions of the drying process. It was shown that the averaged vapor partial pressure over the partially wet surface is not the saturation vapor pressure owing to the lower vapor partial pressure in the dry pores at the surface. In the continuum approach to drying, the fact that the spatially averaged vapor pressure is different from the saturation vapor pressure in the presence of liquid water is traditionally explained by adsorption and capillary condensation phenomena and modeled invoking Kelvin's effect (Adamson and Gast [1997]). However, these phenomena are not taken into account in our pore network models (on the grounds that they can be neglected in capillary porous media).

The discrepancy between the average vapor partial pressure and the saturation pressure in drying capillary porous media is, hence, seen as a non-local equilibrium effect. Although considered by some authors (Benet and Jouanna [1983], Pujol et al. [2011]), the non-local equilibrium assumption is not accounted for in the traditional models of drying of capillary porous media. On the contrary, traditional models are based on the local equilibrium assumption, i.e. the average vapor pressure in a representative elementary volume (or at the surface) is supposed to be the same as at the surface of menisci. This strongly suggests to develop the non-local equilibrium (or two-equation) version of the continuum models for better and more consistent predictions of drying processes. Such a model should take into account a better closure relationship between the mass transfer rate at the surface and the degree of occupancy of the porous surface by the liquid than provided by Schlünder's model. It should also be able to account for the variation of the degree of non-equilibrium due to changes in geometrical characteristics of the network and operating conditions of the drying process, which was shown in this chapter.

The study was implicitly based on the assumption that the impact of corner liquid films, e.g. Chauvet et al. [2009], Vorhauer et al. [2015], is negligible since the presence of the films is not taken into account in the pore network model considered. The case where the impact of secondary capillary liquid structures, such as corner liquid films, is significant would deserve a specific study along the same lines as the present one.

In this chapter the period in which the surface is partially or fully wet was studied only focusing on the surface phenomena. However, it is obvious that the duration of this period depends on the rate of the transport of liquid towards the surface to compensate the water loss due to evaporation and keep the surface wet. Therefore, it is necessary to also investigate the kinetics of water transport inside the porous medium, so that to better understand the phenomena happening at the surface during this period. This will be discussed in the next chapter.

Chapter 5

Liquid velocity profile in drying of porous media

This chapter is partly taken from Attari Moghaddam et al. [2017a].

5.1 Introduction

As described in the previous chapter and in many works, e.g. Coussot [2000], Van Brakel [1980], the drying kinetics of a capillary porous medium under typical room conditions (i.e. temperature close to 20 °C) can be divided into three main stages: a first stage, the constant rate period (CRP), in which the evaporation rate is constant, a second stage called the falling rate period (FRP), in which the evaporation rate rapidly decreases, and a last stage, the receding front period (RFP), characterized by a receding internal evaporation region. In both the CRP and the FRP, liquid is present on the surface whereas the surface is dry during the RFP. A typical drying rate curve consisting of CRP, RFP and FRP is shown in Fig. 5.1.

From the industrial point of view, the CRP and FRP periods are of great importance, because the drying rate in these periods is high and therefore the sample loses liquid in a short time. In the previous chapter, the characteristics and behavior of the surface of the porous medium during the CRP were investigated. However, an important element of significance for the physics of drying during this period is the liquid distribution inside the sample during the process. This distribution is generally characterized using the concept of saturation, i.e. the fraction of the pore space volume occupied by liquid. As sketched in Fig. 3.1, we consider a typical drying situation in which vapor can escape only from the top surface of the sample. All other surfaces are sealed. The vertical distribution of liquid saturation during drying depends on the competition between capillary, gravitational and viscous forces (generated in the liquid by the evaporation process), e.g. Prat [2002]. For a sufficiently thin sample (as typically considered in laboratory experiments) and under slow evaporation conditions (such as evaporation of water at room temperature), the drying
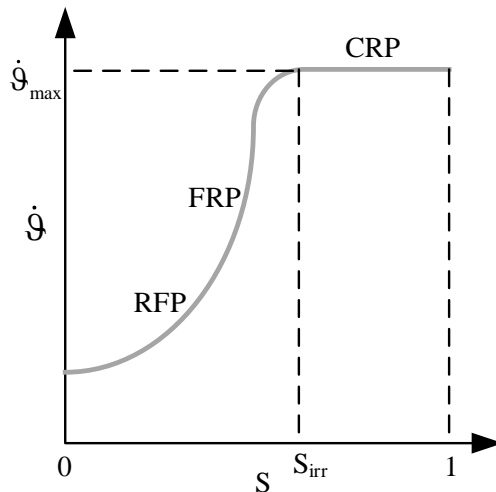
Figure 5.1: A typical drying rate curve for capillary-dominated drying of a porous sample. The transition between CRP and RFP happens at $S = S_{irr}$.

process is dominated by the capillary forces and the distribution of the saturation during most of the CRP/FRP is essentially uniform in space, i.e. approximately independent of the vertical coordinate z, e.g. Gupta et al. [2014], Huinink et al. [2002]. This drying regime is referred to as the capillary regime. Under these circumstances, it is easy to show from a mass conservation argument that the liquid velocity in the sample during the CRP/FRP varies linearly along the sample height (Huinink et al. [2002]). This derivation will be recalled in Section 5.2. It is based on the classical continuum approach for porous media modeling, in which the porous medium is regarded as a fictitious continuum. However, in the presence of viscosity or gravity, the liquid velocity profiles are not linear. In fact, to predict the exact liquid velocity profiles in such regimes from a continuum approach, one must know the relationship between saturation and depth a priori.

On the other hand, the velocity field in the liquid phase can also be computed using a pore network model. The instantaneous 3D velocity field thus computed can be averaged over horizontal slices so as to determine the mean velocity in the z direction. For the capillary-dominated case, in contrast to the velocity field obtained from the continuum description, the averaged velocity obtained from pore network simulations does not vary linearly in the vertical direction, but a step profile is obtained instead. The velocity is typically uniform up to a certain depth within the sample and then vanishes very rapidly as the depth increases; not considering here a thin layer adjacent to the evaporative surface referred to as the edge effect region later in this chapter. The same type of instantaneous velocity profile is observed in the gravity-capillary regime, with the position of the step change in the velocity profile to be related to the position of the meniscus with the highest capillary potential. However, in the presence of viscosity, the instantaneous velocity profile from PN drying simulations is different compared to the ones obtained when neglecting the viscosity. The velocity profile in this case is not uniform and fluctuates up to a certain

depth inside the network and then vanishes rapidly as the depth increases.

The main objective of this chapter is to reconcile the continuum description of the velocity field during the CRP in the capillary regime with the more detailed information obtained from the pore network model. In doing so, we will also reveal new information regarding the velocity field in a slowly drying capillary porous medium. The velocity field in the presence of stabilizing forces will also be obtained from both approaches and compared with the fields obtained for the capillary-dominated regime.

Somewhat surprisingly at first glance and in contrast to the viscous-capillary or gravity-capillary regimes, there is actually no need to compute the velocity field in the liquid phase to predict the saturation distribution during the CRP in the capillary regime, neither in the continuum approach nor in the pore network model. Actually, this is fully consistent with the fact that the capillary forces are dominant in this regime. The velocity field becomes important, however, when species such as ions or colloidal particles, for example, are present in the liquid, e.g. Desarnaud et al. [2015], Eloukabi et al. [2013], Guglielmini et al. [2008], Hidri et al. [2013], Keita et al. [2013, 2016], Norouzi Rad et al. [2013]. The transport of these species during drying and thus their distribution within the porous medium are highly dependent on the velocity field induced in the liquid by the evaporation process. For instance, the occurrence of salt efflorescence at the surface of a drying porous medium is related to the convective transport of ions toward the evaporative surface by the velocity field, e.g. Eloukabi et al. [2013], Huinink et al. [2002], Veran-Tissoires and Prat [2014].

5.2 Velocity field obtained from the continuum approach

The average liquid saturation variation during the CRP/FRP can be related to the evaporation flux j by a simple mass balance,

$$j = \frac{J}{A} = -\frac{m_0}{A}\frac{dS_{net}}{dt},$$

(5.1)

where m_0 is the mass of liquid saturating the porous medium initially ($m_0 = AH\rho_\ell\varepsilon$).

Using similar arguments as in Huinink et al. [2002], the velocity profile can then be deduced as follows: The local mass balance equation reads

$$\frac{\partial S_{loc}}{\partial t} + \frac{\partial}{\partial z}(US_{loc}) = 0.$$

(5.2)

S_{loc} is spatially uniform in the capillary regime, which enables us to combine Eqs. 5.1 and Eq. 5.2, noting that the velocity is zero at the sample bottom (at z = 0). This leads to expressing the velocity profile in the capillary-dominated regime as

$$U(z) = \frac{Aj}{S_{loc}m_0}z = \frac{j}{\varepsilon S_{loc}\rho_\ell}\frac{z}{H}. \tag{5.3}$$

Note that U represents the average velocity in the pores, referred to as the interstitial velocity, and not the filtration (Darcy's) velocity U_D. Recalling that

$$U_D = \varepsilon S_{loc}U \tag{5.4}$$

we obtain

$$U_D(z) = \frac{j}{\rho_\ell}\frac{z}{H}. \tag{5.5}$$

Hence in capillary regime the interstitial velocity (as well as the Darcy velocity) varies linearly along the height of sample, is maximum at the evaporative surface (where $U(H) = \frac{j}{\varepsilon S_{loc}\rho_\ell}$ and $U_D(H) = \frac{j}{\rho_\ell}$) and vanishes at z = 0. While the filtration velocity does not vary in time during the CRP, the interstitial velocity increases as a function of time at a given location since the saturation S_{loc} decreases as a function of time.

In the presence of viscosity or gravity saturation inside the network is not uniform, but a function of z. Therefore combining Eq. 5.1 with Eq. 5.2 will work only if the functionality of local saturation with z is known a priori. However, by knowing the saturation profiles at each time and by using Eq. 5.2, it is possible to obtain the velocity field in the presence of gravity or viscosity. For this purpose, first the network is divided into N control volumes (CV), with the first CV located at the bottom, as shown in Fig. 5.2.

By knowing the saturation values everywhere in the network, according to Eq. 5.2, and assuming that liquid velocity at the bottom end of the network is zero, the velocity of the first control volume can be obtained as

$$U_1\overline{S}_1 = -a\frac{\Delta S_1}{\Delta t}, \tag{5.6}$$

in which $\overline{S}_1$ and ΔS_1 are the average saturation of the first CV and the change of its saturation during the period t until $t + \Delta t$, respectively; a is the height of the control volume. Similarly for the control volume 2,
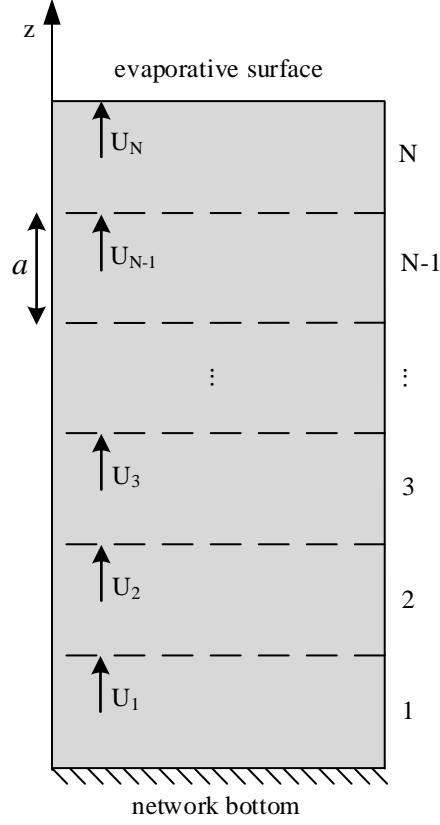
Figure 5.2: Control volumes for the calculation of velocity profiles.

$$U_2\overline{S}_2 - U_1\overline{S}_1 = -a\frac{\Delta S_2}{\Delta t}. \tag{5.7}$$

Combining Eqs. 5.6 and 5.7,

$$U_2\overline{S}_2 = -a\frac{\Delta S_1}{\Delta t} - a\frac{\Delta S_2}{\Delta t} = -\frac{a}{\Delta t}(\Delta S_1 + \Delta S_2). \tag{5.8}$$

Therefore the liquid velocity for the control volume i is

$$U_i = -\frac{a}{\overline{S}_i\Delta t}\sum_{n=1}^{i}\Delta S_n. \tag{5.9}$$

By combining Eqs. 5.4 and 5.9, the filtration velocity for control volume i is obtained as

$$U_{Di} = -\frac{a\varepsilon_i}{\Delta t}\sum_{n=1}^{i}\Delta S_n. \tag{5.10}$$

In the CRP of the capillary-dominated regime, saturation profiles stay uniform, therefore the amount of water loss during time Δt will be the same at every position in the network. This means that

$$\frac{\Delta S_N}{\Delta t} = \frac{\Delta S_{N-1}}{\Delta t} = ... = \frac{\Delta S_2}{\Delta t} = \frac{\Delta S_1}{\Delta t}. \tag{5.11}$$

Therefore Eq. 5.8 can be rewritten as

$$U_2 \overline{S}_2 = -2a\frac{\Delta S_1}{\Delta t} = 2U_1 \overline{S}_1. \tag{5.12}$$

Knowing that the saturation is uniform throughout the sample, $U_2 = 2U_1$, and in general for control volume i in the capillary-dominated regime and in the CRP

$$U_i = iU_1. \tag{5.13}$$

In fact, Eq. 5.13 confirms Eq. 5.3, showing that during drying in the capillary-dominated regime the velocity profile changes linearly with the medium depth.

5.3 Computation of the velocity field by pore network simulations

We consider three regimes to investigate their liquid velocity field: capillary-dominated, gravity-capillary and viscous-capillary regime. In the absence of viscosity, i.e. in the capillary-dominated and gravity-capillary regimes, the evolution of the phase distribution during drying is essentially seen as a succession of quasi-static hydrostatic equilibria. The passage from one equilibrium configuration to the next is a very rapid event, referred to as a (global) Haines jump, e.g. Armstrong and Berg [2013], which corresponds to the full invasion of a single throat by the gas phase in our model. During the Haines jump, viscous and even inertial effects are not negligible (Armstrong and Berg [2013]). The time scale of the very rapid events corresponding to Haines jumps has not yet resolved. It is assumed that these phenomena do not affect the successive equilibrium fluid configurations obtained by using purely quasi-static invasion rules, which is in accordance with experimental observations in model systems, e.g. Ferrari and Lunati [2014], Jung et al. [2016], Laurindo and Prat [1996].

The fact that the velocity generated in the liquid during the drying process in the absence of viscosity has a negligible influence on the time-evolution of the phase distribution does not mean that there is no velocity (in a quasi-static equilibrium configuration). The velocity field originates from the so-called pumping effect to stable menisci at the periphery of each liquid cluster. The pumping effect is schematically illustrated in Fig. 5.3. Consider a stable meniscus, i.e. a meniscus which is not located at the entrance of the throat with the largest capillary potential (see Eq. 2.1) along the periphery of the cluster

to which this meniscus belongs. For the meniscus to be stable there must be a liquid flow rate toward this meniscus compensating the evaporation rate from this meniscus. Therefore, a flow is induced in each cluster from the unstable menisci toward the stable menisci. This is called the pumping effect. In the absence of viscosity, there is only one throat containing an unstable meniscus in each cluster (inside the interfacial throat with the largest potential).
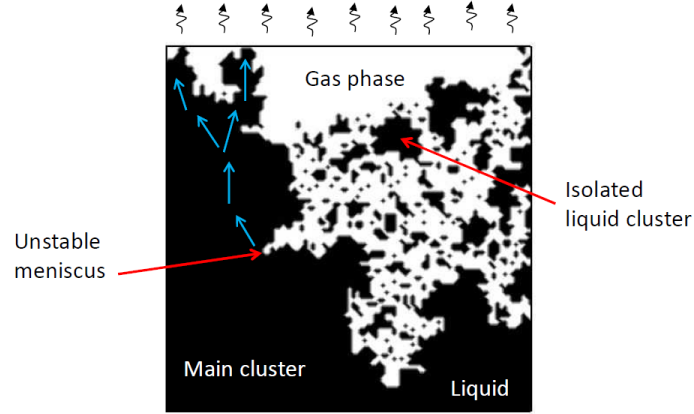
Figure 5.3: Sketch of the pumping effect. The liquid is pumped by capillary action from the region of the unstable meniscus toward the region with high evaporation rates. The liquid motion resulting from the pumping effect is schematically represented by blue arrows.

The method to compute this flow from unstable to stable menisci within each cluster in the absence of viscosity is as follows: The volumetric flow rate between two liquid pores i and j in a cluster is expressed using Poiseuille's law as

$$q_{ij} = \frac{g_{ij}}{\mu} \Delta P_{ij}, \tag{5.14}$$

where $\Delta P_{ij} = P_i - P_j$ is the pressure difference between pores i and j and g_{ij} is the hydraulic conductance of the channel connecting the pores i and j,

$$g_{ij} = \frac{\pi r_{t,ij}^4}{8 L_t}. \tag{5.15}$$

Expressing the mass conservation at each liquid pore of each cluster,

$$\sum_{j=1}^{6} q_{ij} = 0 \tag{5.16}$$

then yields a linear system which is solved numerically for the pressure in each pore of each cluster. To this end boundary conditions must be specified. At a throat containing a stable meniscus, the flow rate from the adjacent liquid pore compensates the evaporation

rate J_{sm} from this meniscus. Thus

$$q_{sm} = \frac{J_{sm}}{\rho_\ell}, \tag{5.17}$$

where J_{sm} is computed from the numerical solution of the vapor diffusive transport problem in the gas region of the network. The pressure in the liquid pore um adjacent to the unstable meniscus is fixed for simplicity, assuming $P_{um} = P_{atm}$, where P_{atm} is the gas phase total pressure (which is constant throughout the gas phase). One should realize that the flow rate computed in each channel is actually independent of μ and P_{atm}. However, a too low viscosity can lead to numerical problems whereas a too high viscosity is physically not consistent with the assumption that there is only one moving meniscus in a given cluster (this, though, has no impact as long as the identification of the moving meniscus is based on the largest capillary threshold). These channel flow rates are computed from the pressure field using Eq. 5.14. Then the average velocity in each liquid channel can be determined as

$$\overline{u}_{ij} = \frac{q_{ij}}{\pi r_{t,ij}^2}. \tag{5.18}$$

Once the flow rates have been determined in each liquid channel, the flow rate through each horizontal slice k of the network is computed as

$$Q_k = \sum_{m=1}^{n} q_m, \tag{5.19}$$

where n is the number of vertical liquid throats considered in the x-y plane. The filtration velocity in the z direction is then determined as

$$U_{Dk} = \frac{Q_k}{A}. \tag{5.20}$$

As illustrated for a piece of a 2D vertical slice of the network in Fig. 5.4, one can distinguish four types of (vertical) throats: liquid throats (between two liquid pores), gaseous throats (between two gaseous pores), isolated liquid throats (marked in red in Fig. 5.4) and cluster liquid throats containing a meniscus (also referred to as the interfacial throats of a liquid cluster). Three of the latter are indicated with white arrows in Fig. 5.4. The filtration velocity is computed considering only the throats belonging to a liquid cluster, namely the liquid throats and the interfacial throats. There is no liquid flow rate computed in the isolated liquid throats. For a given cluster, the throat with the biggest

capillary potential is the one containing the moving meniscus. The mass flow rate in this throat is the sum of the evaporation rates from all stable menisci of the considered cluster. Note also that the flow rate in a vertical liquid throat (liquid or interfacial) is counted positive if the velocity is upward and negative if the velocity is downward.
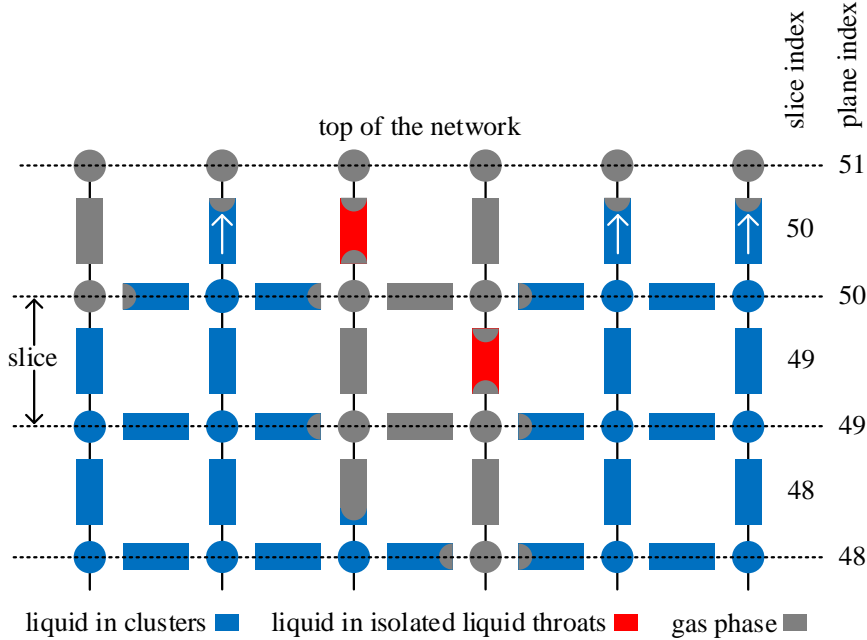
Figure 5.4: Illustration of the various types of throats present in the network during drying.

As in Le Bray and Prat [1999] and Yiotis et al. [2006], we define as the main cluster (mc), the biggest liquid cluster connected to the network top of the two-phase region. As a result, the filtration velocity can be decomposed into two contributions, corresponding respectively to the main cluster and the other clusters (referred to as the isolated clusters (ic)),

$$U_D = U_{Dmc} + U_{Dic} \tag{5.21}$$

The computation of each component is similar to U_D, Eq. 5.20, decomposing Q_k into $Q_k = Q_{mck} + Q_{ick}$. The interstitial velocity cannot be readily deduced from the classical formula $U_k = \frac{U_{Dk}}{\varepsilon S_k}$, where S_k is the slice-averaged saturation, because we are interested only in the vertical component of the interstitial velocity. A simple method to compute U_k is,

$$U_k = \frac{Q_k}{A_{wk}} \tag{5.22}$$

where A_{wk} is the sum of the cross section areas of the liquid throats in slice k.

In drying of porous media in the presence of the viscosity, in contrast to capillary-

dominated and gravity-capillary regime, the capillary pumping effect could originate from more than one meniscus at each time step. In other words, the number of unstable menisci could be more than one. This is due to the extra resistance due to viscous forces in the liquid phase, which resist against free movement of water from the throat with the largest capillary potential. Therefore the instantaneous velocity profile at each time step obtained from PN drying simulations could be affected by more than one unstable menisci. However, here the slice-averaged instantaneous velocity profile can be calculated similar to the cases in the absence of viscosity, provided that the value of viscosity is already known.

5.4   Liquid flow in capillary-dominated regime

In order to obtain the PNM and continuum velocity profiles, pore network drying simulations have been performed. The pore network model has been explained in Chapter 2. The results regarding the capillary-dominated regime will be discussed first and in more detail, so that to give a comprehensive insight into the velocity profiles during drying. By analysis of the capillary-dominated regime, the edge effect on the velocity profiles will also be thoroughly studied. After that results related to the stabilized regimes will be shown.

5.4.1   Pore network drying simulations

The PN drying simulations for the capillary-dominated regime are the same as the ones mentioned in Chapter 4. The network size is $25 \times 25 \times 51$ and the results were averaged over 15 realizations. The complete simulation parameters can be found in Appendix A.

Drying rate   The drying curve obtained from PN simulations averaged over 15 realizations is shown in Fig. 5.5. There are some differences between this drying rate curve and the typical drying rate curve for the capillary-dominated regime considered in the classical literature, e.g. Van Brakel [1980], shown in Fig. 5.1. The first difference is the decrease in evaporation rate right from the beginning of the drying process, similarly as in previous drying PN simulations, e.g. Le Bray and Prat [1999], Yiotis et al. [2006]. This immediate drop was discussed in the previous chapter by analyzing the evaporative surface. There, it was mentioned that the length of the throats and boundary layer thickness can affect this drop. However the main reason for this phenomenon, which should be studied by considering what happens inside the network, was not discussed. In fact, this immediate drop is due to the invasion of surface pores during the very first stage of drying until the gas phase breakthrough, i.e. until the gas phase reaches the bottom of the sample for

the first time. From percolation theory (Wilkinson [1986]), we know that the gas phase saturation in a cubic system with edge length L scales like
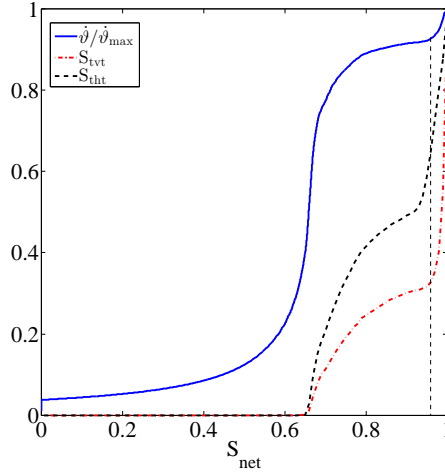
Figure 5.5: The normalized evaporation rate (blue-solid), the saturation of top vertical throats (red-dotted) and the saturation of top horizontal throats (black-dashed), averaged among 15 realizations for capillary-dominated drying.

$$S_{gBT} \propto L^{D_f - D} \tag{5.23}$$

at breakthrough, where D is the space dimension (D = 3), D_f is the fractal dimension of the percolation cluster ($D_f = 2.52$, in 3D) and L is the system size (in the simulations in this work, $L = H \approx N_z a$). Thus $S_{gBT} \propto L^{-0.48}$ for 3D systems (Stauffer and Aharony [1994]). As a result, the gas saturation at breakthrough is very small in a large network, i.e. a typical porous medium sample. This explains why this very first period cannot be seen in experiments, because the corresponding evaporated mass is actually very small compared to the total mass of liquid initially present in the sample. Conversely, the relative importance of this period in our simulations can be related to a finite size effect.

This very first period is further illustrated by looking at the average saturation of the top vertical throats (S_{tvt}) versus network saturation (Fig. 5.5). As can be seen, the sharp decrease in the average saturation of top vertical throats is followed by a drop in the evaporation rate during this period. This also holds for the saturation of top horizontal throats (S_{tht}). One can refer to Fig. 2.1 for the definition of top vertical throats and top horizontal throats. As can be seen, the decrease in drying rate occurring in this very first period affects the drying rate during the CRP, which starts at the end of this initial period. The evaporation rate is actually not perfectly constant but varies weakly during the constant rate period. This has also been observed in previous pore network simulations, e.g. Le Bray and Prat [1999], Yiotis et al. [2006]. Compared to classical experimental results, the CRP obtained from the simulations is quite short (the saturation range corresponding to the CRP is much narrower than in the experiments).

Several factors explain this difference: First, the irreducible saturation, i.e. the saturation for which the liquid phase is no longer connected over a distance comparable to the system size, is quite high in our system ($S_{irr} \approx 0.68$) compared to a random packing of monodisperse spherical particles ($S_{irr} \approx 0.1$, Dullien et al. [1989]) or the fired clay brick considered in Gupta et al. [2014] ($S_{irr} < 0.1$). This has to do with the coordination number of our network (each pore is connected to 6 neighbor pores) which is low compared to the average coordination number in real systems. Second, the fact that the pores are volumeless and thus that all the pore space volume is in the channels (throats) leads to a greater irreducible saturation ($S_{irr} \approx 0.68$ vs $S_{irr} \approx 0.45$ for the network considered in Le Bray and Prat [1999] for instance). The high irreducible saturation favors an earlier end of the CRP owing to an earlier fragmentation of the liquid phase into isolated clusters. Third, the external mass transfer boundary layer thickness measured in lattice spacing units is quite small in our simulations ($\delta = 10a$) compared to experiments with real systems (for example $\delta = 100a$ for a typical convective boundary layer of 1 mm over a micrometer-sized porous medium characterized by a mean distance of 10 μm between adjacent pores). This favors a greater impact on the drying kinetics of changes in the throat saturations near the top surface of the network.

Horizontal slice-averaged saturation profiles The average slice saturation inside the pore network for different network saturations is shown in Fig. 5.6. These results are in quite good qualitative agreement with the experimental profiles measured by NMR reported for example in Gupta et al. [2014] (see Fig. 2a in this reference) if one takes into account that 1) the irreducible saturation is much higher with our cubic network as explained previously, and 2) the initial period up to the gas breakthrough which is, as explained, difficult to observe in experiments. This period corresponds to the topmost profile in Fig. 5.6 characterized by a liquid saturation which increases with the depth. If one disregards this first profile, an almost uniform saturation profile for total network saturations greater than the irreducible saturation ($S_{irr} \approx 0.68$) is observed, similarly as in the experiments. One can observe, however, a sharp drop in saturation at positions near the evaporative surface. This was also observed in previous PN simulations, e.g. Le Bray and Prat [1999], Yiotis et al. [2006], and even more interestingly in the experimental profiles obtained by NMR, e.g. Faure and Coussot [2010], Gupta et al. [2014].

This sharp drop is due to the preferential invasion in the top horizontal and vertical throats (S_{tht}, S_{tvt}), as shown in Fig. 5.5. The emptying of the top vertical throats leads to the formation of many isolated horizontal single liquid throats just below the top pores. These isolated single liquid throats are disconnected from the body of the liquid phase inside the network, and therefore they empty quickly, leading to a lower saturation near the top compared to deeper inside the network. Similarly as in the PN simulations reported in Le Bray and Prat [1999] (see Fig. 5 in this reference) over a network twice as large, this

edge effect actually affects about the 3-4 first rows of pores. It is, however, unclear how the extent of this near surface region will change with the network size. The fact that the saturation edge effect is also observed in experiments suggests that the size of the region affected by the saturation edge effect increases with network size. This edge effect has clearly an impact on the drying kinetics as shown in Fig. 5.5.
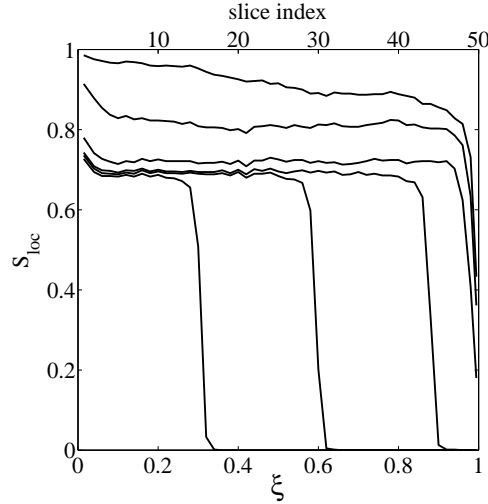
Figure 5.6: Saturation profiles of capillary-dominated drying obtained from PN simulations and averaged over 15 realizations. From the top, profiles corresponding to the network saturations 0.9, 0.8, 0.7, 0.6, 0.4 and 0.2, respectively; $\xi = z/H$. The evaporative top surface of the network is located at $\xi = 1$.
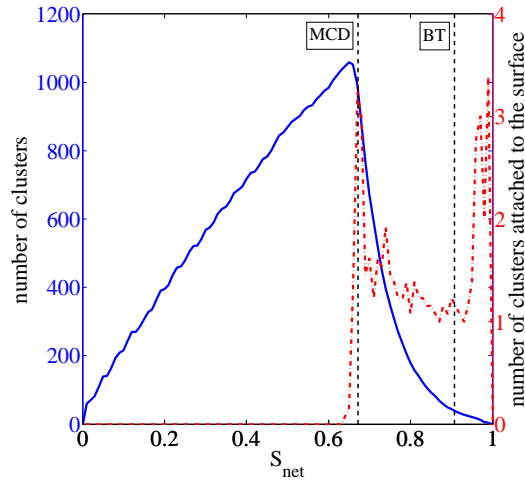
Figure 5.7: Number of liquid clusters present in the pore network and number of liquid clusters connected to the top surface as a function of overall saturation. The data are averaged over 15 realizations.

Liquid cluster formation   As mentioned earlier and quantitatively illustrated for our pore network in Fig. 5.7, liquid clusters form during drying. The number of clusters increases during the CRP/FRP until the main cluster detaches from the top surface of the network. This event is referred to as the main cluster disconnection (MCD) (Le Bray and Prat [1999], Yiotis et al. [2006]). The number of clusters connected to the top surface of the network is quite low, however, varying typically between 1 and 2 during the CRP/FRP.

Thus the liquid phase fragmentation, i.e. the formation of clusters, takes place mostly inside the network. The results reported in Fig. 5.7 also give insights into the edge effect since there are clusters connected to the top surface forming during the short period before breakthrough. These clusters evaporate during this initial phase, which leads to the formation of dry pockets connected to the surface. Figure 5.8 presents similar results when the isolated liquid throats are taken into account. The comparison between Fig. 5.7 and Fig. 5.8 shows that many isolated liquid throats form within the network. The isolated throats connected to the surface rapidly evaporate during the initial short period before BT. The formation and evaporation of those throats contributes to the edge effect and to the modification of the liquid distribution right at the surface between the initial distribution (all the vertical throats attached at the surface are filled with liquid) and the distribution when the CRP starts (some throats are empty).
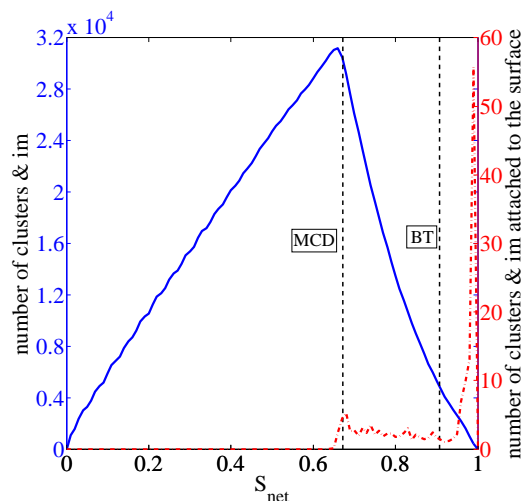
Figure 5.8: Number of liquid clusters present in the pore network plus number of isolated menisci (im) and number of liquid clusters plus isolated menisci connected to the top surface as a function of overall saturation. The data are averaged over 15 realizations.

5.4.2 Mass flow rate partition

To obtain first insights on the slice-averaged velocity field in the network, we compute the total mass flux Q_m reaching the top plane of each slice from below. It can be expressed as

$$Q_{mk} = \rho_\ell U_{Dmck} A + \rho_\ell U_{Dick} A + Q_{gk} + Q_{itk}, \qquad (5.24)$$

where Q_{gk} is the diffusive mass flow rate between the horizontal planes k and k+1 (see Fig. 5.4) through the vertical gaseous throats connecting the two planes (these throats are shown in grey in Fig. 5.4). Q_{itk} is the evaporation rate from the top menisci of the isolated liquid throats (marked in red in Fig. 5.4) located in the slice.

The variation of each contribution to Q_m as a function of z is shown in Fig. 5.9 for three different overall saturations in the CRP/FRP for cases where the moving meniscus in the main cluster is not very far from the network bottom.
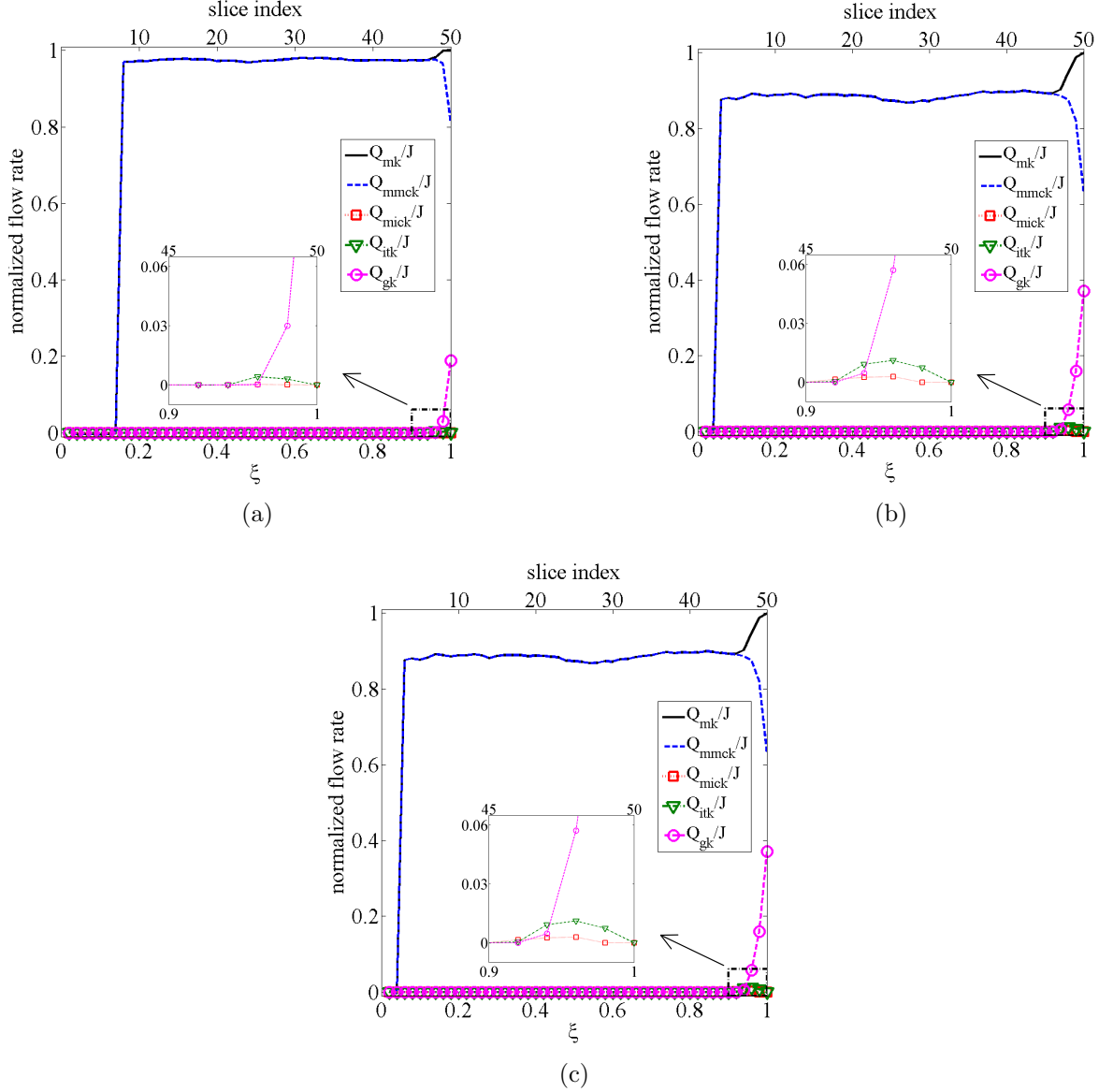
Figure 5.9: Variation of contributions to Q_m (Eq. 5.24) as a function of z for $S_{net} = 0.9$ (a), $S_{net} = 0.8$ (b) and $S_{net} = 0.7$ (c); $Q_{mmck} = \rho_\ell U_{Dmck} A$; $Q_{mick} = \rho_\ell U_{Dick} A$; J is the evaporation rate corresponding to each global saturation.

As can be seen from Fig. 5.9, one must distinguish the thin edge effect region from the rest of the network, referred to as the bulk in what follows. In the bulk, the transport in the gas phase is completely negligible and there is no contribution of the isolated clusters to the liquid transport. The evaporation from those clusters is screened and therefore negligible. Indeed, the pore network simulations indicate that the vapor partial pressure in the pores of the network invaded by the gas phase is very close to the saturation pressure (equilibrium vapor partial pressure imposed at the surface of each meniscus).

This is consistent with the classical description, e.g. Van Brakel [1980], considering that the transport of vapor is negligible within the porous medium compared to the transport in the liquid phase during the CRP. The transport in the bulk therefore occurs in the liquid phase and through the main cluster (which is connected to the top surface of network). The situation is more complex in the edge effect region where the contribution of isolated clusters, although quite weak, is not completely negligible. However, the most significant change is that the transport in the gas phase is noticeable in this region. Because of the edge effect and the contribution of the gas diffusive transport, the filtration velocity is not simply given by $U_D = J/(A\rho_\ell)$ (which is the continuum model prediction), but actually $U_D < J/(A\rho_\ell)$ in the bulk and decreasing within the edge effect region in the direction of the network top surface.

5.4.3 Slice-averaged velocity profiles

As illustrated in Fig. 5.10, horizontal slice-averaging of the instantaneous velocity field in the network produces step velocity profiles which are markedly different from the linear profile predicted by continuum models (Eq. 5.5).
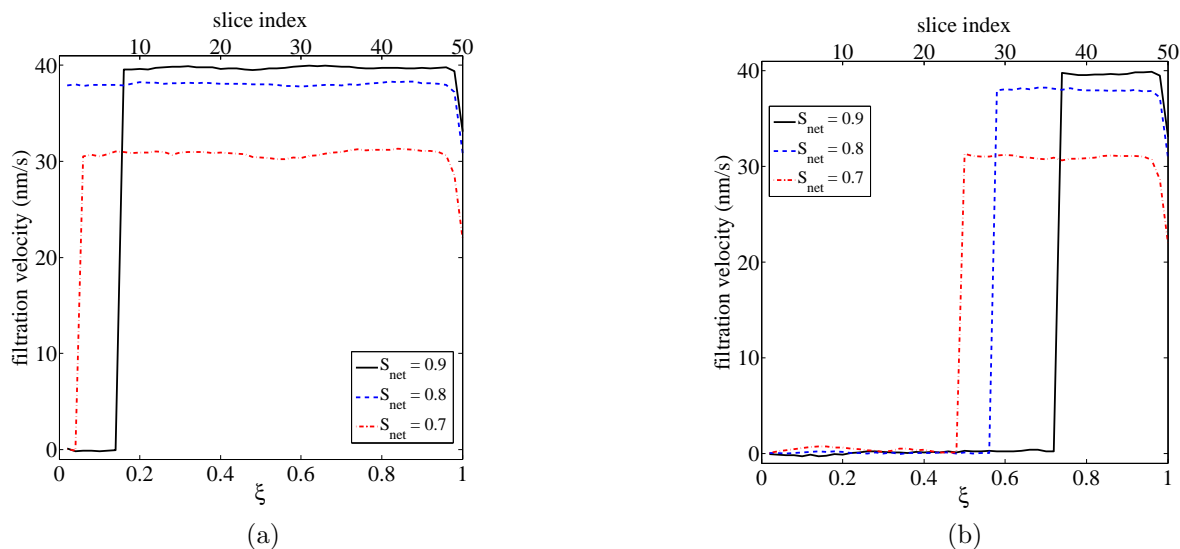
Figure 5.10: Example of slice-averaged velocity profiles: (a) profiles corresponding to the data shown in Fig. 5.9 (moving meniscus in the lower part of the network), (b) velocity profiles for comparable saturations as in Fig. 5.10a but with a moving meniscus in the main cluster located closer to the network top surface ($\xi = 1$).

The step velocity profile can be explained as follows: As shown in Fig. 5.9, there is no evaporation inside the network. Thus, the vapor transport is negligible within the porous medium compared to the transport in the liquid phase. Thus evaporation takes place only from the menisci close to the porous medium surface, namely within the edge effect region (as illustrated in Fig. 5.9). The physical picture is then as sketched in Fig. 5.11.

Based on the results presented in Fig. 5.9, the liquid phase is essentially moving in a
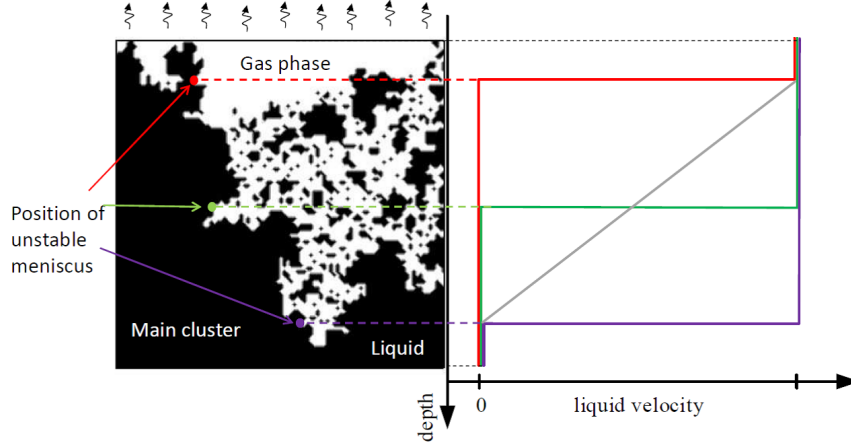
Figure 5.11: A 2D schematic phase distribution in a porous sample during capillary-dominated drying (left picture) and three velocity profiles of single invasion events corresponding to three different positions of the unstable meniscus and their average (in grey) (right picture).

single cluster, referred to as the main cluster. Thus, we only consider this cluster. Let k_{um} be the plane in which the moving meniscus in the main cluster is located at the time considered. Since there is no evaporation within the porous medium but only at its surface, the filtration velocity is actually different from zero only in the planes located above the plane k_{um}. Furthermore, since again the internal evaporation is negligible, the filtration velocity is actually uniform and constant in the planes located above the plane k_{um}. As a result, the PNM filtration velocity profiles is given by

$$U_{Dz} = \frac{J}{A\rho_\ell} \quad for \quad k_{um} < k \leq N \quad and \quad U_{Dz} = 0 \quad for \quad 1 \leq k < k_{um} \tag{5.25}$$

5.4.4 Reconciling the continuum and discrete velocity fields

The vertical filtration velocity profile deduced from the continuum approach (Eq. 5.5, the velocity increases linearly from bottom to top) is markedly different from the one obtained with the PNM model (Eq. 5.25, step profile).

To reconcile the two approaches, an approximation is to consider that the unstable meniscus position can be located in any horizontal plane with equal probability. To this aim, a fraction of moving menisci in the main cluster in each slice is obtained by averaging over fifteen realizations. The procedure to obtain these results is as follows: First, for each realization at each position the fraction of invasions in the main cluster is obtained. 1000 invasions in all clusters and isolated throats at each overall saturation are considered, and then the number of invasions in the main cluster in each plane is divided by 1000. The same method is applied to other realizations. Second, for each overall saturation, in each position all the fractions of invasions in the main cluster, obtained from 15 realizations, are summed up and then divided by 15. As can be seen from Fig. 5.12, this is only a fair

approximation. According to the PN approach the velocity field varies from one to the next channel invasion event in the main cluster. The next step is then to average the PN velocity field over a certain number of invasion events N, which is equivalent to a time averaging,

$$\langle U_{Dz} \rangle_k = \frac{1}{N} \sum_{i=N_i}^{N_i+N} U_{Dzi}(k). \tag{5.26}$$
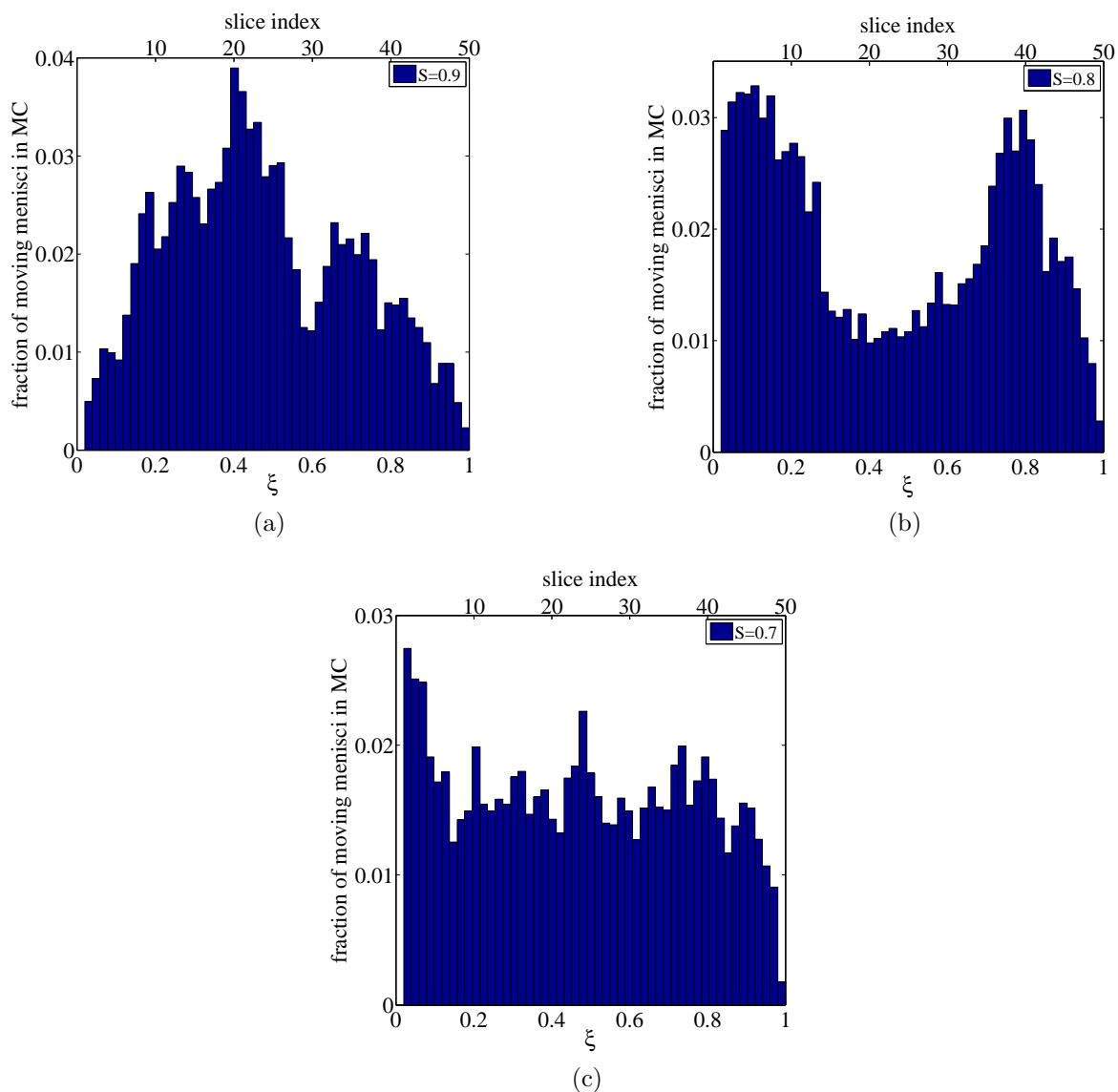
Figure 5.12: Fraction of moving menisci in the main cluster in each slice obtained by averaging over fifteen realizations for S = 0.9 (a), S = 0.8 (b) and S = 0.7 (c).

This can be expressed as

$$\langle U_{Dz} \rangle_k = \frac{1}{N} \sum_{i=N_i}^{N_i+N} U_{Dzi}(k) = \frac{N_{<k}}{N} \frac{J}{A\rho_\ell}, \tag{5.27}$$

where $N_{<k}$ is the number of invasions (out of N) for which the unstable meniscus is located below plane k. Hence $\frac{N_{<k}}{N}$ can be interpreted as the probability that the unstable meniscus is located below plane k. Assuming that the unstable meniscus can be located in any horizontal plane with equal probability,

$$\frac{N_{<k}}{N} \approx \frac{(k-1)}{N_z} \tag{5.28}$$

where N_z is the total number of horizontal planes in the network. Combining Eq. 5.27 with Eq. 5.28 yields

$$\langle U_{Dz} \rangle_k = \frac{(k-1)a}{N_z a} \frac{J}{A\rho_\ell} \approx \frac{z_k}{L} \frac{J}{A\rho_\ell}, \tag{5.29}$$

which is a discrete version of Eq. 5.5.

Thus the filtration velocity (as well as the interstitial velocity) of the continuum approach can be interpreted as a time-averaged velocity of the PN approach. This is illustrated in Fig. 5.13 from the numerical PN simulations. In Fig. 5.13, instantaneous step velocity profiles corresponding to various single invasions needed to obtain a quasi-linear average velocity profile are shown for network saturations 0.9, 0.8 and 0.7. The blue lines show the step velocity profiles associated with each single invasion. The average velocity profile is shown in purple. The number of invasions per realization needed to obtain the quasi-linear average velocity profiles for network saturation 0.9, 0.8 and 0.7 are on average 751, 761 and 806, respectively.

The procedure to obtain the average velocity profiles is actually the following. Overall saturation intervals are defined, between $S_{net} + 0.05$ and $S_{net} - 0.05$. These intervals are considered to obtain the average velocity profile for each realization and each corresponding overall saturation. Then for each overall saturation, averages are computed among all velocity profiles obtained from all realizations (summing up 15 values of velocity at each position obtained from 15 realizations and dividing it by 15). This gives the values shown in Fig. 5.13 (purple curves). For each realization, the number of invasions (in all clusters and isolated throats) in the three aforementioned overall saturation intervals is counted and summed up over all realizations. Then these 3 numbers are divided by 15 to give the average number of invasions at each overall saturation, which are used to produce the curves in Fig. 5.13 (purple). It can be also mentioned that the numbers of invasions corresponding to each overall saturation interval for different realizations are very close to each other (plus/minus 10 invasions difference between realizations).
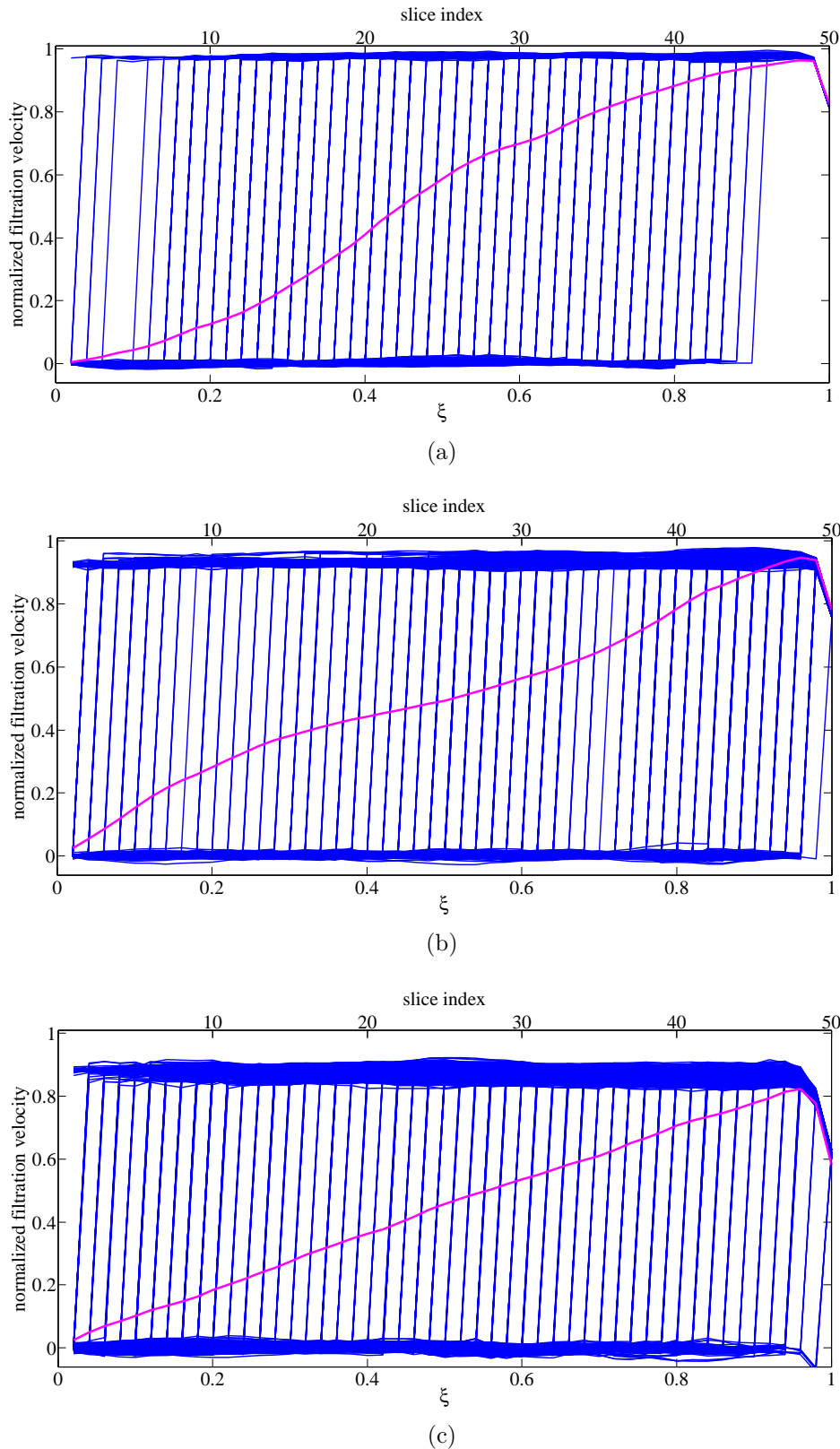
Figure 5.13: Normalized step filtration velocity profiles induced by single invasions (blue lines) for a single realization in the capillary-dominated regime for network saturations 0.9 (a), 0.8 (b) and 0.7 (c) obtained from PN simulation. The average velocity profile between all invasions and realizations is also shown in purple. The velocities are normalized by $J/(A\rho_\ell)$ where J is the evaporation rate corresponding to each overall saturation.

The time-averaged velocity profiles thus obtained are shown together in Fig. 5.14. In ad-

dition to obtaining a quasi-linear variation consistent with the velocity profiles obtained within the continuum framework, Fig. 5.14 illustrates the impact of the edge effect characterized by a drop in the velocity in the edge effect region. This drop is not predicted within the framework of the continuum approach.
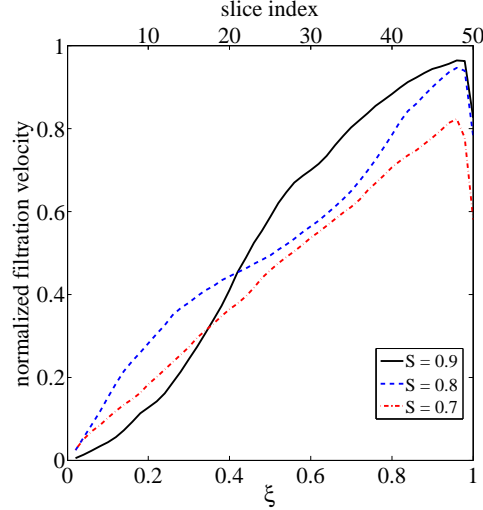
Figure 5.14: Normalized velocity profiles in the capillary-dominated regime obtained from time-averaging of single invasion velocity profiles over all realizations for three different network saturations. The velocities are normalized by $J/(A\rho_\ell)$ where J is the evaporation rate corresponding to each overall saturation.

The fact that the average profiles are not perfectly linear is consistent with the histograms shown in Fig. 5.12. For example for $S_{net} = 0.8$, one can see that the slope of the velocity profile at the bottom ($\xi <\sim 0.2$) is greater than for the other two velocity profiles. This is consistent with the fact that the histogram (Fig. 5.12) indicates that there are many invasions happening at those positions. Also, the slope of this filtration velocity profile in Fig. 5.14 decreases in the interval ($\sim 0.2 < \xi <\sim 0.6$). This is consistent with the histogram in Fig. 5.12 indicating that there are not many invasions happening within this interval (compared to the region $\xi <\sim 0.2$). Finally, an increase in the slope of the average filtration velocity is again observed in the region $\xi >\sim 0.7$, which is due to the presence of many moving menisci in this part.

As it was explained before, the mass conservation law predicts a linear liquid velocity profile, if the saturation profiles are uniform and evaporation rate stays constant during the CRP (Eq. 5.5). However none of these two conditions is fulfilled in our PN drying simulations. In order to obtain the "real" filtration velocity profiles from the continuum approach in our simulations, Eq. 5.10 can be used. The results along with the normalized velocity profiles obtained from PN drying simulations are shown in Fig. 5.15.

As it is seen in Fig. 5.15, the velocity profiles of the two approaches are in good agreement. The deviation of velocity profiles from the linear line for the results obtained from the continuum approach is due to the fact that $\Delta S/\Delta t$ is not equal for all the control volumes (here a control volume is a slice composed of one plane in PN). The increase in the
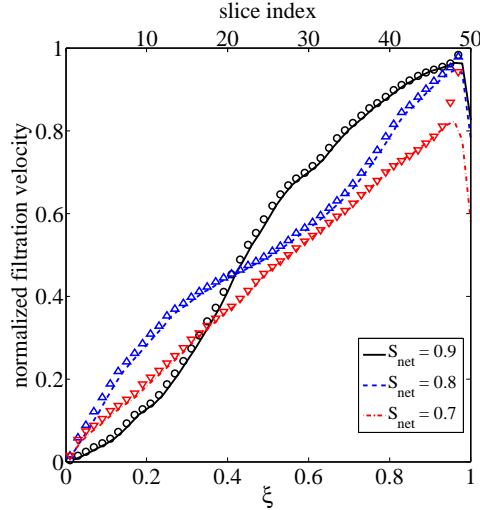
Figure 5.15: Normalized velocity profiles in the capillary-dominated regime obtained from time-averaging of single invasion velocity profiles over all realizations (lines) and from mass conservation law (symbols) for three different network saturations. The velocities are normalized by $J/(A\rho_\ell)$, where J is the evaporation rate corresponding to each overall saturation.

normalized filtration velocity values of the continuum approach at the very top of the network is owing to the evaporation at those positions. In fact the change of saturation considered in Eq. 5.5 is only due to the liquid transport. However, evaporation at the top of the network leads to adding an extra ΔS, which is not due to the liquid transport, and therefore the velocity values at these positions are overestimated.

The change of velocity at different depths of the network is also shown in Fig. 5.16. At the beginning of the drying process ($S_{net} = 1$), the velocity is zero everywhere. When drying starts, gas invades into the network. As soon as the gas reaches to a certain depth of the network, the liquid is pumped to the surface and therefore the liquid velocity at that position will become non-zero. As expected, the velocity of the positions near the surface is always bigger than deeper parts, since they transfer all the liquid being pumped from deeper positions to the surface. When the phase distribution is developed and becomes uniform everywhere, a constant velocity profile versus saturation is expected which lasts until the continuity of the liquid phase is lost and velocity decreases to zero. This is consistent with Eq. 5.5, in which uniform saturation profiles and a perfect CRP would result in a constant filtration velocity for each position in the network. Obviously this constant liquid velocity profiles are not observed in our results (Fig. 5.16). This is due to the non-uniformity of saturation profiles and decreasing evaporation rate during the "CRP".

A condition for obtaining almost perfectly linear averaged velocity profiles (as for the case $S_{net} = 0.7$ in Fig. 5.15) is that the histogram is quasi-uniform (equal probability in the distribution of moving menisci along the vertical coordinate). Consistently with the quasi-linear velocity profile obtained for $S_{net} = 0.7$, the histogram for this saturation in Fig. 5.12 is the one closest to a uniform probability distribution. We surmise that
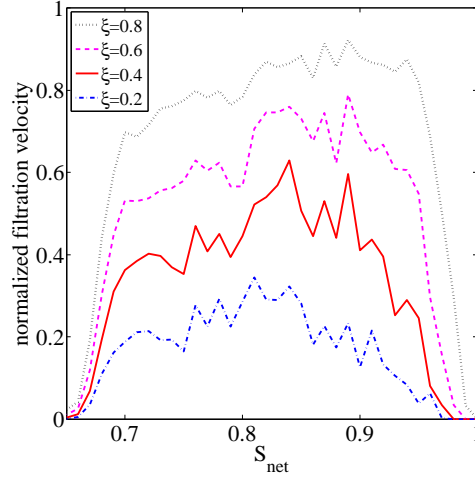
Figure 5.16: Normalized velocity profiles of capillary-dominated regime for different depths of the network versus network saturations, averaged among all realizations.

more uniform histograms would be obtained during the CRP/FRP by considering larger networks or a greater number of realizations. We also note that the case $S_{net} = 0.9$ is different since this saturation corresponds to the very first period before breakthrough, where the saturation profile is not uniform. Although it would be desirable to repeat the work considering larger networks, we believe that the results obtained from our relatively small network provide a clear and convincing interpretation of the velocity field when the liquid phase is connected to the top surface of porous medium (CRP and FRP) in the capillary regime.

One interesting outcome is that the velocity induced in the liquid phase as a result of the evaporation process essentially takes place in the main cluster. As illustrated in Fig. 5.17, a noticeable fraction of the liquid phase does not belong to the main cluster. Thus, there are liquid regions within the network completely inactive in terms of convective transport, suggesting that it would be interesting to clearly distinguish the main cluster from the other liquid clusters when analyzing the transport of dissolved species or particles during drying. This is in contrast to the classical continuum approach which uses a single variable (the saturation) to characterize the local presence of the liquid phase, without distinguishing between saturation corresponding to the main cluster and saturation associated with the other clusters. This suggests that it would be interesting to develop new continuum models making explicitly the distinction between the moving liquid phase and the liquid phase at rest.

5.5 Liquid velocity field in stabilized regimes

As it was mentioned earlier in this chapter, gravity and viscosity act as stabilizing mechanisms on the water transport in drying porous media. This means that the so-called pumping effect in capillary-dominated drying of a porous sample (see Fig. 5.3 and its
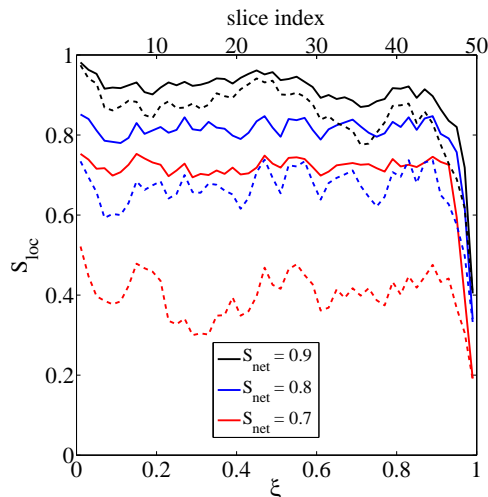
Figure 5.17: Saturation profiles for a single realization, considering all clusters and all isolated liquid throats (solid lines) and only the main cluster (dashed lines) for overall saturations 0.9, 0.8 and 0.7.

explanations), which leads to the free transport of water to the surface, will be hindered by the introduction of viscosity or gravity. Thus it is interesting to see how the liquid velocity profile in the presence of these stabilizing effects will be affected. For this purpose, a series of simulations on PN drying of gravity-capillary and viscous-capillary regimes were performed and their velocity fields were obtained by applying the continuum and discrete approaches. In order to be able to compare the results in this section with the capillary-dominated results, the velocity fields will be obtained for the same network saturations as in the capillary case, i.e. $S_{net} = 0.9$, 0.8 and 0.7.

5.5.1 Pore network drying simulations

In order to investigate the effect of gravity and viscosity on the velocity field, the same network size as for the capillary regime, i.e. $25 \times 25 \times 51$ nodes, was considered. The other geometrical characteristics as well as the operating conditions of this series of simulations can be found in Table 3.1. For the gravity-capillary simulations, two different values of the Bo number were considered: high Bo case with g $= 1.3$ m/s^2 and $Bo = 22 \times 10^{-3}$ (same simulations as Case 2 in Chapter 4) and low Bo case with g $= 0.13$ m/s^2 and $Bo = 22 \times 10^{-4}$. In the viscous-capillary simulations, the initial capillary number is Ca $= 0.014$ (same simulations as in Chapter 3). The Bo and Ca numbers are calculated from Eqs. 3.18 and 3.19, respectively. For each series of simulations, 15 realizations of throat radius distribution were considered.

Drying rate In Fig. 5.18 the normalized average drying rate curves of all series of simulations are shown. The parameters used for this series of simulations can be found in Appendix A. For the low Bo case, the effect of gravity is not strong enough and the evaporation rate decreases slightly. But when increasing g by 10 times, as in the high Bo

case, the effect of gravity becomes significant and therefore the evaporation rate decreases sharply at the beginning of the process. The drying rate curve of the viscous case also suggests that the viscous effect is big and has a significant stabilizing influence.

In contrast to the capillary-dominated regime, in stabilized regimes the CRP is not observed. This is obviously due to the added resistance to the liquid pumping, which consequently reduces the liquid flow towards the evaporative surface.
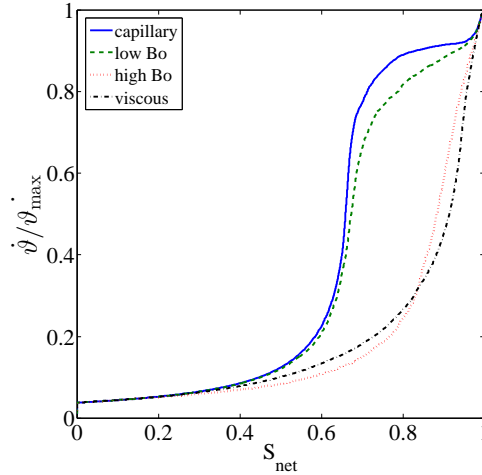
Figure 5.18: The normalized evaporation rate of different regimes, each averaged among 15 realizations.

Horizontal slice-averaged saturation profiles The slice-averaged saturation profiles for the low Bo pore network drying simulations are shown in Fig. 5.19a. Since the effect of gravity is not big, the saturation profiles differ only slightly from the ones in the capillary-dominated regime. The edge effect which was explained in Section 5.4.1 is also seen in this case, i.e. the sharp drop of the saturation profile at the very top of the network is due to the emptying of top vertical menisci. The saturation profiles of the PN drying simulations for high Bo are shown in Fig. 5.19b. Here the strong effect of gravity significantly hinders the transport of water to the surface. As a result, an almost dry region is observed even at high network saturations (around $S_{net} = 0.9$). This shows that liquid is not forming a continuous phase across the whole network and that evaporation happens inside the network. Consequently, a sharp drop in evaporation rate at high network saturations (Fig. 5.18) is observed. The stabilizing effect of gravity also affects the evolution of saturation at the lower end of the network. As it is seen in Fig. 5.19b, the saturation stays very high until small values of S_{net} which is a sign of very small capillary potential for local saturations close to 1 (for explanation of the capillary potential concept see Eq. 2.1). In fact, it is more difficult for the gas phase to invade the menisci which are located in the high local saturation region. The saturation profiles of viscous drying simulations (Fig. 5.19c) show for the near-surface region the same behavior as in the high Bo case, i.e. the liquid loses its continuity at the top of the network at high S_{net}. As a consequence, the gas phase can easily invade into the liquid throats in this region, forming a dry zone

at the top and reducing the total evaporation rate with a sharp slope.

The important note here is that because of the non-uniform saturation profiles (for $S_{net} >$ 0.7) and the absence of the CRP in stabilized regimes, it is not possible to combine Eq. 5.2 with Eq. 5.1 in order to obtain a general relationship for the velocity field. However, it is possible to predict and characterize the behavior of the velocity profiles for such regimes. In order to do so, the same concepts as in the capillary dominated-regime will be used: here single invasions are responsible for creating a velocity field on the pore scale, whereas on the continuum-scale the change of slice-averaged saturation profiles in the non-evaporative region is an indication of non-zero velocity field during the drying of a porous sample.

(a)

(b)

(c)
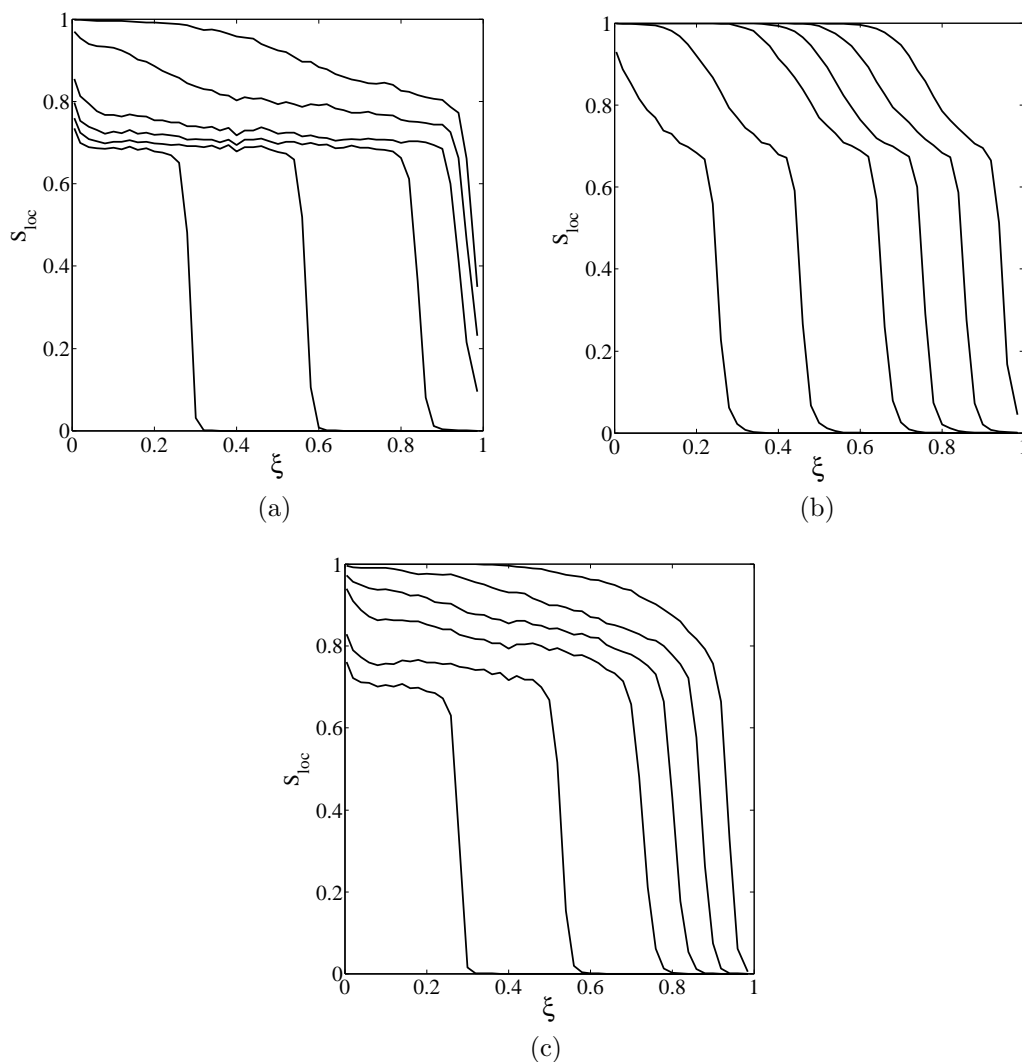
Figure 5.19: Saturation profiles of (a) low Bo (b) high Bo and (c) viscous PN drying simulations, averaged among 15 realizations. From the top, profiles belong to network saturations 0.9, 0.8, 0.7, 0.6, 0.4 and 0.2, respectively; $\xi = z/H$. The evaporative top surface of the network is located at $\xi = 1$.

5.5.2 Slice-averaged velocity profiles

In the presence of gravity, at each time step only one meniscus is emptied. Therefore, the slice-averaged velocity profile of a single invasion in the gravity-capillary regime can be obtained by applying the same procedure used in the capillary-dominated regime as follows:

1. At each time step the moving meniscus, which has the largest capillary potential, is identified (Eq. 2.1).

2. By introducing a "pseudo-viscosity", the mass conservation equation for each liquid pore is written (summation of liquid flow rates to a liquid pore, obtained from Hagen-Poiseuille's equation, should be zero).

3. The boundary condition for all menisci, except the moving meniscus, is their respective evaporation rate.

4. After obtaining the liquid pressure field, by summing up the liquid flow rates for all vertically-neighboring pores in a slice (a slice is shown in Fig. 5.4) and dividing the sum by $\rho_\ell A$, the averaged velocity for each slice is obtained.

The shape of an instantaneous velocity profile in the gravity-capillary drying of a porous sample is the same as in the capillary-dominated regime, i.e. a step change in velocity field that happens at the position of the meniscus with the largest capillary potential (see Fig. 5.11). However, the magnitude of the acceleration of gravity defines which meniscus should be invaded. According to Eq. 2.1, in case g is big, the gravity term $(\rho_\ell - \rho_a)gh$ will become more important. This means that menisci located at higher positions (bigger h) will have greater capillary potential and are more likely to be invaded. Therefore, if the gravity effect is significant, as in the high Bo case, it is expected to have more invasions at higher positions in the network compared to the case with lower gravity effect.

However, in the case of viscosity not being negligible, it could happen that at the same time more than one menisci are emptying. This is because of the effect of viscosity which acts as a barrier to the free transport of water from the largest meniscus to the other evaporative menisci, making some other evaporative menisci to move. Therefore a pressure will be inserted into the bulk of the liquid phase at different positions in the network, which causes fluctuations in the step-wise velocity profile seen in the absence of viscosity. In Fig. 5.20, as an example, an instantaneous velocity profile obtained at network saturation 0.9 for the viscous-capillary drying of the network with $25 \times 25 \times 51$ nodes is shown.

As seen in Fig. 5.20, there are several step changes in the instantaneous velocity profile. In fact, each of these jumps shows an external push on the liquid phase, imposed by a
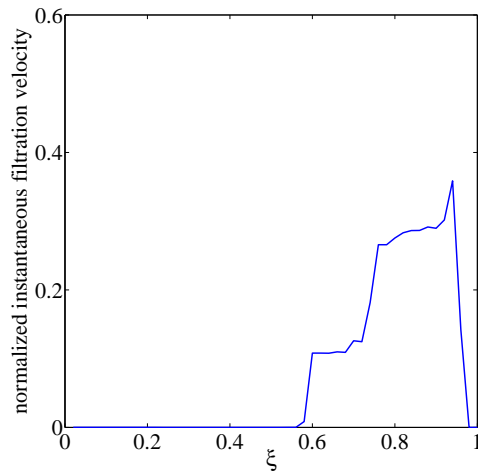
Figure 5.20: Instantaneous velocity profile obtained from PN drying simulation for the viscous-capillary regime at network saturation 0.9. The velocity profile has been normalized by dividing it over its respective evaporation rate.

moving meniscus. In other words, the pressure induced by the moving meniscus located at the lowest position in the network ($\xi \approx 0.6$) is not enough to keep the other menisci stationary. This leads to retreating of water in some other menisci, located at higher positions and a slice-averaged velocity profile with several step changes. However, if the size of the moving meniscus is large enough, the imposed pressure might be big enough to avoid any water retreatment in other menisci, which would cause a similar slice-averaged instantaneous velocity field as in the gravity-capillary or capillary-dominated regimes to be observed.

The method for calculation of slice-averaged velocity profiles in the viscous-capillary regime is similar to the capillary-dominated and gravity-capillary regimes. The only difference is that here there is no need to introduce a viscosity to be able to write the mass conservation (step 2 above), because obviously viscosity has already been introduced in PN drying simulations.

5.5.3 Reconciling the continuum and discrete velocity fields

As it was seen in Fig. 5.19, in the presence of gravity or viscosity the slice-averaged saturation profiles are not uniform. Neither a constant rate period is observed in such regimes (Fig. 5.18). Due to these differences, in stabilized regimes the velocity field does not follow a predictable behavior and is a function of Ca and Bo. Here, the velocity profiles in presence of viscosity and gravity are calculated from the mass conservation method using Eq. 5.10.

As it was mentioned in Section 5.4.4, the filtration velocity of the continuum approach can be interpreted as a time-averaged velocity of the PN approach. To reconcile the results of the two approaches, the same procedure as for the capillary-dominated regime is taken,

as follows:

1. At each desired overall saturation, the interval between $S_{net} - 0.05$ and $S_{net} + 0.05$ is considered.

2. The velocity profiles for the continuum approach are obtained by using Eq. 5.10. ΔS in this equation is the change of saturation at each slice between the interval $S_{net} - 0.05$ and $S_{net} + 0.05$.

3. The velocity profiles for the PN approach are obtained by averaging instantaneous slice-averaged velocity profiles for all the steps in the period between $S_{net} - 0.05$ and $S_{net} + 0.05$ among all realizations.

Next, the velocity profiles of stabilized regimes obtained from these two methods are presented and discussed. In order to focus only on the velocity of the liquid phase, the results will be shown only for the region in which the evaporation is zero.

Velocity profiles in low Bo regime The liquid velocity profiles of the low Bo regime obtained from mass conservation and PNM are shown in Fig. 5.21. A good agreement between the results of both methods is observed. Because of the weak effect of gravity in this case, at each network saturation, a similar distribution of moving menisci across the network compared to the capillary-dominated regime is expected. As a result, the time-averaged velocity profiles do not deviate significantly from the ones in the capillary-dominated regime, as seen in Fig. 5.21.
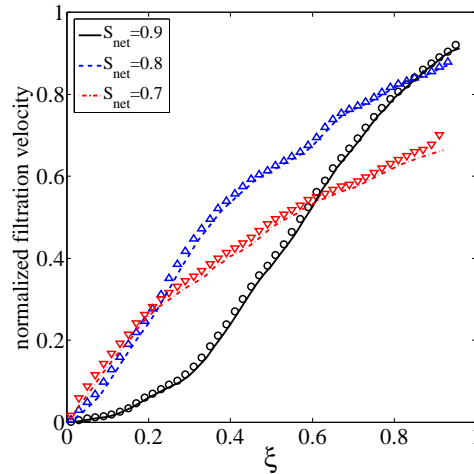
Figure 5.21: Normalized velocity profiles in the gravity-capillary regime (low Bo) obtained from time-averaging of the single step invasion velocity profiles over all realizations (lines) and from mass conservation law (symbols) for three different network saturations. The velocities are normalized by $J/(A\rho_\ell)$, where J is the evaporation rate corresponding to each overall saturation.

Velocity profiles in high Bo regime When the acceleration of gravity is big, it is expected to see more deviation from the liquid velocity profiles of the capillary-dominated regime. In fact, gravity in this case is so large that at high local saturations it does not let the gas invade easily into deeper positions of the network. The normalized slice-averaged instantaneous velocity profiles of one realization as well as the normalized time-averaged velocity profile averaged among all realizations in high Bo regime are shown in Fig. 5.22. The instantaneous velocity profiles at different network saturations show that, when Bo is big enough, the invasions will happen at higher positions in the sample and therefore the two-phase zone will be smaller compared to the capillary-dominated regime. It is also observed in this figure that, the liquid velocity profiles do not continue until the top of the network, which is owing to the fast receding of the two-phase region into the network. Another interesting point here is that, at all network saturations, no invasion happens in a big part of the network (lower end of the network), which leads to the creation of a zero-velocity region. For each network saturation, the zero-velocity area corresponds to the region in which $S_{loc} = 1$.

The normalized time-averaged velocity profiles obtained from PN simulations are compared to the ones obtained from the continuum approach in Fig. 5.23. There is a good agreement between the results of the two methods for all network saturations. By reducing network saturation from 0.9 to 0.8, the maximum value of normalized filtration velocity is reduced significantly. This is because at $S_{net} = 0.9$ the two-phase region is still attached to the surface (see saturation profiles in Fig. 5.19b) and, therefore, not fully developed. As soon as a dry region has been formed inside the network (for $S_{net} < 0.8$), it is expected that by further reducing the network saturation until S_{BT} the phase distribution of the two-phase region will stay constant (owing to constant Bo) and, consequently, the shape and maximum of the normalized filtration velocity profiles will remain unchanged while moving inside the depth of the network. This is observed by comparing the normalized velocity profiles for $S_{net} = 0.8$ and $S_{net} = 0.7$ in Fig. 5.19b.

Velocity profiles in viscous regime The normalized filtration velocity profiles for the viscous simulations obtained from the PN and continuum models are shown in Fig. 5.24. Same as the capillary-dominated and gravity-capillary results, here also the agreement between the velocity profiles of the two methods is fairly good. At $S_{net} = 0.9$, a zero-velocity region is observed, which is a sign of full saturation before the BT has happened. After the BT point, i.e. for $S_{net} < 0.9$, the liquid velocity near the bottom of the network is non-zero. An almost linear velocity profile for network saturations smaller than S_{BT} suggests that the distribution of moving menisci across the network is uniform, which is similar to the velocity profiles of the capillary-dominated regime at $S_{net} = 0.7$ (Fig. 5.12c).

(a)

(b)

(c)
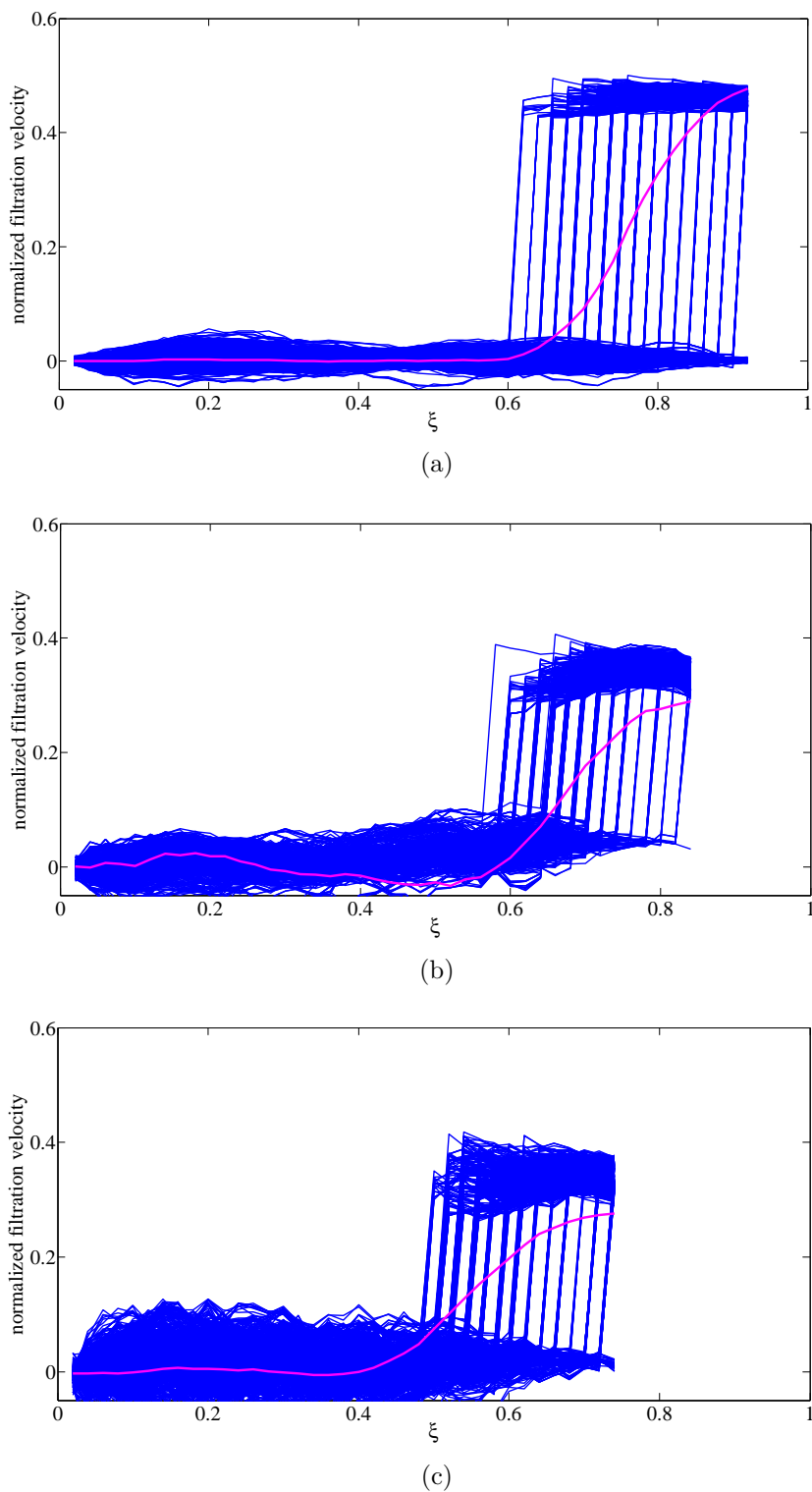
Figure 5.22: Normalized velocity profiles in gravity-capillary regime with high Bo induced by several single invasions (blue lines) for network saturations (a) 0.9, (b) 0.8 and (c) 0.7 obtained from PN simulation for one realization. The average velocity profile for all invasions and realizations is also shown in purple.

The comparison between the velocity profiles of all regimes at different network saturations is brought in Fig. 5.25. An interesting point observed in this figure is that the normalized filtration velocity of the capillary-dominated regime is always bigger than that of the stabilized regimes, neglecting some areas in which the velocity of the low Bo case is
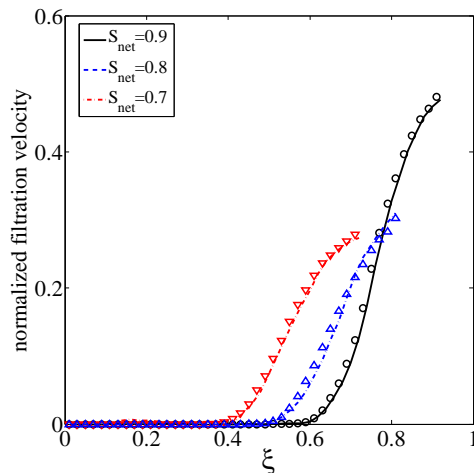
Figure 5.23: Normalized velocity profiles in the gravity-capillary regime (high Bo) obtained from time-averaging of single invasion velocity profiles over all realizations (lines) and from mass conservation law (symbols) for three different network saturations. The velocities are normalized by $J/(A\rho_\ell)$, where J is the evaporation rate corresponding to each overall saturation.
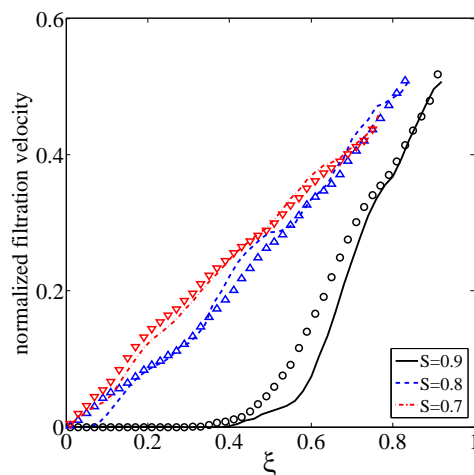
Figure 5.24: Normalized velocity profiles in the viscous-capillary regime obtained from time-averaging of single invasion velocity profiles over all realizations (lines) and from mass conservation law (symbols) for three different network saturations. The velocities are normalized by $J/(A\rho_\ell)$, where J is the evaporation rate corresponding to each overall saturation.

bigger than the velocity of the capillary-dominated regime, which could be due to the small number of realizations. The higher filtration velocity in the capillary-dominated regime is due to the fact that in this case the main cluster places a significant portion of the liquid at the top of the two-phase region (see Fig. 5.17) where evaporation happens. Therefore, a large part of the evaporation rate comes from the main cluster. This imposes a liquid pressure and velocity field inside the main cluster, corresponding to the evaporation rate from the main cluster. However, in strongly stabilized regimes, e.g. the high Bo and viscous cases, the fragmentation of the liquid phase at the top of the two-phase region is significant and many isolated menisci are formed in this region. This consequently leads to less contribution of the bigger clusters to the total evaporation rate. As a result, the imposed pressure in the main liquid cluster is less, which leads to a smaller normalized filtration velocity in such regimes.
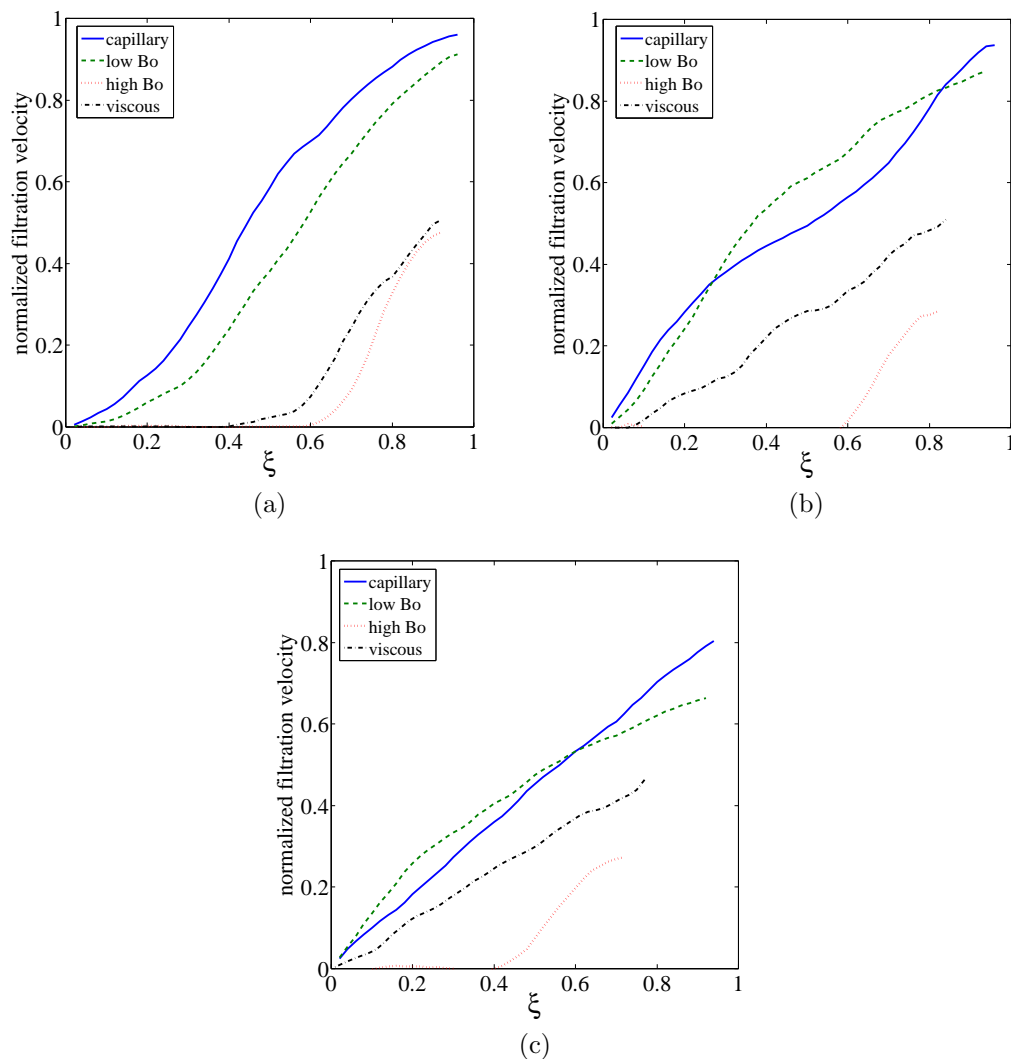
Figure 5.25: Normalized velocity profiles of all regimes obtained from time-averaging of the PN single invasion velocity profiles over all realizations for network saturations 0.9 (a), 0.8 (b) and 0.7 (c).

The ability of PNM and continuum approach to predict the behavior and characteristics of filtration velocity profiles in the presence of stabilizing regimes proves that these two methods are well-suited for prediction of velocity profiles of different regimes. However, it would be interesting to develop a general form of velocity profile for the viscous-capillary and gravity-capillary regimes, based on Ca and Bo, respectively.

5.6   Remarks

In this chapter the structure of the velocity field in the liquid phase during the drying of a porous medium for different regimes was studied. A simple mass balance in the continuum framework enabled to extract the variation of velocity across the sample. By contrast the instantaneous slice averaged velocity field determined from pore network simulations showed a different behavior along the porous medium height. It was shown

that the continuum and pore network standpoints can be reconciled by time averaging the velocity field obtained from the pore network simulations.

The main result in this chapter was that the velocity predicted from the classical continuum approach can be interpreted as a temporally and spatially averaged velocity. While it is traditional to consider the continuum (Darcy)-scale velocity as a spatial average, i.e.Whitaker [1998], it is less common to combine spatial and temporal averaging to obtain upscaled descriptions. This is done, for example, in the upscaling of turbulent flows in porous media, e.g. de Lemos [2012]. In the case of two-phase flow, the formal upscaling, e.g. Whitaker [1986], is typically performed assuming quasi-static distributions of the fluids at the REV scale without any time-averaging procedure since all menisci are actually considered as static. In this context, our results suggest that the classical Darcy-scale equations used to describe the drying process in the capillary regime could be rigorously derived combining space and time averages.

Although the analysis leads to consistent results (except in the edge effect region) between the classical continuum approach and the PN simulations as far as the (averaged) velocity field is concerned, the (instantaneous) velocity field is probably still more complex. For instance, we argue that the Haines jumps have little impact on the liquid-gas distributions within the pore space, which essentially corresponds to quasi-static distributions. However, it is unclear whether the Haines jumps have an impact on the convective transport of a species.

In extraction of velocity profiles we have not taken into account the possible presence of liquid films. It is relatively well established that liquid films can have a great impact on the drying process, e.g. Chauvet et al. [2009], Yiotis et al. [2012]. This actually depends on the wettability properties of the three phases, Prat [2007]: The lower the contact angle is, the more likely films will have a significant impact. However, based on the existing PN models of drying with films, e.g. Prat [2007], Vorhauer et al. [2015], Yiotis et al. [2003], the presence of films should not change the main results presented in this chapter except that the CRP in the capillary-dominated regime computed with the PNM would be longer when liquid films are added to the model.

Our results also suggest that one of the key issues in the modeling and analysis of drying is the edge effect region. Since drying is controlled by what happens at the surface during the CRP/FRP, this region is of key importance. The consequence for the modeling of drying within the continuum framework would be to develop a specific modeling for this region so as to take into account adequately the impact of this region on evaporation. It is well known that the interfacial region between a porous medium and a free fluid deserves special attention in the somewhat simpler cases where there is a single fluid and no phase change, e.g. Chandesris and Jamet [2009], Ochoa-Tapia and Whitaker [1995]. In that respect, it makes sense that this must also be the case for the significantly more

complex drying situation.

Finally, our results also open up a route for better analysis of the transport of species (ions, particles) that can be present in the liquid phase during drying owing to the fundamentally different structure of the instantaneous spatially averaged velocity field compared to the velocity field obtained from the continuum model. In this respect, it would be interesting to compare pore network simulations and continuum model-based predictions in the same spirit as the velocity field analysis presented here. Also, our results suggest that making a clear distinction between the convective active liquid phase (corresponding to the main cluster) and the non-active liquid phase (corresponding to the isolated liquid clusters) could be instrumental for developing better species transport models.

Chapter 6

Summary and outlook

6.1 Summary

In this work, the pore-scale and continuum phenomena during drying of capillary porous media was investigated. With the help of pore network drying simulations, it was tried to predict and analyze the macroscopic phenomena happening at the surface and inside the porous medium during drying. These phenomena were the moisture transport inside the porous medium, the local equilibrium at the surface and inside the network, the drying rate and the liquid velocity profiles.

The one-equation continuum model of drying, in which all the dependent variables are a function of saturation, was used to predict the kinetics and slice-averaged saturation profiles of the drying process in viscous-capillary regime in a pore network with $25 \times 25 \times 51$ nodes. In order to solve this equation, the dependency of three macroscopic parameters, namely, the moisture transport coefficient, the NLE function at the surface and the NLE function inside the network on saturation should be known a priori. These parameters were extracted by using the PN simulations on multiple realizations of the throat size distribution.

By calculating the mean vapor pressure and saturation of a slice the NLE function inside the porous medium was obtained. By applying the same procedure, this time for the surface, the relationship between NLE function at the surface and surface saturation was extracted. As an interesting and new finding, it was proved that the LE assumption which has been considered in classical continuum models of drying of capillary porous media may not be always valid. It was also shown that the NLE function at the surface is different from the one inside the network. The existence of NLE effects is a strong indication that the one-equation continuum model is intrinsically not suited for our problem.

The moisture transport coefficient has two parts, one of which is responsible for the transport of water in the liquid and the other in the gas phase. The summation of these two quantities at each local saturation gives the total value of moisture transport coefficient.

The functionality of D versus S_{loc} was determined by three methods. In the first method, which was developed in this work for the first time, the water flux in the gas and liquid phase inside a slice (REV) as well as the slice-averaged saturation profiles obtained from PN drying simulations were used to obtain the moisture transport coefficient in both phases. Here, a slice was considered to contain two rows of pores. The moisture transport coefficient was also obtained by a second method, the inverse method, which was developed by integrating the one-equation continuum model over space. In this method the only data used were the slice-averaged saturation profiles of PN drying simulations. As the third method of extraction of the moisture transport coefficient, capillary-controlled invasion percolation simulations were performed, assuming the local capillary equilibrium in a REV of size $25 \times 25 \times 25$ nodes. By performing the capillary-controlled IP simulations, three effective parameters, i.e. capillary pressure, relative permeability and relative diffusivity, were specified as functions of local saturation. Then, by using Eq. 3.12, the moisture transport coefficient was obtained.

The moisture transport coefficient results obtained from the first method were the most reliable, since they could better show the physics of the drying process for the most complete range of local saturations. It was proved that the moisture transport coefficient not only is a function of local saturation, but also changes as the network saturation varies (for $S_{net} <\sim 0.68$). At a certain S_{loc}, with decreasing S_{net}, the value of D was reduced. It was shown that the reason for this phenomenon is the increased ratio of isolated menisci with decreasing network saturation. The D-S curve was in general in agreement with experimental results, i.e. it had two maxima at opposing local saturation limits, which is the sign of highest moisture transport in single-phase regions, and a minimum at $S_{loc} \approx 0.4$, which showed that the moisture transport is highly resisted at this saturation.

The inverse method produced D values in agreement with the first method at high S_{net}, however overestimated the D values at low S_{net}. This was due to the fact that the effect of isolated menisci, which mainly act as a barrier to the transport of moisture, cannot be considered in this method. The capillary-controlled IP simulations produced D values only until the irreducible saturation since at this saturation the conductivity of the liquid phase inside the REV is lost and capillary-controlled IP cannot continue. The capillary-controlled IP simulations overestimated the moisture transport coefficient. This was owing to the large size of the REV considered in capillary-controlled IP compared to the network size. However the trends in the change of moisture transport coefficient obtained from capillary-controlled IP were in agreement with those from the first method.

Since the saturation of a slice and consequently macroscopic parameters could be captured only until a specific value ($S_{loc} \approx 2 \times 10^{-4}$), a method was developed to predict the values of moisture transport coefficient until $S_{loc} = 0$. After fitting curves on the data points of macroscopic parameters, they were fed into the one-equation continuum model. The CM

could predict the saturation profiles and evaporation rate (until $S_{net} \approx 0.85$) of the drying process, which were in agreement with the averaged PN drying simulation results. This was a proof that the macroscopic parameters were correctly identified by the methods considered in this work.

In order to see how the macroscopic parameters change with network size and due to the high computational time of PN drying simulations in the viscous-capillary regime, gravity-capillary simulations were performed. It was shown that for a not too high network, the gravity-capillary simulations can predict the macroscopic parameters obtained from viscous-capillary simulations, provided that Bo is in the same range as the initial value of Ca. The PN drying simulations of the gravity-capillary regime were performed for networks of $50 \times 50 \times 51$ and $100 \times 100 \times 101$ nodes. It was then claimed that, because of similarity of macroscopic parameters for all the studied network sizes, the network of $25 \times 25 \times 51$ nodes is the representative network for all network sizes smaller than $100 \times 100 \times 101$ nodes.

With the help of the detailed information provided by PN drying simulations, e.g. the phase distribution and vapor pressure of gas pores at the surface, the behavior of φ_{surf} and the contribution of wet and dry patches on the surface to the total evaporation rate were analyzed by changing the Bo number, throat length and boundary layer thickness. In all the cases, the non-local equilibrium effect at the surface was observed. It was concluded that the change of regime, provided that capillarity is not negligible, has barely an effect on the NLE function at the surface. Keeping the throat radius constant, it was shown that the non-local equilibrium effect is more pronounced for a larger throat length. Finally a thinner boundary layer resulted in a more significant non-equilibrium effect. Among all the three changes considered, only the change of throat length affected the relative contributions of wet and dry regions on the surface to the total evaporation rate.

The PN drying simulations in capillary-dominated regime showed that in the CRP a sharp drop is observed in slice-averaged saturation profiles at the top of the network, which is not considered in classical continuum models of drying. This edge effect was characterized by computing the water flow rates in main and isolated clusters, isolated menisci and gas phase. It was then shown that the occurrence of this effect is due to the creation of many isolated menisci at the top of the network, which consequently leads to a sharp drop in evaporation rate at the beginning of the "CRP".

The liquid transport inside the porous medium during the CRP in the capillary-dominated regime was further investigated by the analysis of liquid velocity field. A mass conservation approach suggested that the filtration velocity field is a linear function of depth. However the instantaneous velocity profile induced by a single invasion and obtained from PNM showed a step change of velocity in a certain depth. In order to reconcile the PNM and continuum velocity profiles the instantaneous velocity profiles of PNM were averaged over

a period of time. In this way, interestingly the classical Darcy-scale equations for drying in the capillary-dominated regime were deduced by taking spatio-temporal averages. It was also proven that a linear velocity profile in the capillary-dominated regime is obtained only if the histogram of position of moving menisci during a time interval is uniform.

The continuum and PNM liquid velocity fields inside the porous medium during drying in stabilized regimes were also investigated. While the instantaneous velocity profiles in gravity-capillary simulations were similar to the ones in capillary regime, they were fluctuating in the viscous-capillary simulations. In case of a strong stabilization effect, a zero-velocity region could be observed at the bottom end of the sample. Also due to the early formation of a dry region inside the network, the liquid will not span across the whole network, making the liquid velocity profile shorter. To reconcile the continuum and PNM velocity profiles, same as in the capillary-dominated regime, the single invasion velocity profiles were averaged over a period of time. The comparison between the velocity profiles of capillary-dominated and stabilized regimes showed that at each network saturation the velocity in the former is always bigger, owing to the absence of any resistance against the liquid pumping from the instable meniscus (menisci) towards stationary menisci.

6.2   Outlook

The pore network considered in this work was a regular cubic network. Although through randomness of the throat size distribution and also Monte Carlo simulations its results can be considered reliable, in order to simulate real samples some modifications should be done. The inclusion of pore volume is one of these modifications. In the current pore network model, the pores are only computational nodes. The inclusion of pore volume would be more consistent with real systems, since the majority of liquid in a porous sample is stored in pores. It would also help to achieve a smaller S_{irr}, which would consequently lead to a longer CRP in the capillary-dominated regime and let the capillary-controlled IP simulations continue to smaller local saturations.

An important finding in this work was the non-equilibrium effect in drying of capillary porous media. However, it is not yet clear how this phenomenon is affected in presence of secondary capillary structures. It is also not known how such structures affect the moisture transport coefficient and the liquid velocity field. Therefore, it would be very interesting to include secondary capillary structures in the pore network model to investigate their effect on both quantities.

The size of the REV in our capillary-controlled IP simulations was determined to be $25 \times 25 \times 25$ nodes, i.e. only $1/2$ of the network of $25 \times 25 \times 51$ nodes. Therefore the length scale separation criterion, which is a requirement for CM, is violated here. Thus, the network size in PN drying simulations should be increased, so that to meet the length

scale separation criterion. Increasing the network size is also advantageous from the point of view that it can lead to producing the macroscopic parameters of CM for bigger sample sizes. However, this is not possible with the current facilities owing to the high computational cost of PN drying simulations. An alternative is to predict the macroscopic parameters of big sample sizes through study of the change of macroscopic parameters with network size. The maximum network size, for which the PN drying simulations were performed, was $100 \times 100 \times 101$ nodes and took almost 100 days for one realization in the gravity-capillary regime. Therefore, it is necessary to either optimize the drying code or use strong workstations, so that to be able to increase the network size and number of realizations in Monte Carlo PN drying simulations. The pore networks considered here were neither shallow nor narrow. Therefore, it would be interesting to investigate the macroscopic parameters and liquid velocity fields also in such networks.

Although the one-equation continuum model produced saturation profiles in agreement with the PN drying simulations, it failed to predict the evaporation rate until the end of the process. Moreover, three functions for the moisture transport coefficient were used, which makes it difficult to apply such a model. More importantly, the presence of the non-equilibrium effect showed that the application of the one-equation CM is intrinsically not suitable to our system. Development of a two-equation CM, in which mass conservation equations of gas and liquid are treated separately, seems to solve the deficits of the one-equation CM. In contrast to the one-equation CM, in such model it is not needed to introduce a relationship between saturation and vapor pressure (the NLE function). Also the problem regarding the extraction of moisture transport values at very low local saturations, which was solved in this work by the help of the evaporation rate and mass conservation law, will be eliminated in the two-equation continuum model.

A more advanced version of the two-equation continuum model would take into account the contribution of main and isolated liquid clusters as well as isolated menisci to the total liquid transport. As it was seen in this work, the liquid is mainly transported through the main cluster towards the evaporative surface. Therefore, it is important to distinguish between the moving liquid and the liquid at rest inside the porous medium. This will enable to better analyze the transport of species in a drying porous sample.

Another important result was the characterization of the edge effect during drying of porous media, which leads to a sharp drop of saturation in the region near the evaporative surface and a sudden drop of evaporation rate at the beginning of the "CRP". PN drying simulations as well as experimental results show that this effect is intrinsic to the drying of porous media. However, in the classical continuum models of drying, the edge effect has not yet been considered and therefore this effect cannot be captured by such models. Thus, the inclusion of this phenomenon in the continuum model would certainly make its results more realistic.

Bibliography

A. W. Adamson and A. P. Gast. *Physical Chemistry of Surfaces*. Wiley, 6th edition, 1997.

T. Agaesse, A. Lamibrac, F. N. Büchi, J. Pauchet, and M. Prat. Validation of pore network simulations of ex-situ water distributions in a gas diffusion layer of proton exchange membrane fuel cells with x-ray tomographic images. *Journal of Power Sources*, 331: 462–474, 2016.

P. E. Arce, M. Quintard, and S. Whitaker. *The Art and Science of Upscaling*, pages 1–39. Wiley, 2005.

R. T. Armstrong and S. Berg. Interfacial velocities and capillary pressure gradients during Haines jumps. *Physical Review E*, 88:043010, 2013.

A. Attari Moghaddam, A. Kharaghani, E. Tsotsas, and M. Prat. Kinematics in a slowly drying porous medium: Reconciliation of pore network simulations and continuum modeling. *Physics of Fluids*, 29(2):022102, 2017a.

A. Attari Moghaddam, M. Prat, E. Tsotsas, and A. Kharaghani. Drying of capillary porous media in the piston-like invasion limit. evidence of non-local equilibrium effects. *To be submitted*, 2017b.

A. Attari Moghaddam, M. Prat, E. Tsotsas, and A. Kharaghani. A pore network study of evaporation from the surface of a drying non-hygroscopic porous medium. *To be submitted*, 2017c.

J. Benet and P. Jouanna. Non equilibre thermodynamique dans les milieux poreux non satures avec changement de phase. *International Journal of Heat and Mass Transfer*, 26(11):1585–1595, 1983.

S. A. Bories. Fundamentals of drying of capillary-porous bodies. In S. Kakaç, B. Kilkiş, F. A. Kulacki, and F. Arinç, editors, *Convective Heat and Mass Transfer in Porous Media*, pages 391–434. Springer Netherlands, 1991.

W. Brutsaert. *Evaporation into the Atmosphere: Theory, History and Applications*. Springer, 1982.

T. Bultreys, W. D. Boever, and V. Cnudde. Imaging and image-based fluid transport modeling at the pore scale in geological materials: A practical introduction to the current state-of-the-art. *Earth-Science Reviews*, 155:93–128, 2016.

F. P. Casciatori, A. Bück, J. C. Thoméo, and E. Tsotsas. Two-phase and two-dimensional model describing heat and water transfer during solid-state fermentation within a packed-bed bioreactor. *Chemical Engineering Journal*, 287:103–116, 2016.

N. H. Ceaglske and O. A. Hougen. Drying granular solids. *Industrial & Engineering Chemistry*, 29(7):805–813, 1937.

M. Chandesris and D. Jamet. Jump conditions and surface-excess quantities at a fluid/porous interface: A multi-scale approach. *Transport in Porous Media*, 78(3): 419–438, 2009.

F. Chauvet, P. Duru, S. Geoffroy, and M. Prat. Three periods of drying of a single square capillary tube. *Physical Review Letters*, 103:124502, 2009.

M. Cieplak and M. O. Robbins. Influence of contact angle on quasistatic fluid invasion of porous media. *Physical Review B*, 41:11508–11521, 1990.

P. Coussot. Scaling approach of the convective drying of a porous medium. *European Physical Journal B*, 15(3):557–566, 2000.

P. Crausse, G. Bacon, and S. Bories. Etude fondamentale des transferts couples chaleur-masse en milieu poreux. *International Journal of Heat and Mass Transfer*, 24(6):991 – 1004, 1981.

J.-F. Daian. *Equilibrium and Transfer in Porous Media 1: Equilibrium States*. Wiley, 2014.

M. de Lemos. *Turbulence in Porous Media*. Elsevier, 2012.

T. Defraeye. Advanced computational modelling for drying processes: A review. *Applied Energy*, 131:323–344, 2014.

J. Desarnaud, H. Derluyn, L. Molari, S. de Miranda, V. Cnudde, and N. Shahidzadeh. Drying of salt contaminated porous media: Effect of primary and secondary nucleation. *Journal of Applied Physics*, 118(11), 2015.

C. Duan, R. Karnik, M.-C. Lu, and A. Majumdar. Evaporation-induced cavitation in nanofluidic channels. *Proceedings of the National Academy of Sciences*, 109(10):3688–3693, 2012.

F. A. Dullien, C. Zarcone, I. F. Macdonald, A. Collins, and R. D. Bochard. The effects of surface roughness on the capillary pressure curves and the heights of capillary rise in glass bead packs. *Journal of Colloid and Interface Science*, 127(2):362–372, 1989.

H. Eloukabi, N. Sghaier, S. B. Nasrallah, and M. Prat. Experimental study of the effect of sodium chloride on drying of porous media: The crusty-patchy efflorescence transition. *International Journal of Heat and Mass Transfer*, 56(12):80–93, 2013.

I. Fatt. The network model of porous media. *Petroleum Transactions, AIME*, 207:144–181, 1956.

P. Faure and P. Coussot. Drying of a model soil. *Physical Review E*, 82:036303, 2010.

A. Ferrari and I. Lunati. Inertial effects during irreversible meniscus reconfiguration in angular pores. *Advances in Water Resources*, 74:1–13, 2014.

S. Geoffroy and M. Prat. A review of drying theory and modelling approaches. In J. M. P. Q. Delgado, editor, *Drying and Wetting of Building Materials and Components, Building Pathology and Rehabilitation*. Springer International, 2014.

I. Gómez, J. Sala, and J. Millán. Characterization of moisture transport properties for lightened clay brick: Comparison between two manufacturers. *Journal of Building Physics*, 31(2):179–194, 2007.

L. Guglielmini, A. Gontcharov, A. J. Aldykiewicz, and H. A. Stone. Drying of salt solutions in porous materials: Intermediate-time dynamics and efflorescence. *Physics of Fluids*, 20(7), 2008.

S. Gupta, H. P. Huinink, M. Prat, L. Pel, and K. Kopinga. Paradoxical drying of a fired-clay brick due to salt crystallization. *Chemical Engineering Science*, 109:204–211, 2014.

E. Haghighi, E. Shahraeeni, P. Lehmann, and D. Or. Evaporation rates across a convective air boundary layer are dominated by diffusion. *Water Resources Research*, 49(3):1602–1610, 2013.

F. Hidri, N. Sghaier, H. Eloukabi, M. Prat, and S. B. Nasrallah. Porous medium coffee ring effect and other factors affecting the first crystallisation time of sodium chloride at the surface of a drying porous medium. *Physics of Fluids*, 25(12), 2013.

C. K. Ho and K. K. Udell. An experimental investigation of air venting of volatile liquid hydrocarbon mixtures from homogeneous and heterogeneous porous media. *Journal of Contaminant Hydrology*, 11(3):291–316, 1992.

H. P. Huinink, L. Pel, and M. A. J. Michels. How ions distribute in a drying porous medium: A simple model. *Physics of Fluids*, 14(4):1389–1395, 2002.

M. Janz. *Methods of measuring the moisture diffusivity at high moisture levels.* Report tvbm-3076, Division of Building Materials, University of Lund, 1997.

M. Jung, M. Brinkmann, R. Seemann, T. Hiller, M. Sanchez de la Lama, and S. Herminghaus. Wettability controls slow immiscible displacement through local interfacial instabilities. *Physical Review Fluids*, 1:074202, 2016.

E. Keita, P. Faure, S. Rodts, and P. Coussot. MRI evidence for a receding-front effect in drying porous media. *Physical Review E*, 87:062303, 2013.

E. Keita, T. E. Kodger, P. Faure, S. Rodts, D. A. Weitz, and P. Coussot. Water retention against drying with soft-particle suspensions in porous media. *Physical Review E*, 94: 033104, 2016.

O. Krischer. *Die wissenschaftlichen Grundlagen der Trocknungstechnik.* Springer, 2013.

J. B. Laurindo and M. Prat. Numerical and experimental network study of evaporation in capillary porous media: Phase distributions. *Chemical Engineering Science*, 51(23): 5171–5185, 1996.

K. H. Le, A. Kharaghani, C. Kirsch, and E. Tsotsas. Pore network simulations of heat and mass transfer inside an unsaturated capillary porous wick in the dry-out regime. *Transport in Porous Media*, 114(3):623–648, 2016.

Y. Le Bray and M. Prat. Three-dimensional pore network simulation of drying in capillary porous media. *International Journal of Heat and Mass Transfer*, 42(22):4207–4224, 1999.

P. Lehmann and D. Or. Effect of wetness patchiness on evaporation dynamics from drying porous surfaces. *Water Resources Research*, 49(12):8250–8262, 2013.

P. Lehmann, S. Assouline, and D. Or. Characteristic lengths affecting evaporative drying of porous media. *Physical Review E*, 77:056309, 2008.

W. K. Lewis. The rate of drying of solid materials. *Industrial & Engineering Chemistry*, 13(5):427–432, 1921.

M. I. Lowry and C. T. Miller. Pore-scale modeling of nonwetting-phase residual in porous media. *Water Resources Research*, 31(3):455–473, 1995.

A. Luikov. Systems of differential equations of heat and mass transfer in capillary-porous bodies (review). *International Journal of Heat and Mass Transfer*, 18(1):1–14, 1975.

R. G. Marchand and M. K. Kumaran. Moisture diffusivity of cellulose insulation. *Journal of Building Physics*, 17(4):362–377, 1994.

E. F. Médici and J. S. Allen. Evaporation, two phase flow, and thermal transport in porous media with application to low-temperature fuel cells. *International Journal of Heat and Mass Transfer*, 65:779–788, 2013.

T. Metzger, A. Irawan, and E. Tsotsas. Influence of pore structure on drying kinetics: A pore network study. *AIChE Journal*, 53(12):3029–3041, 2007a.

T. Metzger, E. Tsotsas, and M. Prat. Pore-network models: A powerful tool to study drying at the pore level and understand the influence of structure on drying kinetics. In E. Tsotsas and A. S. Mujumdar, editors, *Modern Drying Technology: Computational Tools at Different Scales, Volume 1*, pages 57–102. Wiley-VCH, 2007b.

T. Metzger, T. H. Vu, A. Irawan, V. K. Surasani, and E. Tsotsas. Pore-scale modelling of transport phenomena in drying. In A. Bertram and J. Tomas, editors, *Micro-Macro-Interactions in Structured Media and Particle Systems*, pages 187–204. Springer, 2008.

A. S. Mujumdar, editor. *Handbook of Industrial Drying*. CRC Press, 4th edition, 2015.

D. A. Nield and A. Bejan. *Convection in Porous Media*. Springer, 3rd edition, 2006.

M. Norouzi Rad, N. Shokri, and M. Sahimi. Pore-scale dynamics of salt precipitation in drying porous media. *Physical Review E*, 88:032404, 2013.

S. Nowicki, H. Davis, and L. Scriven. Microscopic determination of transport parameters in drying porous media. *Drying Technology*, 10(4):925–946, 1992.

J. Ochoa-Tapia and S. Whitaker. Momentum transfer at the boundary between a porous medium and a homogeneous fluid: I. Theoretical development. *International Journal of Heat and Mass Transfer*, 38(14):2635–2646, 1995.

C. Peishi and D. C. Pei. A mathematical model of drying processes. *International Journal of Heat and Mass Transfer*, 32(2):297–310, 1989.

L. Pel, H. Brocken, and K. Kopinga. Determination of moisture diffusivity in porous media using moisture concentration profiles. *International Journal of Heat and Mass Transfer*, 39(6):1273–1280, 1996.

L. Pel, K. Landman, and E. Kaasschieter. Analytic solution for the non-linear drying problem. *International Journal of Heat and Mass Transfer*, 45(15):3173–3180, 2002.

P. Perré. Multiscale modeling of drying as a powerful extension of the macroscopic approach: Application to solid wood and biomass processing. *Drying Technology*, 28(8): 944–959, 2010.

J. R. Philip and D. A. de Vries. Moisture movement in porous materials under temperature gradients. *Eos, Transactions American Geophysical Union*, 38(2):222–232, 1957.

R. Pini and S. M. Benson. Simultaneous determination of capillary pressure and relative permeability curves from core-flooding experiments with various fluid pairs. *Water Resources Research*, 49(6):3516–3530, 2013.

M. Prat. Percolation model of drying under isothermal conditions in porous media. *International Journal of Multiphase Flow*, 19(4):691 – 704, 1993.

M. Prat. Discrete models of liquid-vapour phase change phenomena in porous media. *Revue Générale de Thermique*, 37(11):954–961, 1998.

M. Prat. Recent advances in pore-scale models for drying of porous media. *Chemical Engineering Journal*, 86(12):153–164, 2002.

M. Prat. On the influence of pore shape, contact angle and film flows on drying of capillary porous media. *International Journal of Heat and Mass Transfer*, 50(78):1455–1468, 2007.

M. Prat. Pore network models of drying, contact angle, and film flows. *Chemical Engineering Technology*, 34(7):1029–1038, 2011.

M. Prat, S. Veran-Tissoires, N. Vorhauer, T. Metzger, and E. Tsotsas. Fractal phase distribution and drying: Impact on two-phase zone scaling and drying time scale dependence. *Drying Technology*, 30(11-12):1129–1135, 2012.

A. Pujol, G. Debenest, S. Pommier, M. Quintard, and D. Chenu. Modeling composting processes with local equilibrium and local non-equilibrium approaches for water exchange terms. *Drying Technology*, 29(16):1941–1953, 2011.

H. Rajaram, L. A. Ferrand, and M. A. Celia. Prediction of relative permeabilities for unconsolidated soils using pore-scale network models. *Water Resources Research*, 33 (1):43–52, 1997.

S. Roels, J. Carmeliet, H. Hens, O. Adan, H. Brocken, R. Cerny, Z. Pavlik, A. T. Ellis, C. Hall, K. Kumaran, L. Pel, and R. Plagge. A comparison of different techniques to quantify moisture content profiles in porous building materials. *Journal of Thermal Envelope and Building Science*, 27(4):261–276, 2004.

M. Sahimi. *Continuum versus Discrete Models*, pages 1–7. Wiley-VCH, 2011.

E. Sanchez-Palencia. *Non-homogeneous media and vibration theory. Lecture Notes in Physics 127*. Springer, 1980.

E. Schlünder. On the mechanism of the constant drying rate period and its relevance to diffusion controlled catalytic gas phase reactions. *Chemical Engineering Science*, 43 (10):2685–2688, 1988.

W. Schoeber. *Regular regimes in sorption processes*. PhD thesis, Technical University Eindhoven, 1976.

H. Shibata and Y. Hirohashi. Effect of segment scale in a pore network of porous materials on drying periods. *Drying Technology*, 31(7):743–751, 2013.

N. Shokri and D. Or. What determines drying rates at the onset of diffusion controlled stage-2 evaporation from porous media? *Water Resources Research*, 47(9), 2011. W09513.

J. Srikiatden and J. S. Roberts. Moisture transfer in solid food materials: A review of mechanisms, models, and measurements. *International Journal of Food Properties*, 10 (4):739–777, 2007.

D. Stauffer and A. Aharony. *Introduction to Percolation Theory*. CRC Press, 2nd edition, 1994.

M. Suzuki and S. Maeda. On the mechanism of drying of granular beds. *Journal of Chemical Engineering of Japan*, 1(1):26–31, 1968.

D. S. Svirsky, M. I. J. Van Dijke, and K. S. Sorbie. Prediction of three-phase relative permeabilities using a pore-scale network model anchored to two-phase data. *SPE Reservoir Evaluation & Engineering*, 10(5):527–538, 2007.

J. Van Brakel. Mass transfer in convective drying. In A. Mujumdar, editor, *Advances in Drying*, pages 217–267. Hemisphere: New-York, 1980.

S. Veran-Tissoires and M. Prat. Evaporation of a sodium chloride solution from a saturated porous medium with efflorescence formation. *Journal of Fluid Mechanics*, 749: 701–749, 2014.

O. Vincent, D. A. Sessoms, E. J. Huber, J. Guioth, and A. D. Stroock. Drying by cavitation and poroelastic relaxations in porous media with macroscopic pores connected by nanoscale throats. *Physical Review Letters*, 113:134501, 2014.

N. Vorhauer, T. Metzger, and E. Tsotsas. Extraction of effective parameters for continuous drying model from discrete pore network model. *Proceedings of 17th International Drying Symposium, Magdeburg*, pages 415–422, 2010.

N. Vorhauer, Y. J. Wang, A. Kharaghani, E. Tsotsas, and M. Prat. Drying with formation of capillary rings in a model porous medium. *Transport in Porous Media*, 110(2):197–223, 2015.

T. H. Vu. *Influence of pore size distribution on drying behaviour of porous media by a continuous model*. Phd thesis, Otto von Guericke University Magdeburg, Germany, 2006.

T. H. Vu, T. Metzger, and E. Tsotsas. Influence of pore size distribution via effective parameters in a continuous drying model. *Proceedings of 15th International Drying Symposium, Budapest A*, pages 554–560, 2006.

Y. Wang, A. Kharaghani, T. Metzger, and E. Tsotsas. Pore network drying model for particle aggregates: Assessment by x-ray microtomography. *Drying Technology*, 30(15): 1800–1809, 2012.

S. Whitaker. Simultaneous heat, mass, and momentum transfer in porous media: A theory of drying. *Advances in Heat Transfer*, 13:119–203, 1977.

S. Whitaker. Flow in porous media II: The governing equations for immiscible, two-phase flow. *Transport in Porous Media*, 1(2):105–125, 1986.

S. Whitaker. *The Method of Volume Averaging.* Springer, 1998.

D. Wilkinson. Percolation effects in immiscible displacement. *Physical Review A*, 34: 1380–1391, 1986.

D. Wilkinson and J. Willemsen. Invasion percolation: A new form of percolation theory. *Journal of Physics A: Mathematical and General*, 16(14):3365–3376, 1983.

A. G. Yiotis, A. G. Boudouvis, A. K. Stubos, I. N. Tsimpanogiannis, and Y. C. Yortsos. Effect of liquid films on the isothermal drying of porous media. *Physical Review E*, 68: 037303, 2003.

A. G. Yiotis, I. N. Tsimpanogiannis, A. K. Stubos, and Y. C. Yortsos. Pore-network study of the characteristic periods in the drying of porous materials. *Journal of Colloid and Interface Science*, 297(2):738–748, 2006.

A. G. Yiotis, I. N. Tsimpanogiannis, and A. K. Stubos. Fractal characteristics and scaling of the drying front in porous media: A pore network study. *Drying Technology*, 28(8): 981–990, 2010.

A. G. Yiotis, D. Salin, E. S. Tajer, and Y. C. Yortsos. Drying in porous media with gravity-stabilized fronts: Experimental results. *Physical Review E*, 86:026310, 2012.

Y. C. Yortsos, B. Xu, and D. Salin. Phase diagram of fully developed drainage in porous media. *Physical Review Letters*, 79:4581–4584, 1997.

Appendix A: Simulation Parameters

Table A.1 shows the physical properties of fluids used for simulations in Chapters 3, 4 and 5.

Table A.1: Physical properties of fluids at T = 293.15 K and P = 1 atm.

Property	Value
Bulk vapor pressure, $p_{v,\infty}$ (Pa)	0.0
Equilibrium vapor pressure, p_v^* (Pa)	2339
Molar vapor mass, $\tilde{M}_v$ (kg/kmol)	18.02
Surface tension between water and air, γ (N/m)	0.07274
Universal gas constant, $\tilde{R}$ (J/kmolK)	8314.5
Air-vapor binary diffusion coefficient, D_{va} (m^2/s)	2.5685×10^{-5}

Simulation Parameters of Chapter 3

Structure and fluid parameters used for simulations in Chapter 3 are indicated in Table A.2.

Table A.2: Structure and fluid parameters for simulations in Chapter 3.

Parameter	(Fig. 3.3)	(Fig. 3.19)
Network discretization (nodes)	$25 \times 25 \times 51$	$50 \times 50 \times 51$, $25 \times 25 \times 51$
Boundary layer discretization (nodes)	$25 \times 25 \times 10$	$50 \times 50 \times 10$, $25 \times 25 \times 10$
Boundary layer thickness (mm)	10	10
Number of realizations	15	10, 15
Mean throat radius (μm)	250	250
Standard deviation of throat radius (μm)	25	25
Throat length (mm)	1	1
Viscosity ($Pa.s$)	28	28
Sample porosity	0.594	0.594
Gravity (m/s^2)	0.0	0.0

(Fig. 3.23)	(Fig. 3.25)	(Fig. 3.27)
$25 \times 25 \times 51$	$50 \times 50 \times 51$	$100 \times 100 \times 101$
$25 \times 25 \times 10$	$50 \times 50 \times 10$	$100 \times 100 \times 10$
10	10	10
15	10	1
250	250	250
25	25	25
1	1	1
0.0, 28	0.0, 28	0.0
0.594	0.594	0.594
1.3, 0	1.3, 0	1.3

Simulation Parameters of Chapter 4

Structure and fluid parameters used for simulations in Chapter 4 are indicated in Table A.3.

Table A.3: Structure and fluid parameters for simulations in Chapter 4.

Parameter	(Fig. 4.2)	(Fig. 4.10)	(Fig. 4.15)
Network discretization (nodes)	$25 \times 25 \times 51$	$25 \times 25 \times 51$	$25 \times 25 \times 51$
Boundary layer discretization (nodes)	$25 \times 25 \times 10$	$25 \times 25 \times 10$	$25 \times 25 \times 10$
Boundary layer thickness (mm)	10	10	10, 19, 59
Number of realizations	15	15	15
Mean throat radius (μm)	250	250	250
Standard deviation of throat radius (μm)	25	25	25
Throat length (mm)	1	0.4, 1, 2.5	1
Viscosity ($Pa.s$)	0.0	0.0	0.0
Sample porosity	0.594	0.594	0.594
Gravity (m/s^2)	0.0, 1.3, 13	0.0	0.0

Simulation Parameters of Chapter 5

Structure and fluid parameters used for simulations in Chapter 5 are indicated in Table A.4.

Table A.4: Structure and fluid parameters for simulations in Chapter 5.

Parameter	(Fig. 5.5)	(Fig. 5.18)
Network discretization (nodes)	$25 \times 25 \times 51$	$25 \times 25 \times 51$
Boundary layer discretization (nodes)	$25 \times 25 \times 10$	$25 \times 25 \times 10$
Boundary layer thickness (mm)	10	10
Number of realizations	15	15
Mean throat radius (μm)	250	250
Standard deviation of throat radius (μm)	25	25
Throat length (mm)	1	1
Viscosity ($Pa.s$)	0.0	0.0, 28
Sample porosity	0.594	0.594
Gravity (m/s^2)	0.0	0.0, 0.13, 1.3

Appendix B: Electronic Appendix

Codes and results of this thesis will be documented in an electronic appendix, available at the chair of Thermal Process Engineering, Otto Von Guericke University Magdeburg. In the following a list of contents of this electronic appendix is given.

MATLAB Codes and Result Files
- Pore Network Drying
    Capillary-Gravity Regime (Section 3.5.2)
    Capillary-Viscosity Regime (Section 3.4.1 and 3.5.1)
- Pore Network Drying - Surface Analysis
    Capillary-Gravity Regime (Section 4.3, 4.4 and 4.5)
- Pore Network Drying - Velocity Profile
    Capillary-Gravity Regime (Section 5.4.1, 5.5.1)
    Capillary-Viscosity Regime (Section 5.5.1)
- Capillary-Controlled Invasion Percolation (Section: 3.4.2)
- Continuum Model of Drying (Section 3.4.5)
- Extraction of Moisture Transport Coefficient
    From Pore Network Drying Simulations (3.4.4)
    From Capillary-Controlled Invasion Percolation Simulations (Section 3.4.4)
    From Inverse Method (Section 3.4.4)
- Extraction of Liquid Velocity Profiles
    From Pore Network Simulations (Section 5.4.3, 5.4.4, 5.5.2 and 5.5.3)
    From Continuum Approach (5.4.4 and 5.5.3)
- Surface Analysis (Section 4.3, 4.4 and 4.5)

Student works

The following student works were conducted within the framework of this thesis:

1. Muhammad Umer, *One-dimensional moisture transport coefficient of drying porous media obtained from inverse method.* Master thesis, Chair of Thermal Process Engineering, Otto von Guericke University Magdeburg, Magdeburg, August 2016.

2. Roozbeh Valadian, *Macroscopic parameters of drying porous media in gravity-capillary regime obtained from pore network simulations.* Master thesis, Chair of Thermal Process Engineering, Otto von Guericke University Magdeburg, Magdeburg, August 2016.

Publications and presentations

Own publications and presentations related to this thesis in national and international journals and conferences are listed the following.

Publications in national and international journals, and in conference proceedings

1. A. Attari Moghaddam, M. Prat, A. Kharaghani, and E. Tsotsas. *On the effect of stabilizing mechanisms on the liquid velocity field in a drying porous medium*, In preparation.

2. A. Attari Moghaddam, A. Kharaghani, E. Tsotsas, and M. Prat. *A pore network study of evaporation from the surface of a drying non-hygroscopic porous medium*, Submitted to AIChE Journal.

3. A. Attari Moghaddam, M. Prat, E. Tsotsas, and A. Kharaghani. *Evaporation in capillary porous media at the perfect piston-like invasion limit: Evidence of non-local equilibrium effects*, Submitted to Water Resources Research.

4. A. Attari Moghaddam, A. Kharaghani, E. Tsotsas, and M. Prat. *Insights into the velocity field in a slowly drying capillary porous medium*, 6th European Drying Conference, Liège, Belgium, 2017.

5. A. Attari Moghaddam, A. Kharaghani, E. Tsotsas, and M. Prat. *Kinematics in a slowly drying porous medium: Reconciling pore network simulations and continuum modeling*, Physics of Fluids, 29:022102, 2017.

6. A. Attari Moghaddam, A. Kharaghani, E. Tsotsas, and M. Prat. *Equivalence of the one-dimensional moisture diffusion model and the three-dimensional pore network drying model*, 20th International Drying Symposium (IDS), Gifu, Japan, 2016.

7. A. Attari Moghaddam, A. Kharaghani, E. Tsotsas, and M. Prat. *A new methodology for the extraction of moisture transport coefficient in drying porous media*, Proceeding of GRK workshop, Dec. 2015.

Oral and poster presentations in national and international conferences

1. A. Attari Moghaddam, A. Kharaghani, E. Tsotsas, and M. Prat, *Liquid velocity in drying porous media: pore network vs. continuum model*, presented (oral) in GRK workshop, 20-21 Oct. 2016, Potsdam, Germany.

2. A. Attari Moghaddam, A. Kharaghani, E. Tsotsas, and M. Prat, *Analysis of evaporative surface during drying of porous media*, presented (oral) in IVT Colloquium-OVGU, 7 Jul. 2016, Magdeburg, Germany.

3. A. Attari Moghaddam, A. Kharaghani, E. Tsotsas, and M. Prat, *Bridging the gap between discrete and continuous drying models*, presented (poster) in GRK workshop, 9-10 Jun. 2016, Erfurt, Germany.

4. A. Attari Moghaddam, A. Kharaghani, E. Tsotsas, and M. Prat, *Sensitivity of the moisture transport coefficient to the characteristics of drying porous media*, presented (oral) in Jahrestreffen der ProcessNet-Fachgruppe Trocknungstechnik, 14-15 Mar. 2016, Weimar, Germany.

5. A. Attari Moghaddam, A. Kharaghani, E. Tsotsas, and M. Prat, *A new methodology for determination of macroscopic transport parameters in drying porous media*, presented (oral) in AGU Fall Meeting, 14-18 Dec. 2015, San Francisco, USA.

6. A. Attari Moghaddam, A. Kharaghani, E. Tsotsas, and M. Prat, *Effect of network size and capillary number on macroscopic fluid transport properties of drying porous media*, presented (oral) in GRK workshop, 13-14 Nov. 2015, Brandenburg, Germany.

7. A. Attari Moghaddam, A. Kharaghani, E. Tsotsas, and M. Prat, *Determination of moisture transport coefficient from invasion percolation simulations*, presened (oral) in GRK summer school, 8-12 Jun. 2015, Berlin, Germany.

8. A. Attari Moghaddam, A. Kharaghani, E. Tsotsas, and M. Prat, *Moisture transport coefficient in drying porous media*, presented (oral) in Interpore 2015, 18-21 May 2015, Padova, Italy.

9. A. Attari Moghaddam, A. Kharaghani, E. Tsotsas, and M. Prat, *Towards estimating continuum model parameters from pore network drying simulations*, presented (oral) in Jahrestreffen der Fachgruppen Trocknungstechnik und Wärme- und Stoffübertragung, 4-6 Mar. 2015, Leipzig, Germany.

10. A. Attari Moghaddam, A. Kharaghani, E. Tsotsas, and M. Prat, *From pore network to continuous drying model*, presented (oral) in IVT Colloquium-OVGU, 9 Dec. 2014, Magdeburg, Germany.

11. A. Attari Moghaddam, A. Kharaghani, E. Tsotsas, and M. Prat, *Using PN for computation of parameters in one-equation continuum drying model*, presented (oral) in GRK workshop, 7-8 Nov. 2014, Quedlinburg, Germany.

12. A. Attari Moghaddam, A. Kharaghani, E. Tsotsas, and M. Prat, *Extraction of effective parameters from pore network simulation*, presented (oral) in GRK workshop, 23-24 May 2014, Dessau, Germany.

13. A. Attari Moghaddam, A. Kharaghani, E. Tsotsas, and M. Prat, *Estimation of effective parameters from pore network drying simulations*, presented (poster) in GRK workshop, 14-15 Jan. 2014, Magdeburg, Germany.

14. A. Attari Moghaddam, A. Kharaghani, E. Tsotsas, and M. Prat. *Estimation of effective parameters from pore network drying simulations*, presented (oral) in GRK workshop, 8-9 Nov. 2013, Wernigerode, Germany.

Curriculum Vitae

Name	**Alireza Attari Moghaddam**
Date of birth	22 September 1986
Place of birth	Tabas/Iran
E-Mail	alireza.a.moghaddam@outlook.de

Education

2013-2017	PhD in Thermal Process Engineering, Otto von Guericke University, Magdeburg, Germany
2008-2010	M.Sc. in Chemical Engineering, Amirkabir University of Technology, Tehran, Iran
2004-2008	B.Sc. in Chemical Engineering, University of Tehran, Tehran, Iran

Work experience

2013-2016	Scientific Assistant, Otto von Guericke University, Magdeburg, Germany
2008-2013	Process Engineer (part-time), Research Institute of Petroleum Industry, Tehran, Iran